SEARCH FOR HIGH ENERGY GRB NEUTRINOS IN ICECUBE

A Thesis
Presented to
The Academic Faculty

by

James Casey

In Partial Fulfillment
of the Requirements for the Degree
Doctor of Philosophy in the
School of Physics

Georgia Institute of Technology
August 2015

SEARCH FOR HIGH ENERGY GRB NEUTRINOS IN ICECUBE

Approved by:

Dr. Ignacio Taboada, Advisor
School of Physics
Georgia Institute of Technology

Dr. A. Nepomuk Otte
School of Physics
Georgia Institute of Technology

Dr. Laura Cadonati
School of Physics
Georgia Institute of Technology

Dr. Deirdre Shoemaker
School of Physics
Georgia Institute of Technology

Dr. Paul Steffes
School of Electrical and Computer Engineering
Georgia Institute of Technology

Date Approved: May 5, 2015

This is dedicated to my family and especially my Mom who have all been very supportive.

PREFACE

In recent years, astronomers and astrophysicist have begun to search for new ways to explore the Universe. Multi-messenger astronomy has changed the way we study the Universe by expanding our searches to include the observation of particles and gravitational waves. The IceCube Neutrino Observatory is a neutrino detector designed to explore the Universe through the observation of particles called neutrinos. Neutrinos are notoriously difficult to detect, but this very attribute also makes them of great interest to scientists. Their limited interactions make less likely to be disturbed by other interactions. They can provide insight deep into astrophysical processes that would otherwise be obscured by gas and dust.

The IceCube collaboration has detected for the first time very-high-energy astrophysical neutrinos. These are the first neutrinos ever detected at such high energies. The energy distribution of these events along with the method in which they were detected provides strong support that these events originate in distant astrophysical processes. The next step is to determine what these processes are. Time dependent point source searches and time clustering searches have not been able to identify source candidates, leaving the question open.

The origin of ultra-high-energy cosmic rays is a mystery that one day may be solved through the observation of neutrinos. GRBs have been proposed as one possible source class of these cosmic rays. The analysis presented here is a search for correlation between 35 very-high-energy neutrino events showing astrophysical origin and a stacked list of 856 gamma-ray bursts (GRBs) from data collected between May 2010 and May 2013. This analysis not only searches for the expected neutrino signature of this cosmic-ray production from GRBs, it also explores new regimes by expanding the search to time scales extending up to 15 days before and after the bursts. This is the first time such an extended time search has been performed looking for correlations between GRBs and neutrinos.

ACKNOWLEDGEMENTS

First and foremost, I would like to thank Ignacio. I definitely would not have made it through to the end without your help, guidance, and patience. I would also like to thank Dirk for all the helpful discussions as I worked through the analysis. I want to thank my office mates, Jacob and Greg, without whose ridiculous conversations, I would have been so... productive. Finally, I would like to thank everyone in the IceCube collaboration. There are far too many to list by name, but so many of you have helped guide me in this work and provided support, especially at our various collaboration meetings and conferences. These meetings were some of the best times I have had in graduate school. And for the record... Yes, Greg, I am serious.

TABLE OF CONTENTS

LIST OF TABLES

LIST OF FIGURES

SUMMARY

IceCube has reported the observation of 35 neutrino events above 30 TeV with evidence for an astrophysical neutrino flux using data collected from May 2010 to May 2013. These events provide the first high energy astrophysical neutrino flux ever observed. The sources of these events are currently unknown. IceCube has looked for correlations between these events and a list of TeV photon sources including a catalog of 36 galactic sources and 42 extragalactic sources, correlations with the galactic plane and center, and spatial and temporal clustering. These searches have shown no significant correlations. The isotropic distribution of the event directions gives indications that the events could be extragalactic in nature and therefore may originate in the same processes that generate ultra-high-energy cosmic rays (UHECRs). The sources of these UHECRs are still unknown; however, gamma-ray bursts (GRBs) have been proposed as one possible source class. By determining the source of these high energy neutrinos, it may be possible to determine the sources of UHECRs as well.

This study is a search for directional and temporal correlation between 856 GRBs and the astrophysical neutrino flux observed by IceCube. Nearly 10,000 expanding time windows centered on the earliest reported time of the burst were examined. The time windows start at ± 10 s and extend to ± 15 days. We find no evidence of correlations for these time windows and set an upper limit on the fraction of the astrophysical flux that can be attributed to the observed GRBs as a function of the time window. GRBs can contribute at most 12% of the astrophysical neutrino flux if the neutrino-GRB correlation time is less than $\approx$20 hours, and no more than 38% of the astrophysical neutrino flux can be attributed to the known GRBs at time scales up to 15 days. We conclude that GRBs observable by satellites are not solely responsible for IceCubes astrophysical neutrino flux, even if very long correlation time scales are assumed.

CHAPTER I

NEUTRINOS

Neutrinos are subatomic particles first proposed by Wolfgang Pauli [1] in 1930 as a means to explain how beta decays could conserve energy, momentum, and spin. He postulated that there was a nearly undetectable particle that was carrying off the missing quantities from the interactions. The first direct detection came in 1956 [2] by observing the gamma rays from electrons annihilating with positrons generated through neutrino-proton interactions in inverse beta decay (eq. 1.1). The neutrinos were generated in the nuclear reactor located at the Savannah River Sight and captured in two tanks of water surrounded by scintillating material that was used to observe the generated gamma rays.

$$\begin{aligned} \bar{\nu}_e + p &\longrightarrow n + e^+ \\ e^+ + e^- &\longrightarrow \gamma + \gamma \end{aligned} \tag{1.1}$$

Neutrinos are difficult to detect because they very rarely interact with matter, but this very attribute makes them of great interested to many physicists, in particular astrophysicists. By studying neutrinos, scientists are able to learn more about the fundamental laws governing particles and their interactions. They can also give a glimpse into interactions deep inside stars where they pass through layers of gas and dusts that trap light obscure internal physical processes. The study of neutrinos may one day give insights into dark matter, the baryon asymmetry, and the sources of the highest energy cosmic rays.

1.1 Neutrino Detection

Neutrinos are neutral leptons and do not interact through the electromagnetic force. They only interact through the weak and gravitational forces. This property makes them difficult to detect as the weak force has a small interaction cross section. The neutrino cross section as a function of energy is given in figure 1.1. There are three types or flavors of neutrinos. Each corresponds to one of the three charged leptons types: electron e, muon μ, and tau τ.

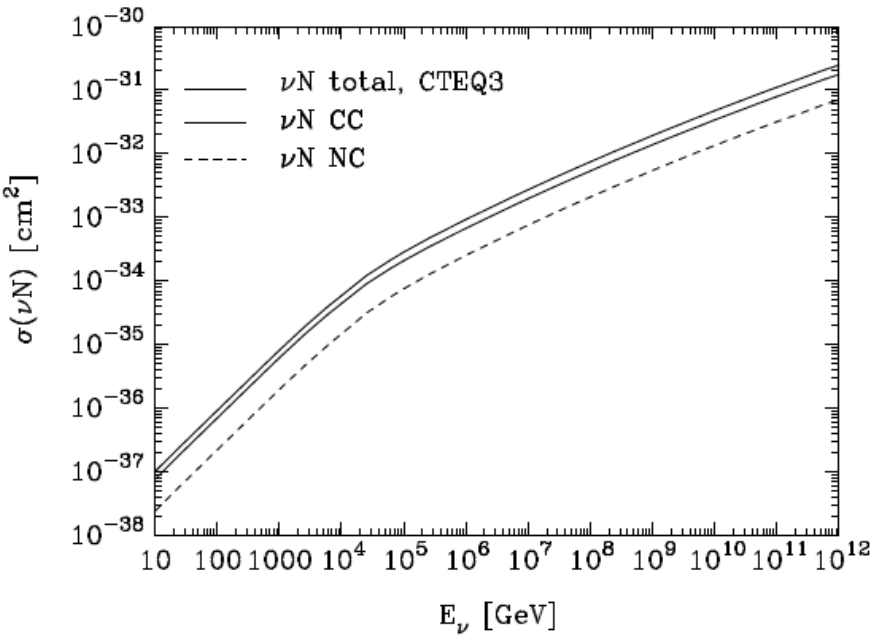

Figure 1.1: The cross section for neutrino-nucleon interactions is given as a function of energy. The cross section increases with energy causing the Earth to become opaque at the highest neutrino energies. Figure from [3].

Neutrinos rarely interact with matter as they pass through. The low interaction rate can be mitigated by large fluxes of neutrinos. For example, there are approximately 7×10^{10} s^{-1} cm^{-2} solar neutrinos passing through the Earth. The cross section, however, increases with energy. While low energy neutrinos will pass through the Earth with almost no interactions, the Earth becomes opaque to the higher energy neutrinos. This begins to have an affect at the energies that IceCube is most sensitive. At near PeV energies, the Earth becomes opaque to neutrinos [4], which can have an impact on many neutrino searches in IceCube. Figure 1.2 shows the flux of neutrinos after passing through the Earth at various energies.

Neutrinos interact weakly through charged current and neutral current interactions. Figure 1.3a shows the primitive vertex for neutral current neutrino interactions where l can be any lepton type including neutrinos. In neutral current interactions neutrinos interact with other particles, in particular atomic nuclei, through the exchange of a Z boson to pass energy on to the particle. Figure 1.3b shows the primitive vertex for charged current neutrino interactions where l can be any neutrino flavor. Neutrinos generate charged leptons

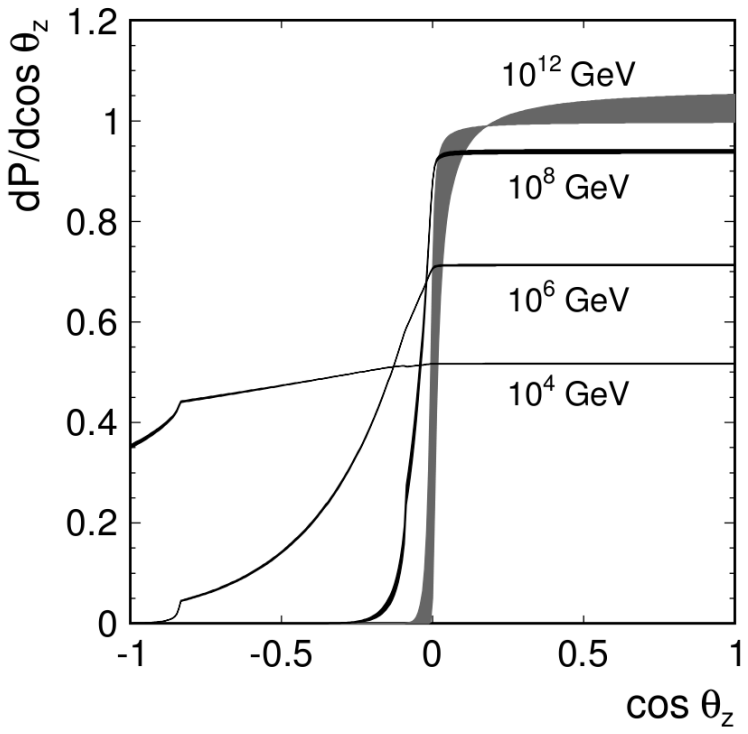

Figure 1.2: Neutrino distribution due to earth absorption as a function of the cosine of the zenith angle where $\theta_z = 0$ is directly above the detector. Various energies are depicted. As the energy increases, the earth becomes opaque to neutrinos as indicated by the drop of neutrinos for $\cos\theta_z < 0$. Figure from [4].

through charged current interactions where there is an exchange of a W^+ or W^- boson.

These vertices govern the interactions of neutrinos. Neutrinos can scatter off of nuclei in deep inelastic scattering to create new leptons and/or transfer energy to the nuclei, which then in turn generate hadronic showers of particles as the nucleon breaks apart from the massive amounts of energy imparted. Hadronic showers are showers of hadrons such as protons, neutrons, and pions created as particles move through a medium and may be generated in both charged and neutral current interactions. The Feyman diagram for a hadronic shower from a charged current interaction is given in figure 1.4.

Equation 1.2a gives the interaction of a neutrino and nucleon in a neutral current interaction, and equation 1.2b gives the interaction of a neutrino and nucleon in a charged current interaction. The observation of the particles generated in these interactions is used to detect neutrinos. Specifically for this analysis, the energy of the particles generated in these interactions is so great that the charged particles created in the interactions will create

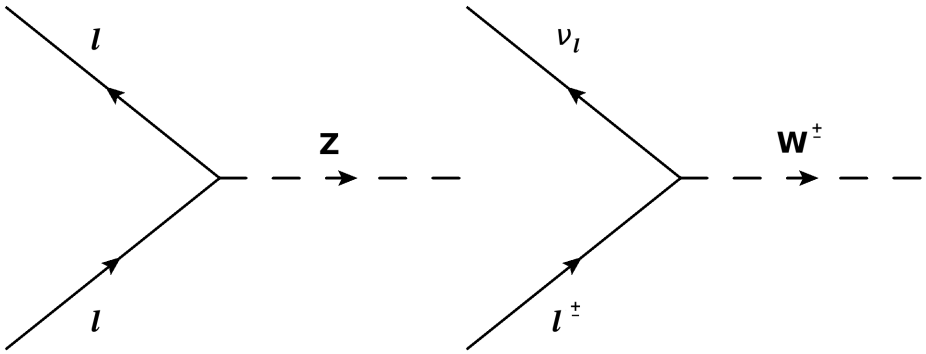

(a) Neutral Current Interaction (b) Charged Current Interaction

Figure 1.3: Feynman diagrams for the weak force interaction primitives involving neutrino interactions. The figure on the left is the neutral current interaction. The l can be any lepton, including any flavor of neutrino. The figure on the right is the charged current interaction where l is any of the charged leptons and the ν_l is its corresponding neutrino counter part.

flashes of light called Cherenkov radiation as they move through the clear ice located at the South Pole.

$$\begin{aligned} p(n) + \nu_l &\longrightarrow p(n) + \nu_l \\ p(n) + \bar{\nu}_l &\longrightarrow p(n) + \bar{\nu}_l \end{aligned} \tag{1.2a}$$

$$\begin{aligned} n + \nu_l &\longrightarrow p + l^- \\ p + \bar{\nu}_l &\longrightarrow n + l^+ \end{aligned} \tag{1.2b}$$

These interactions lead to the creation of new particles, which deposit energy in different ways. The two primary topologies created by neutrino interactions in the IceCube Neutrino Observatory (see chapter 3) are tracks created by muons in charged current interactions and cascades generated by almost all other interactions. A track is so named because it deposits light in the over a long distances. Tracks at the energies relevant to this search are on the order of 10 km [6] and will radiate energy away through ionization, bremsstrahlung, pair production, and photo-nuclear interactions. The energy loss of tracks can be approximated by

$$-\frac{dE}{dx} = a + bE. \tag{1.3}$$

The value of a is due to ionization and can be found using the Bethe-Bloch formula [7], and the value of b is related to all the other forms of energy loss. Approximate values

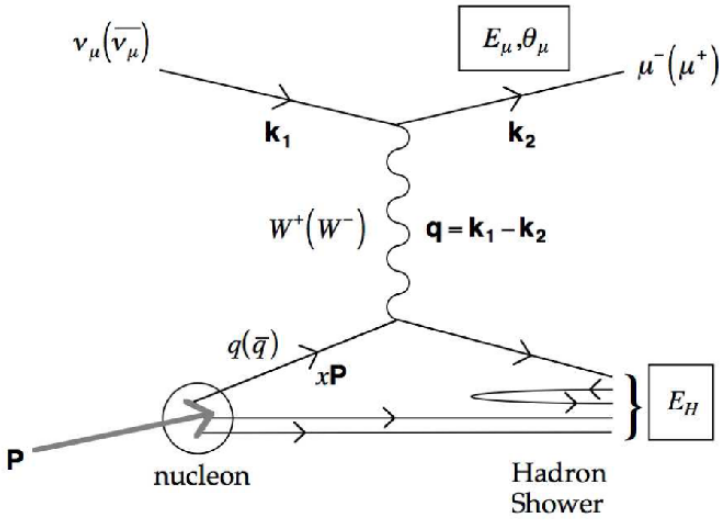

Figure 1.4: Feyman Diagram for a Neutrino-Nucleon Interaction. A muon neutrino scatters off of a nucleon creating muon and a hadronic shower [5].

determined by simulation for a and b in ice for the energy range of 20 to 10^{11} GeV are $a = 0.246$ GeV m^{-1} and $b = 4.31 \times 10^{-3}$ m^{-1} [8].

Cascades are primarily generated from hadronic showers or relativistic electrons and tau particles. Electrons lose energy in a similar fashion to muons but over much shorter distances since they have much less mass. The energy loss due to bremsstrahlung dominates at energies above 79 MeV in water. This energy loss is given by

$$-\frac{dE}{dx} = \frac{E}{L_0} \tag{1.4}$$

where L_0 is the radiation length. In ice $L_0 \approx 40$ cm [9]. The photons lost in this process will then pair produce to generate electrons and positrons which will generate more photons and so on to create a shower as seen in figure 1.5. The total length of the shower is given by

$$L = L_0 \frac{\log(E_0/E_c)}{\log(2)} \tag{1.5}$$

where E_0 is the initial energy of the particle and E_c is the critical energy. The critical energy is were the energy loss from bremsstrahlung is equivalent to the energy loss due to ionization. Using the above equations, the length of a typical shower for a 100 TeV electron is determined to be ≈8 m. Figure 1.6 shows the number of photons deposited by

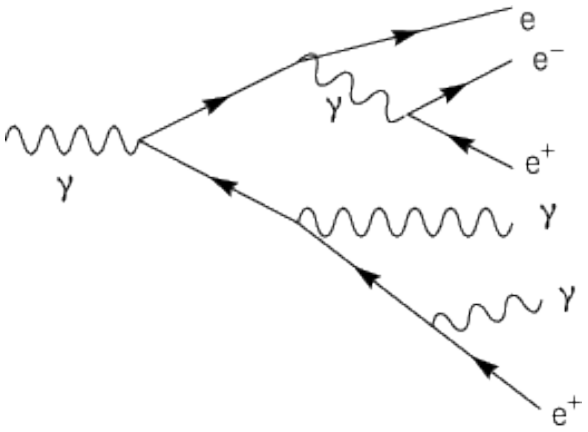

Figure 1.5: An electromagnetic shower. An electron will generate a pair of photons through bremsstrahlung which then can pair-produces an electron and positron that will each generate more photons to create an electromagnetic shower. Figure from [10]

an electromagnetic cascade for various energies from simulation.

The mechanism for energy loss in hadronic cascades is more complicated due to the production of neutrons in the hadronic shower. Pion production during the shower will dissipate some of the energy through electromagnetic showers as $\pi^0 \rightarrow \gamma\gamma$. The length of the cascade will also be somewhat longer due to the longer interaction length for hadronic interactions in ice (0.91 m [9,11]). The average total light yield [11] for a hadronic cascade relative to a purely electromagnetic cascade can be parameterized by

$$F = F_{EM} + (1 - F_{EM}) f_0 \tag{1.6}$$

where f_0 is the relative Cherenkov light produced from the hadronic component of the cascade and F_{EM} is the fraction of the light yield from the purely electromagnetic component. Using equation 1.6 and

$$F_{EM} = 1 - \left(\frac{E}{E_0}\right)^{-m} \tag{1.7}$$

where E is the total energy of the system and E_0 and m are phenomenological values determined by simulation, the distribution of F can be determined to be a Gaussian with mean F and

$$\sigma = F\sigma_0 \log(E)^{-\gamma} \tag{1.8}$$

where σ_0 and γ are model parameters. The values for the parameters above are given in table 1.1.

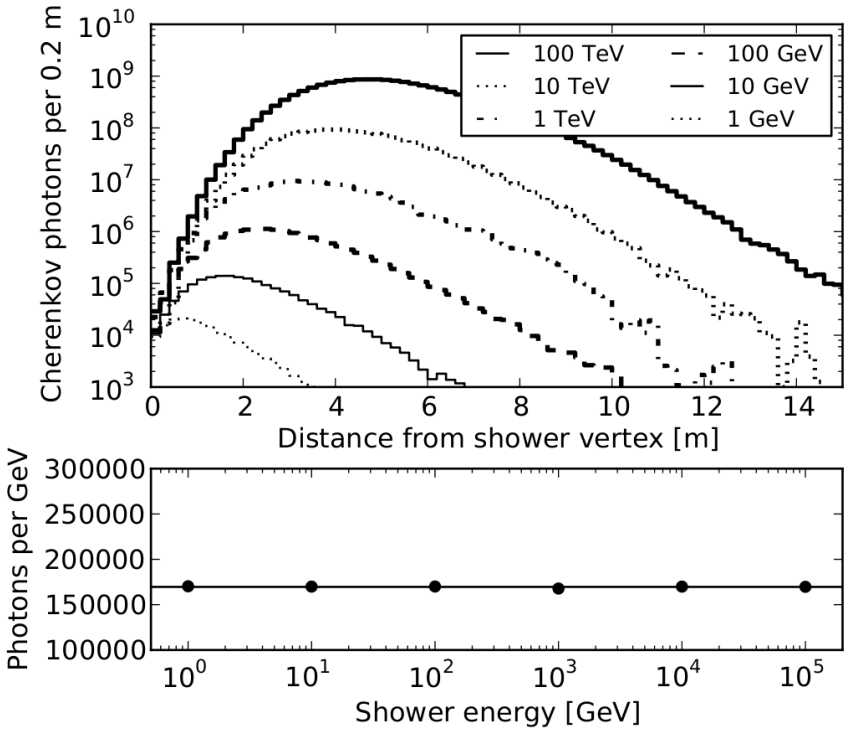

Figure 1.6: The figure shows the number of photons generated by cascades as derived from simulation. The upper plot gives the photon generation as a function of the distance and the lower panel shows the number of photons generated as a function of energy. Figure from [11].

Tau particles generated from charge current interactions will generate two cascades in the detector. The first is from the initial interaction as the neutrino scatters off of a nucleon. The second will be as a result of the decay of the tau to lighter particles. Taus with sub-PeV energies will travel short distances such that the cascades may be indistinguishable from one another, giving a general cascade signature. At energies $\gtrsim$1 PeV, unique topologies may be visible such as the double bang which looks like a pair of near simultaneous cascades in a very short area. These higher energy tau topologies have not yet been observed.

1.1.1 Cherenkov Radiation

Cherenkov radiation is light created from charged particles moving through a medium at a velocity greater than the phase velocity of light in that medium. The phase velocity of light is given by $v_p = c/n$ where n where n is the refractive index of the medium. For the IceCube detector, the medium is ice. Charged particles move through the ice with relativistic speed

Table 1.1: Hadronic Shower Energy Distribution Parameters. Table from [11]

Parameter	Value
E_0	0.399
m	0.130
f_0	0.467
σ_0	0.379
γ	1.60

given by $v/c = \beta \approx 1$ creating polarization in the ice. The velocity of the charged particle is such that the medium does not have time enough to relax as the particle passes, but instead creates a trail of radiation that forms a coherent front in the form of a shockwave as seen in figure 1.7. The shockwave moves at an angle θ relative to the motion of the particle which is related to the velocity of the particle by

$$\theta = \cos^{-1}\left(\frac{1}{n\beta}\right). \tag{1.9}$$

For ice, $n \approx 1.31$ giving $\theta \approx 40°$.

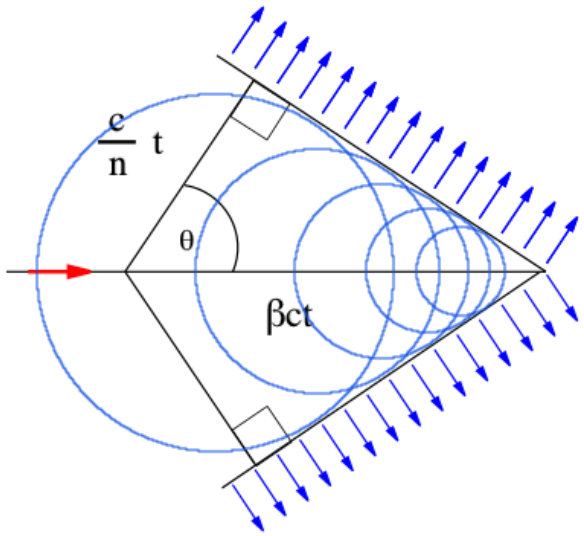

Figure 1.7: Cherenkov radiation is generated as a particle moves faster than the speed of light in a given medium. Radiation is generated as the polarized medium relaxes forming a coherent front. Image from [12].

The intensity of the photons generated in Cherenkov radiation increases with frequency where it peaks in the UV range as the propagation media typically become opaque at UV frequencies. This gives the light in a bluish tint in the visible spectrum. The spectrum of

Cherenkov radiation is given by

$$\frac{dN}{dxd\lambda} = \frac{2\pi\alpha}{\lambda^2}\left(1 - \frac{1}{\beta^2 n^2(\lambda)}\right) \tag{1.10}$$

where α is the fine structure constant and given by$\alpha \approx 1/137$, and $n(\lambda)$ is the wavelength dependent index of refraction. The detection of Cherenkov radiation is done IceCube through a large number of photon sensors called PMTs frozen into the ice at the South Pole (see section 3.4). Neutrinos interact with the nucleons in the ice to generate muons and hadronic showers that in turn generate Cherenkov radiation that is detected by the PMTs. A muon moving through the detector produces ≈250 photons per cm [13] in the wavelength range of 300 nm to 500 nm.

1.2 Neutrino Oscillations

Neutrinos have very low masses compared to all other known massive particles and for a time they were believed to be massless particles in the standard model [14]. All attempted measurements of the mass has only resulted in upper limits [15]. The current limits on the neutrino masses are given in table 1.2.

Table 1.2: Neutrino Mass Upper Limits [15]

Flavor	Symbol	Mass
Electron Neutrino	ν_e	< 2 eV
Muon Neutrino	ν_μ	< 190 keV
Tau Neutrino	ν_τ	< 18.2 MeV

Through neutrino oscillations, it was discovered that neutrinos were not massless but instead had a low mass that was difficult to measure. Neutrino oscillation refers to the changing of flavor of a neutrino as it propagates through space. A neutrino starting out as an electron neutrino ν_e may oscillate from one flavor to another and be observed at some later time as a muon or tau neutrino, ν_μ or ν_τ respectively. As shown below, this oscillation between neutrino flavors requires the neutrinos to have a non-zero mass.

In 1968, neutrino oscillations were observed by a deficit of solar neutrinos [16, 17]. Ray Davis was attempting to detect the neutrinos generated inside the Sun. These neutrinos were expected to pass through the outer layers of the Sun giving unique view into the solar

interior. In order to observe these neutrinos, the Homestake experiment was constructed in the Homestake mine in Lead, South Dakota, 1,478 meters underground. A tank with a volume of 380 m^3 was filled with perchloroethylene (C_2Cl_4) to act as a target for the solar neutrinos. Neutrinos would interact with the chlorine-37 to create argon-37 (equation 1.11) which was then extracted and counted to give the number of neutrino interactions.

$$\nu_e + {}^{37}\mathrm{Cl} \longrightarrow {}^{37}\mathrm{Ar} + \mathrm{e}^- \tag{1.11}$$

Only 1/3 of the expected number of neutrinos were observed. This raised questions as to whether the neutrinos were not understood or the Standard Solar Model was wrong. It was proposed that the neutrinos could actually be changing flavors from electron neutrinos to muon and tau neutrinos, as the Homestake experiment was only sensitive to electron neutrinos; any other neutrinos would pass through without interacting. Later several other experiments were able to confirm the deficit of solar neutrinos. Finally in 2001, the Sudbury Neutrino Observatory (SNO) was able to show that solar neutrinos were in fact oscillating between flavors [18].

The SNO detector consisted of a 1,000 metric tons of heavy water in an acrylic vessel with a 6 m radius. The vessel contained 9,600 photomultiplier tubes (PMTs). SNO was sensitive to all three flavors of neutrinos through neutral current interactions. In these interactions, a neutrino would dissociate a deuteron and break it into a proton and neutron. The resulting neutron would be captured very quickly by a nucleus releasing a gamma ray with ≈6 MeV of energy. This gamma ray is then detected by the PMTs. Because it was sensitive to all three flavors it was able to detect the previously unobserved neutrino flavors confirming neutrino oscillations. Observation of neutrino oscillation led to the determination that neutrinos are in fact not massless as the oscillations would be a function of the mass eigenstate energies.

Just as neutrinos have three flavor eigenstates where each of the flavors corresponds to another lepton partner: e, μ, and τ, there are also three mass eigenstates: 1,2, and 3. Each of the flavor states is a mix of the mass states. Generally, the observed neutrino flavor state ν_α (α = e, μ, or τ) is a mix of the mass eigenstate ν_i (i = 1, 2, or 3) where the mixing is

given by equation 1.12 and the flavor state is given by equation 1.13 (see [19]).

$$\nu_\alpha = \sum_{i=1}^{3} \mathrm{U}_{\alpha,i}\nu_i \tag{1.12}$$

$$|\nu_\alpha\rangle = \sum_{i=1}^{3} U^*_{\alpha,i}\,|\nu_i\rangle \tag{1.13}$$

In the equations above, $\mathrm{U}_{\alpha,i}$ is from the mixing matrix U. This matrix describes the relationship of the mixing between the states. The mixing matrix U is outlined in equation 1.14. In the equations below, $\mathrm{c}_{i,j}$ represents $\cos\theta_{i,j}$ where $\theta_{i,j}$ is the mixing angle between mass states i and j. Likewise, $\mathrm{s}_{i,j}$ is $\sin\theta_{i,j}$. The $\exp(i\delta)$ is a phase related to CP violation (see ref. [19]).

$$U = \begin{pmatrix} 1 & 0 & 0 \\ 0 & \mathrm{c}_{23} & \mathrm{s}_{23} \\ 0 & -\mathrm{s}_{23} & \mathrm{c}_{23} \end{pmatrix} \begin{pmatrix} \mathrm{c}_{13} & 0 & \mathrm{s}_{13}e^{i\delta} \\ 0 & 1 & 0 \\ -\mathrm{s}_{13}e^{i\delta} & 0 & \mathrm{c}_{13} \end{pmatrix} \begin{pmatrix} \mathrm{c}_{12} & \mathrm{s}_{12} & 0 \\ -\mathrm{s}_{12} & \mathrm{c}_{12} & 0 \\ 0 & 0 & 1 \end{pmatrix} \tag{1.14}$$

$$= \begin{pmatrix} \mathrm{c}_{12}\mathrm{c}_{13} & \mathrm{s}_{12}\mathrm{c}_{13} & \mathrm{s}_{13}e^{i\delta} \\ -\mathrm{s}_{12}\mathrm{c}_{23} - \mathrm{c}_{12}\mathrm{s}_{23}\mathrm{s}_{13}e^{i\delta} & \mathrm{c}_{12}\mathrm{c}_{23} - \mathrm{s}_{12}\mathrm{s}_{23}\mathrm{s}_{13}e^{i\delta} & \mathrm{s}_{23}\mathrm{c}_{13} \\ \mathrm{s}_{12}\mathrm{s}_{23} - \mathrm{c}_{12}\mathrm{c}_{23}\mathrm{s}_{13}e^{i\delta} & -\mathrm{c}_{12}\mathrm{s}_{23} - \mathrm{s}_{12}\mathrm{c}_{23}\mathrm{s}_{13}e^{i\delta} & \mathrm{c}_{23}\mathrm{c}_{13} \end{pmatrix} \tag{1.15}$$

The probability of observing flavor state ν_α after oscillations in free space is given by

$$P(\nu_\alpha \to \nu_\beta) = |\,\langle\nu_\beta|\mathcal{U}(t)|\nu_\alpha\rangle|^2\,, \tag{1.16}$$

where $\mathcal{U}(t)$ is the time evolution operator of a free particle (not to be confused with the mixing matrix U) given by

$$\mathcal{U}(t) = \exp\Big(-i\hat{H}t\Big). \tag{1.17}$$

Using the equations 1.13 and 1.16, it can be shown that the probability of a relativistic neutrino in flavor state α oscillating to state β is given by 1.18.

$$P(\nu_\alpha \to \nu_\beta) = \left|\sum_i U^*_{\alpha i}U_{\beta i}e^{-i\frac{m_i^2}{2E}L}\right|^2 \tag{1.18}$$

For simplification, the probability for transition in a two state system is given in equation 1.19. In this simplification, the Δm^2 term is the differences in the squared mass states or $m_2^2 - m_1^2$.

$$P(\nu_\alpha \to \nu_\beta) = sin^2 2\theta sin^2\left(\frac{1.27\Delta m^2(eV^2)L(km)}{E_\nu(GeV)}\right) \tag{1.19}$$

Using this simplification makes it easier to see the how the probability varies with its parameters. The value of the mixing angle θ in the first sine function is a constant that currently must be determined through experiment. In the three state system, there are three separate mixing angles that must be measured (though it is really the sine function that is measured). Notice the probability of oscillation is dependent on the difference of the squared masses in the second sine function. It is easy to see here the mass dependence of the oscillations. For zero values of the mass difference, there would be no oscillations. It is also import to notice that the oscillation is a function of L/E where E is the energy of the particle and L is the length the neutrino travels.

For long distances, the distance dependent terms can be averaged out to give estimates on the observed neutrino ratios in the three state system. Many GRB neutrino models predict flavor ratios of Φ_{ν_e}:Φ_{ν_μ}:$\Phi_{\nu_\tau} = 1 : 2 : 0$ at the source (see section 2.3). Examining the ratio of neutrinos for long baselines with this starting ratio gives an observed flavor ratio of Φ_{ν_e}:Φ_{ν_μ}:$\Phi_{\nu_\tau} = 1 : 1 : 1$ at Earth. Another common astrophysical source flavor ratio is Φ_{ν_e}:Φ_{ν_μ}:$\Phi_{\nu_\tau} = 0 : 1 : 0$, which may happen if there is muon cooling in the GRB. The observed flavor ratio at Earth would then be Φ_{ν_e}:Φ_{ν_μ}:$\Phi_{\nu_\tau} = 1 : 2 : 2$. By comparing the neutrino flavor ratio observed at Earth to known models, it is possible to gain more insight into the details of physics of the sources.

There are still some questions in the observed neutrino oscillations. One major question is the sign of the $\Delta m^2_{i,j}$ terms. This presents itself in the form of the neutrino hierarchy problem. The current values for the observed oscillation parameters are given in table 1.3.

Table 1.3: Neutrino Mass Mixing Parameters [14]

Parameter	**Value**
$\sin^2 2\theta_{12}$	0.846 ± 0.021
$\sin^2 2\theta_{23}$	$0.97^{+0.03}_{-0.06}$
$\sin^2 2\theta_{13}$	0.093 ± 0.008
δ/π	1.39
Δm^2_{12}	$7.53 \pm 0.18 \times 10^{-5}$ eV^2
Δm^2_{32} (assuming normal mass hierarchy)	$2.44 \pm 0.06 \times 10^{-3}$ eV^2
Δm^2_{32} (assuming inverted mass hierarchy)	$2.52 \pm 0.07 \times 10^{-3}$ eV^2
Δm^2_{13}	$\approx \Delta m^2_{32}$

Just as the flavor states are mixes of the mass states, the mass states can also be thought of as mixes of the flavor states. The mass eigenstates cannot be observed directly, but are determined from interactions through the flavor states. As shown above, neutrino oscillations are dependent on the differences of the squares of the masses. While it has been possible to measure the value of the differences, there is still some uncertainty about the sign of the differences. The relationship between m_1^2 and m_2^2 has been determined but the sign relationship of m_3^2 to m_1^2 and m_2^2 is still unknown. This manifests itself through the possibility of two possible hierarchies. The two possible hierarchies, normal and inverted, are shown in figure 1.8.

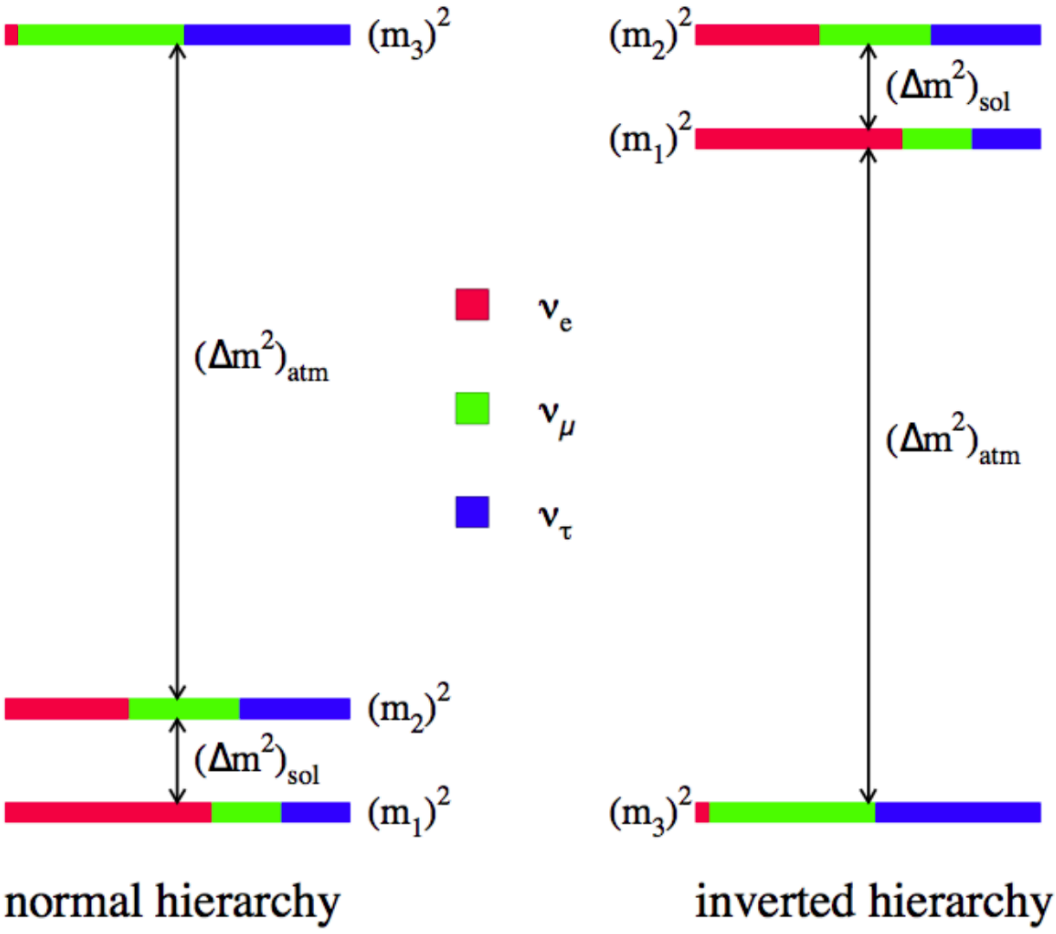

Figure 1.8: The two possible neutrino mass hierarchies. There is some ambiguity in the relationship between the m_3^2 and the m_1^2 and m_2^2 differences. This is a question IceCube hopes to be answer in the near future. Figure from [20].

The IceCube Neutrino Observatory is one of many experiments hoping to resolve the question of the neutrino mass hierarchy. For a more detailed discussion of the mass hierarchy problem see [20].

1.3 Neutrino Astronomy

Neutrino astronomy is a relatively new branch of astrophysics. Neutrinos are interesting to astronomers as they have unique properties that allow them to provide insight into astrophysical processes. Unlike photons, neutrinos are not obscured by interstellar or intergalactic gas and dust. Neutrinos are also able to pass through the outer layers of stars to reveal the internal structure and activity of the stars in which they are generated. Because neutrinos are neutral particles they are also unaffected by magnetic fields that deflect charged particles such as cosmic rays. In fact, neutrinos have been proposed as a means to detect the sources of the highest energy cosmic rays, as the same processes that accelerate the cosmic rays, should also be strong sources for neutrinos.

So far, only two non-terrestrial neutrino sources have been identified. The brightest astrophysical neutrino source detected is the sun. Several experiments have been able to detect neutrinos generated in solar processes. The second source was Supernova 1987A. Three different detectors observed a total of 24 neutrinos generated in the supernova [21–25]. The IceCube Neutrino Observatory has since detected 37 astrophysical-neutrino candidates [26, 27]; however, the sources of these neutrinos is still unknown (see chapter 4).

1.3.1 Cosmic Rays

One branch of neutrino astronomy that is of particular interest is the search for the origins of cosmic rays. Cosmic rays are charged particles generated in astrophysical processes that are constantly bombarding the atmosphere of the Earth. They are mostly composed of protons but can include heavier nuclei up through iron. As these energetic particles interact with the atmosphere they create showers of particles and photons that can be detected at the Earth's surface. Neutrinos may be able to give insight into processes that accelerate these particles. For example, the observation or even non-observation of neutrinos from expected cosmic ray sources can set limits on hadronic acceleration from these sources. The flavor

ratio of observed neutrinos (see section 1.2) can give insight into the processes accelerating the cosmic rays as well.

Cosmic rays were first discovered in 1912 by Victor Hess [28] while trying to determine the origin of ionization on the surface of the Earth. In an attempt to determine the source of the ionization, he carried ionization detectors in a hot-air balloon to an altitude of 5,300 m. He found that the ionization increased with altitude rather than decreasing suggesting that the Earth was not the source of the ionization, but rather the source was from interactions in the atmosphere from above.

Determining the origin of cosmic rays can be challenging. Since cosmic rays are charged particles, they are deflected in magnetic fields that exist inside and outside the galaxy. This deflection obscures the origin direction of all but the highest energy cosmic rays. It is possible to look for electromagnetic signatures for cosmic ray production, but there is some difficulty in identifying these sources. Light produced in these interactions can be blocked by gas and dust between the sources and the Earth. There is also some ambiguity in the source photon spectra. Photons generated from leptonic sources (e.g. accelerated electrons) may not be distinguishable from hadronic sources (i.e. accelerated nuclei that form cosmic rays). This uncertainty with the respect to the photon generation makes it difficult to confirm a photonic sources as a simultaneous sources of cosmic rays.

In particular, the sources of ultra high energy cosmic rays (UHECRs) are of interest due to the high energies that have been observed from these cosmic rays. UHECRs have such high energies, they require a very energetic source to accelerate the particles involved. Sources that accelerate atomic nuclei to such energies will invariably generate neutrinos in the process. Since, neutrinos are neutral particles, they are not deflected in magnetic fields. Unlike cosmic rays, they point back to their sources. By observing neutrinos along with electromagnetic observations such as gamma rays, IceCube may be able to resolve the question of the source of UHECRs.

The cosmic ray energy spectrum has been measured by several experiments. As can be see in figure 1.9, the spectrum generally follows a broken power law. There are two breaks in the spectrum which are believed to be an indication of the source mechanisms at those

energies. The first break occurs around a few PeV or at what is called the *knee*. Below the knee the cosmic ray spectrum follows a power law with

$$\frac{dN}{dE} \propto E^{-2.7}. \tag{1.20}$$

Sources in this energy range are mostly believed to be in the local galaxy. At energies above the knee, it is believed that there may be a transition from galactic to extra-galactic. At these energies, particles will begin to exceed the confinement radius of the magnetic fields in the galaxy. It has also been suggested that this may be the upper end of the energy range obtainable from galactic sources. Energies above the knee follow a softer spectrum:

$$\frac{dN}{dE} \propto E^{-3.0} \tag{1.21}$$

The second break comes at around a few EeV at the *ankle* where the spectrum hardens again to

$$\frac{dN}{dE} \propto E^{-2.6}. \tag{1.22}$$

Cosmic rays generated above the ankle are called Ultra High Energy Cosmic Rays or UHECRs. At these energies the sources are believed to be external to the galaxy and generated in very energetic events such as GRBs and active galactic nuclei.

One of the primary challenges for determining the source of cosmic rays is finding sources that are energetic enough to accelerate particles to the observed energies. Cosmic rays are generally believed to be accelerated through a process called Fermi acceleration. In first order Fermi acceleration, particles are reflected back and forth across the interface of two magnetic fields. As the particles move back and forth across the boundary, the particle energy increases. In order for Fermi acceleration to take place, charged particles must be confined to the region of acceleration through magnetic fields. Figure 1.10 shows the magnetic field requirements as a function of the size of the acceleration region for protons at 10^{20} eV and 10^{21} eV and iron at 10^{20} eV. It also shows various source objects and characteristic size and magnetic field strength for those objects. By examining the relationship between the source size and the characteristic magnetic fields, it is possible to rule out source mechanisms for cosmic rays at given energies.

Note that GRBs show the required magnetic field for confinement to accelerate UHECRs to the observed energies. The same processes that accelerate atomic nuclei to these energies are also expected to be generating neutrinos. This makes GRBs of great interest in the search for the yet unknown sources of UHECRs

1.3.2 Cosmic Rays as Background Neutrino Astronomy

One large problem in detecting neutrinos is separating background events from astrophysical events. As much as we hope to learn from studying cosmic rays, they make neutrino detection more difficult. As cosmic rays interact in the atmosphere, they generate showers of particles (figure 1.11) that can mimic neutrinos in many detectors. Specifically, cosmic rays generate atmospheric muons and neutrinos that interact in the IceCube detector to mimic astrophysical neutrinos. IceCube has a background rate of ≈3 kHz mainly due to muons created in cosmic-ray air showers above the detector.

$$\pi^{\pm} \longrightarrow \mu^{\pm} + \nu_{\mu} \tag{1.23}$$

Other particles such as electrons and hadrons and some muons created in these interactions are unable to penetrate the atmosphere combined with the 1.5km of ice above the detector and do not contribute significantly to the background.

The IceCube collaboration has developed many innovative ways to mitigate the background contribution from cosmic ray air showers. Many analyses include a directional veto in their event selection and only use upward going events from the northern hemisphere to filter out this muon background. Muons are unable to penetrate through large amounts of the Earth, so any events arriving from underneath the detector are most likely neutrinos.

The contribution due to atmospheric neutrinos generated in the cosmic ray air showers, however, is prevalent across the entire sky. Atmospheric neutrinos are more difficult to distinguish from astrophysical neutrinos. IceCube uses timing information combined with location clustering and event energies to help determine the origin of these events. For searches that focus on transient events such as GRBs, the timing and location of the GRBs combined with a list of candidate neutrino events provides a powerful filter to eliminate

background. For events that have no timing information, the event location and energies help filter out possible background events. The energy spectrum of atmospheric neutrinos is softer than the expected signal neutrino spectrum. Atmospheric neutrinos follow a power law spectrum with an index asymptotic to $E^{-3.7}$ where most signal spectra in IceCube are expected to have a power law spectrum with an index of around -2. Higher energy events are more likely to be signal. These analysis rely on likelihood methods that a have a list of sources observed though some other detector medium such as gamma ray or optical photons. By using the time, position, and energy of these events, it is possible to determine the likelihood that an event is signal vs. background.

Newer techniques have expanded our ability to distinguish neutrinos from background. The specific techniques relevant to this search are discussed in chapter 4.

1.3.3 Beyond Cosmic Rays

As with the expansion of astronomy into new wavelengths such as radio or gamma rays, it is possible that the observation of neutrinos could lead to the new and unexpected insight into the universe. The IceCube Neutrino Observatory has begun to observe high energy neutrinos that as of yet have no identified sources. The observation of these neutrinos independent of any known source provides the opportunity to examine unexpected sources of generation. Model independent searches will be able to explore the possibility that known light sources could be generating neutrinos in unexpected ways. This analysis looks for correlations of astrophysical neutrinos with GRBs beyond the standard expectations and begins to explore not only the expected neutrino production mechanisms associated with cosmic ray production but new time ranges for neutrino production in GRBs that have yet to be explored.

1.3.4 Neutrino Observatories

There are two primary very-high-energy neutrino observatories: IceCube and ANTARES. Other lower energy observatories such as Super-K, Borexino, and SNO+ are in operation or under construction and are mostly sensitive to solar neutrinos or neutrinos generated in nearby supernovae. The IceCube observatory is discussed in chapter 3 in detail.

ANTARES is a high energy neutrino detector located in France in the Mediterranean Sea. It has a surface area of about 0.1 km^2. Similar to IceCube, it uses the Earth as a filter for atmospheric muons generated in cosmic ray air showers; though, it has a lower energy threshold and is targeted at lower energy events. Due to it's location in the Norther Hemisphere, it can be used to explore the Southern Hemisphere sky including the galactic center acting as a complementary experiment to IceCube which primarily observes the Northern Hemisphere. ANTARES has very similar goals to IceCube and is also searching for the neutrino signature of cosmic ray production along with other sources of neutrinos. Currently, there is work being done to expand ANTARES into a new detector called KM3Net which will increase the volume of the detector and theoretically raise the energy of the observable events in the detector.

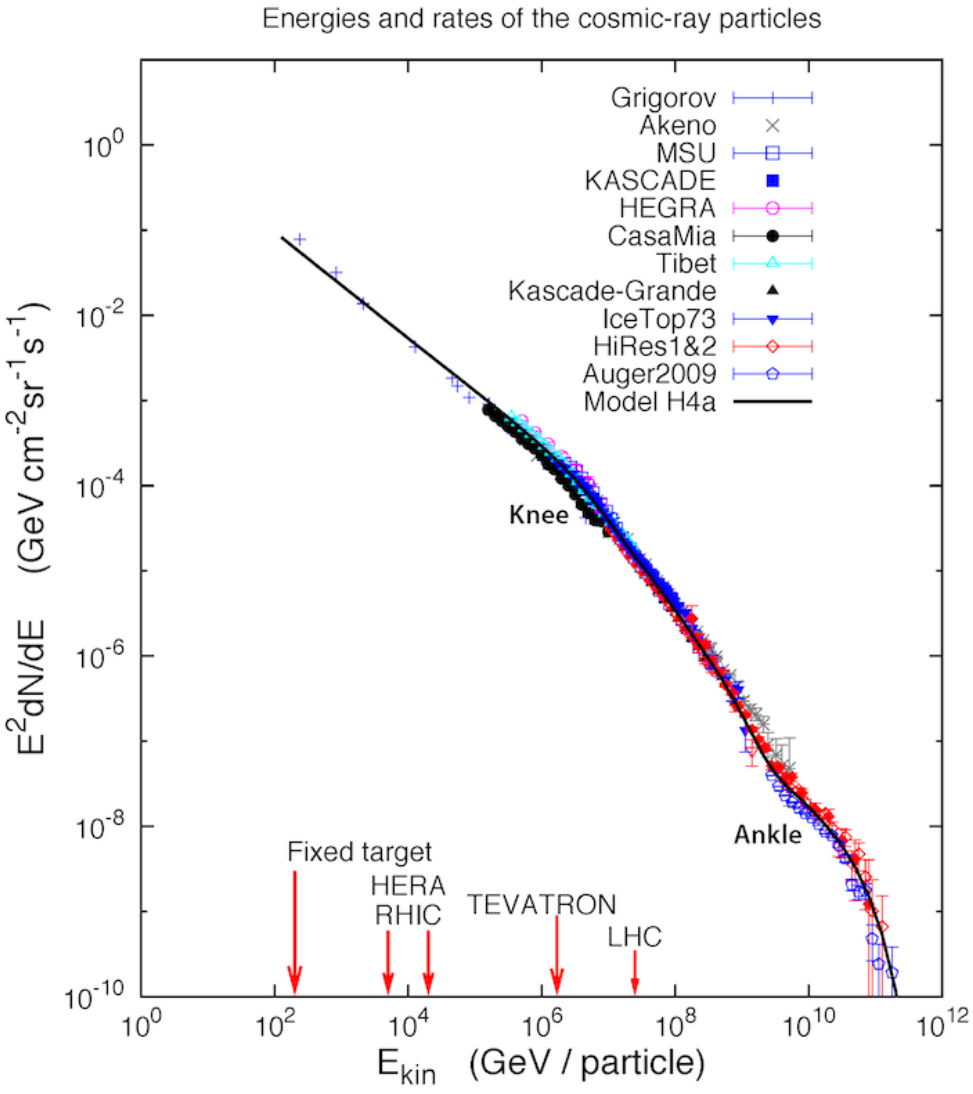

Figure 1.9: Cosmic ray spectrum as measured by various experiments. The sources of cosmic rays is is still a mystery. IceCube was designed to help answer the question of where UHECRs originate by detecting neutrino counterparts. Figure from the IceCube collaboration.

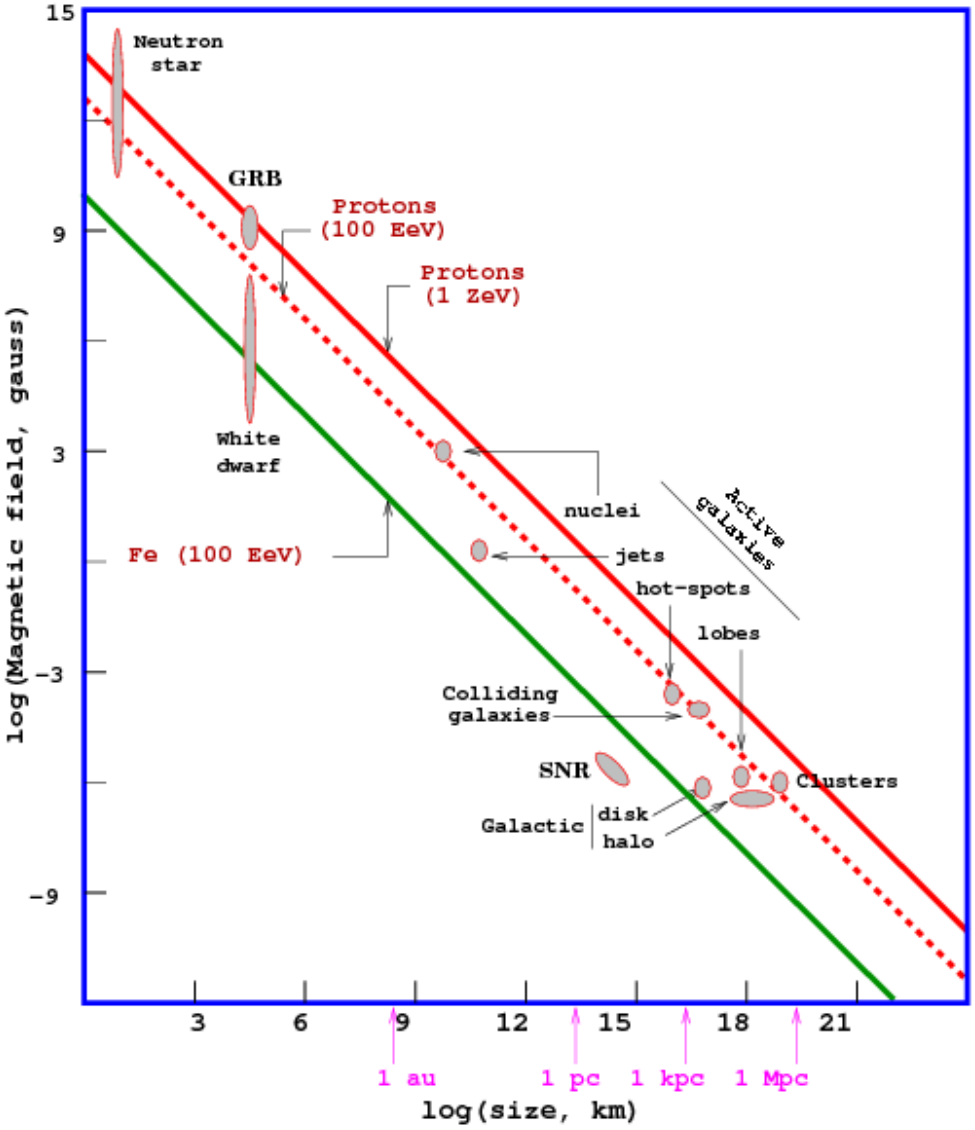

Figure 1.10: Hillas Plot. The solid red line represents objects which can accelerate protons to 10^{21} eV, the dotted red line represents protons accelerated to 10^{20} eV, and the green line represents iron accelerated to 10^{20} eV [29]

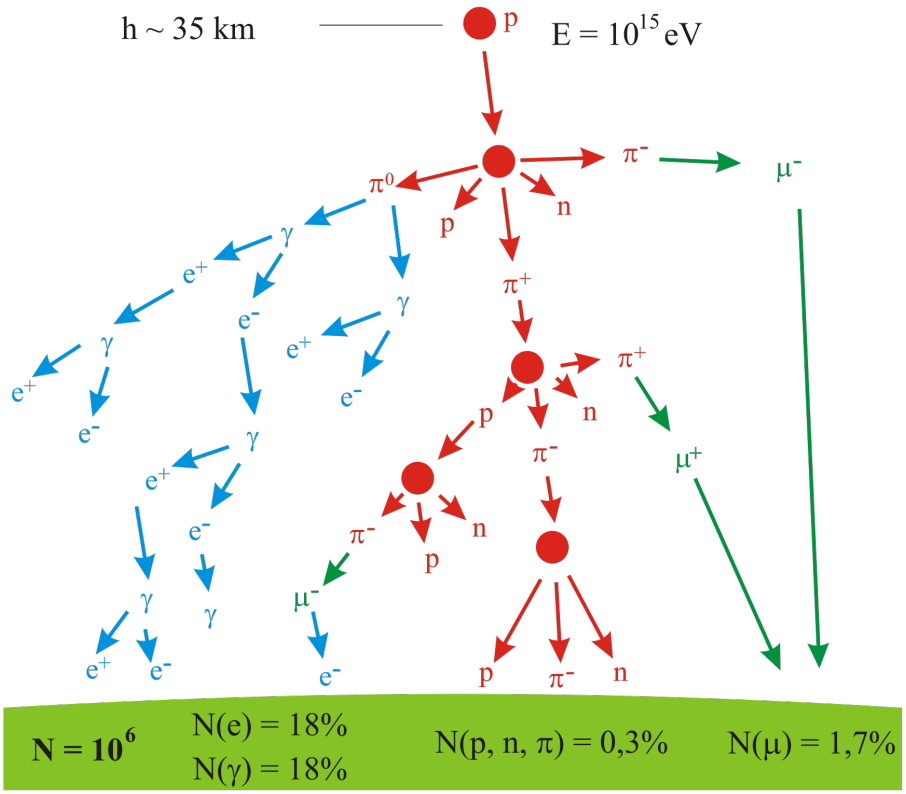

Figure 1.11: Cosmic Ray Air Shower. Cosmic rays interact in the upper atmosphere generating showers of particles that can extend down to the surface of the Earth. Figure from IceCube.

CHAPTER II

GAMMA-RAY BURSTS

Gamma-ray bursts (GRBs) are some of the most energetic events in the known universe with observed energies to over 10^{52} ergs [30]. GRBs are extremely bright flashes of keV to MeV light with components sometimes extending up to GeV energies [31]. Since GRBs were first discovered, they have been of great interest to physicists. Due to the extremely high observed energies, GRBs have been proposed as sites for cosmic ray acceleration for the highest energy cosmic rays and may be able to give insight into many particle physics processes that can not be replicated here on Earth. GRBs are also seen at extreme distances that make them useful for cosmological research.

2.1 History

GRBs were first observed in 1967 by the Vela satellites which were initially launched by the U.S. Department of defense to detect possible violations of the Nuclear Test Ban Treaty. The observations of the first GRBs were unintentional and unexpected. The observed high fluence from the bursts led astronomers to conclude that GRBs must be local to our galaxy and a number of possible source candidates were proposed [32]. In 1991, the Compton Gamma Ray Observatory (CGRO) was launched with the Burst And Transient Source Experiment (BATSE) where the primary science objective of BATSE was to study GRBs. Through the data collected by BATSE, GRBs were shown to have a uniform spatial distribution as seen in figure 2.1. The lack of clustering in the galactic plane gave support to the notion that GRBs were extra galactic in nature and far more energetic than originally expected [30]. Starting in 1997 BeppoSAX began to identify extra-galactic objects associated with the bursts and eventually was able to identify an X-ray afterglow from the observed GRBs. Using the X-ray after glow, the location of GRBs were able to be resolved to much better locations. This led to the observation of an optical afterglow that gave even higher precision measurements of GRB locations. These observations were able to confirm that the

locations of GRBs were on cosmological distances and in fact not local to our galaxy [33].

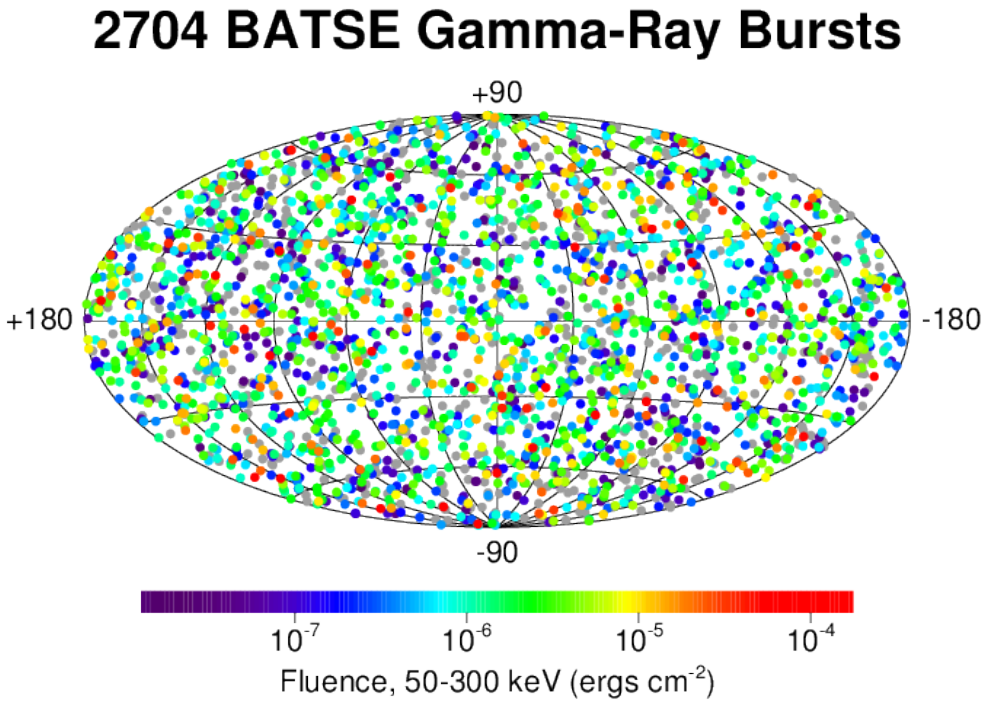

Figure 2.1: BATSE GRB Skymap. The fluence of the GRBs is indicated by the coloring. The uniform distribution of the GRBs in space was a major indication that GRBs are extra-galactic in nature [34].

Recent observations through modern satellites have begun to explore the structure of the GRB spectra with greater detail including observations of afterglows and X-ray flairs.

2.2 GRB Physics

The source mechanisms of GRBs are still not well understood and are an active area of research. GRBs are generally separated into two categories based on the duration of the burst. The duration T_{90} is measured by the time it takes to receive 90% of the photons from the burst. There is a phenomenological separation made for bursts with durations greater than two seconds and those with shorter durations. Figure 2.2 shows the bimodal distribution of bursts in time as observed by BATSE. Long bursts are bursts that extend

beyond two seconds with a peak of the distribution at around 30 s, and short bursts are limited to two seconds or less with a peak in the distribution around 0.3 s [35]. The different time scales are one indication that the bursts have different progenitors; though, the details of physics is similar for both types.

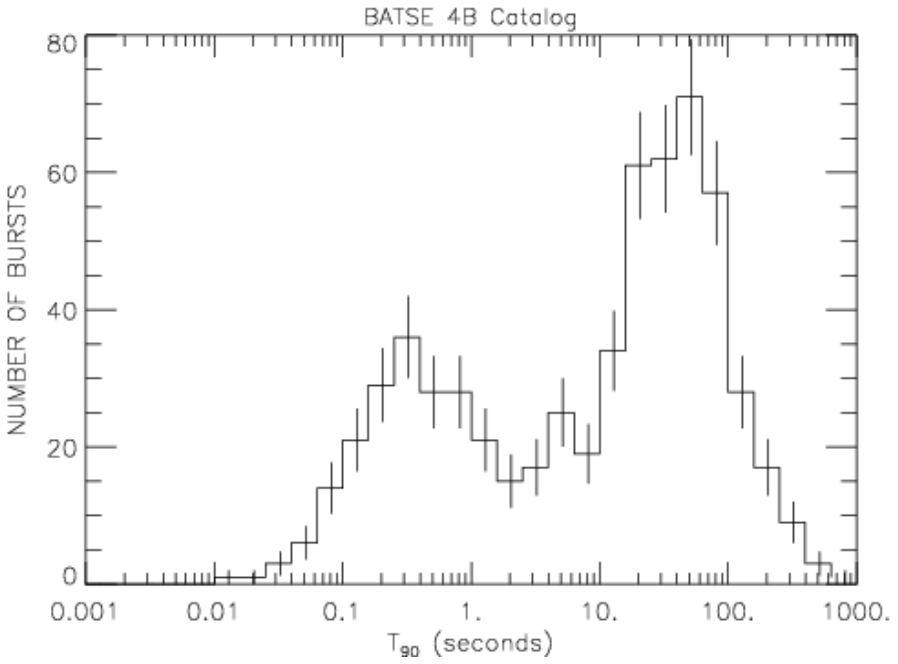

Figure 2.2: GRBs are classified by the time it takes to observe 90% of their signal counts. The bimodal distribution is thought be as a result of two separate GRB mechanisms. Short bursts are believed to be the result of compact binary mergers such as neutron start-neutron star or neutron star-black hole mergers, and long bursts are the believed to be the result of core collapse supernovae. Figure from [35].

Long bursts are thought to be generated in core collapse supernovae, and have even been observed in conjunction with Type Ic supernovae [33]. Long bursts also tend to have softer spectra [36,37]. Short bursts are believed to be generated in compact binary mergers such as neutron star-neutron star or neutron star-black hole mergers where the short times are consistent with more compact objects. Short bursts tend to have harder spectra and fewer features in their spectra [36,37]. In both cases, GRBs are created when matter rapidly accretes onto the surface of a black hole forming relativistic jets of particles. These jets focus most of the energy of the to a small area of the sky and reduce the energy budget required for the observed GRBs.

Most of the gamma-ray energy of a GRB is released during the prompt phase where the keV to MeV photons that give gamma ray burst their name are generated. The observed GRB spectrum the typically follows a broken power law where some bursts have an additional high energy tail that can extend up to GeV energies. The Band function, depicted in figure 2.3 and given in equation 2.1, is a phenomenological function used to describe the broken power law function of the GRB spectrum. The Band function describes the gamma ray emission well, but it has no theoretical basis.

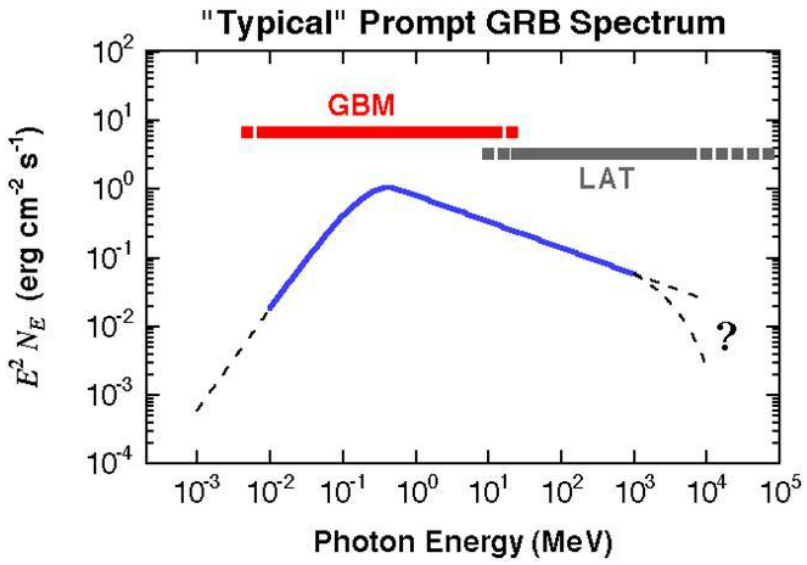

Figure 2.3: A Typical GRB Spectrum. The spectrum is follows a broken power law called the Band function. The Band function is a purely phenomenological fit to the data and has no theoretical basis. The lower energies are observable by the Fermi GBM and the higher energies are observable by the Fermi LAT as depicted by the red and gray regions on the plot. Figure from [38].

$$N(\nu) = N_0 \begin{cases} (h\nu)\exp\left\{(-\frac{h\nu}{E_0})\right\} & \text{for } h\nu < (\alpha-\beta)E_0 \\ [(\alpha-\beta)E_0]^{(\alpha-\beta)}\,(h\nu)^{\beta}\exp\{(\beta-\alpha)\} & \text{for } h\nu < (\alpha-\beta)E_0 \end{cases} \tag{2.1}$$

The high energy tail is also of interest and is described as a single unbroken power-law with some cutoff at high energy. Currently this cutoff energy is not well known and many ground based detectors are hoping to explore this energy region of the GRB to explore possible emission mechanisms.

Most GRBs continue to emit light after the prompt phase in what is called the afterglow

phase. The afterglow is mostly observed in the X-ray regime, but sometimes has optical and infrared components as well. This afterglow can extend for days after the burst and believed to be caused by the interaction of relativistic jets interacting in the medium around the progenitor. The spectra of these afterglows have a power law dependence on the frequency ν and observed time t. The relationship is given by equation 2.2 where $\alpha \sim 1.4$ and $\beta \sim 0.9$ [39].

$$f_\nu(t) \propto \nu^{-\beta} t^{-\alpha} \tag{2.2}$$

Originally, the afterglow was believed to be well understood, but more observations have begun to show structure in the afterglow (figure 2.4. This structure takes the form of X-ray flares. These flares are thought to be the result of late activity of the central engine of the GRB and generated in shocks similar to the prompt phase.

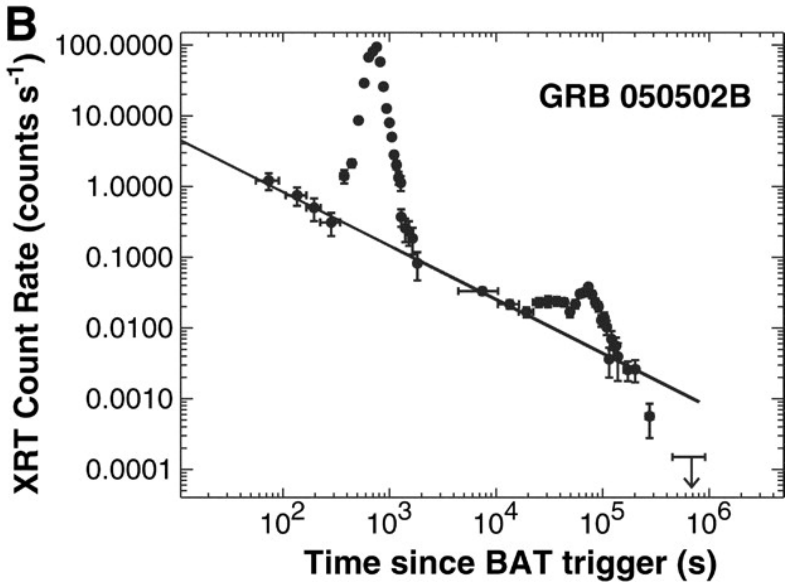

Figure 2.4: Lightcurve from an X-ray Flare. The observed flaring is believed to as a result of late activity from the central engine of the GRB. Figure from [40].

2.2.1 The Fireball Model

One of the leading models for GRB production is the Fireball model (see [30,33,41] for more detailed description). Observed variability on time scales on the order of milliseconds [42] in the rate of observed photon counts or lightcurves of GRBs imply that the emission region must have a relatively short light crossing time or the variability in the lightcurve would be

smeared out. This fact, combined with the large amounts of energy released, on the order of 10^{52} ergs in a few seconds, creates a problem for GRB emission. Relativistic bulk motion in the Fireball model provides a solution to this problem.

In this model, GRBs are produced when matter rapidly accretes onto the surface of a black hole forming relativistic jets of plasma along the spin axis of the black hole. The plasma in the jets is opaque to photon-photon pair production due to high densities and is composed of electron and positron pairs and thermal photons. The energy injected into the system accelerates as small mass M of baryons in the matter surrounding the core which is accelerated to a Lorentz factor $\Gamma \approx E/Mc^2$ of several hundred due to the large amounts of energy being injected. The matter around the black hole accretes somewhat non-uniformly causing the formation of shells in the plasma with different Lorentz factors. As these shells collide due to their varying velocities, internal shocks are formed in the jets. As the shock passes through the outer layers of matter surrounding the compact object, electrons and some baryons are accelerated through first order Fermi acceleration [43], though the baryon loading is not well known. Figure 2.5 gives a simple cartoon illustration.

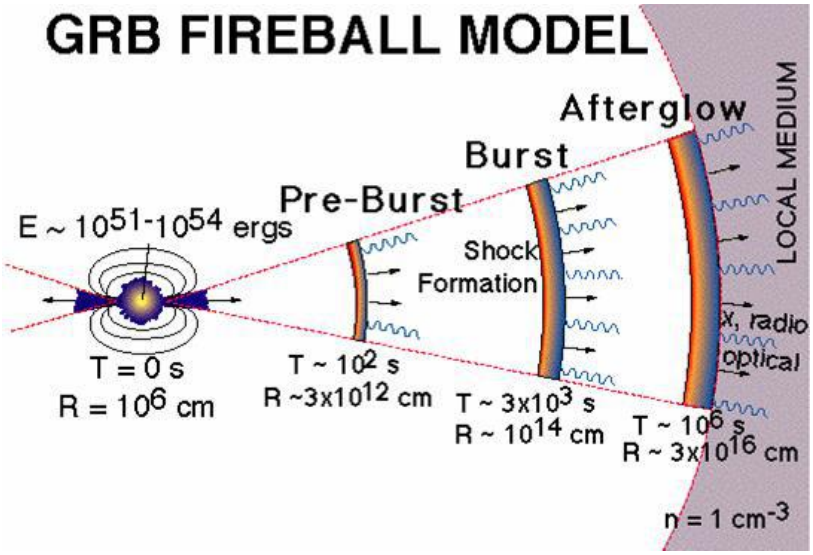

Figure 2.5: Simple Depiction of the Fireball Model. Relativistic jets are formed when matter accretes on the surface of a compact object such as a black hole. Due to variability in the accretion rate, shells of various bulk velocities are formed causing shocks to form as shells of differing velocity collide. Particles are accelerated in these shocks and will eventually generate gamma rays, cosmic rays, and neutrinos. Figure from [44].

First order Fermi acceleration takes place as charged particles are accelerated as they pass across shocks of material with different bulk velocities. The particles are confined to the acceleration region through the strong magnetic fields and may cross over the shock many times increasing their energy.

For a material moving with bulk velocity u_1 overtaking a material with bulk velocity u_2 (figure 2.6), the energy gained at each crossing is shown in equation 2.3.

$$E_{k+1} = \left(1 + \frac{4}{3}(u_1 - u_2)\right) E_k \tag{2.3}$$

The energy E_k is the energy for a particle after the kth crossing. The energy spectrum for a system of many particles undergoing first order Fermi acceleration is given by a power-law (equation 2.4.

$$\frac{dN}{dE} \propto E^{-\gamma} \tag{2.4}$$

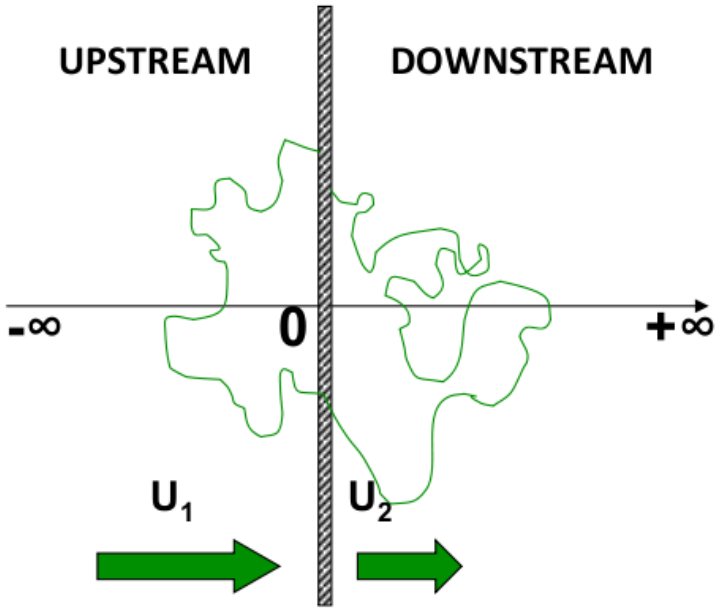

Figure 2.6: First Order Fermi Acceleration. Particles are accelerated as they are reflected back and forth across the a shock formed when a region of higher bulk velocity overcomes a region of lower bulk velocity. Figure from [45].

When the bulk matter reaches the photosphere, it begins to cool and becomes transparent to gamma radiation causing gamma-rays generated by energetic electrons through synchrotron radiation and/or Inverse Compton radiation to escape.

As the jet expands into the interstellar medium (ISM), it interacts with surrounding medium and decelerates forming external shocks. These shocks will again accelerate electrons to produce synchrotron radiation that forms an X-ray afterglow phase in the GRB. Shocks may also reverse and propagate backward on to the ejected material forming reverse shocks that generate lower energy afterglows in the optical and UV. The observed afterglow of several bursts is consistent with the predictions from the Fireball model [46] and in particular, relativistic flows [47].

2.3 Neutrino Production

GRBs have been proposed as sources for the highest energy cosmic rays. In particular, in the Fireball model it is believed that electrons are accelerated in internal shocks inside the relativistic jets. Protons and heavier nuclei present in these shocks undergo similar acceleration.

Protons accelerated in internal shocks can be up scattered by high energy photons to form δ-resonances. These δ particles will then decay into protons, neutrons and pions. The pions then decay into muons and neutrinos. Finally, the resulting muons will decay into positrons and neutrinos.

$$p + \gamma \longrightarrow \Delta^{+} \longrightarrow \begin{cases} p + \pi^{0} & \frac{2}{3} \text{ of the time} \\ n + \pi^{+} & \frac{1}{3} \text{ of the time} \end{cases} \tag{2.5}$$

The π^0 will decay into gamma rays where equation 2.6 shows the decay channels of the π^+ into a muon-neutrino pair. The muon then decays into a positron, and two more neutrinos.

$$\begin{aligned} \pi^{+} \longrightarrow \quad & \mu^{+} + \nu_{\mu} \\ & \mu^{+} \longrightarrow e^{+} + \nu_{e} + \bar{\nu}_{\mu} \end{aligned} \tag{2.6}$$

The energies of the decay products of the π^+ are all roughly equal, and the energies of the neutrinos produced in these interactions are about 5% of the initial proton. The energy of the proton can be estimated from the energy of the photon in the observers frame using equation 2.7 where ϵ_γ is the energy of the photon, ϵ_p is the energy of the proton, and Γ is the bulk Lorentz velocity with a value on the order of hundreds. This is based on the

energies needed to reach a Δ-resonance.

$$\epsilon_\gamma \epsilon_p = 0.2\text{GeV}^2\Gamma^2 \tag{2.7}$$

Using a typical photon energy of around 1 MeV, the energy of the photons can be seen to be $> 10^{20}$ eV leading to neutrinos with energies on the order of 10^{14} eV.

The neutron in equation 2.5 will also decay with a neutrino produced, but the energy of this neutrino is much lower energy than the other neutrinos and will be below the observable threshold.

It is also possible to have proton-proton interactions that will generate pions that will also decay following equation 2.6 into neutrinos.

$$p + p \longrightarrow \pi^+ + X \tag{2.8}$$

The final result is a neutrino flux with a flavor ratio of $\Phi_{\nu_e}:\Phi_{\nu_\mu}:\Phi_{\nu_\tau} = 1:2:0$.

Almost all previous GRB-neutrino searches have focused on neutrinos generated during the prompt phase where the Fireball model generally predicts neutrino production coincident with gamma rays as described above. Previous searches have exploited this fact to reduce neutrino background by looking only for neutrinos coincident with the prompt lightcurve of the GRBs. Newer models have begun to predict neutrino production through interactions beyond the prompt phase causing the need to explore these new regimes.

2.3.1 Precursor

Most neutrino models show strong motivation for neutrinos generated in or after the burst, but it has also been suggested that GRBs could be connected to super nova remnants (SNRs) in which GRBs may follow weeks after a core collapse super nova (SN) [48]. The SNR shell will then provide a target for pp interactions leading the production of 10 TeV neutrinos. The protons are expected to be accelerated in MHD winds of pre-GRB pulsars [49]. In these models there is a precursor phase that is believed to start on the order of 100 s before the burst. So far, very few neutrino searches have extended their searches to the precursor phase. Of the searches that have looked for neutrinos generated in a precursor, no neutrinos have been detected that are coincident with these earlier times.

2.3.2 Afterglow

GRB afterglow emission has been attributed to interaction of the relativistic jets in the circumstellar medium [39, 50]. This is similar to the prompt phase, but involves material outside of the star. The GRB afterglow spectrum was generally believed to be dominated by synchrotron emission. However recent observations by swift have begun to challenge this view. The observations show features such as an initial steep decay followed by a plateau phase and flares that are difficult to explain in the earlier models. It has been suggested that a forward or reverse shock could explain the features seen in the afterglow spectra.

These forward and reverse shock interactions may lead to the production of neutrinos [51]. As the energies of the observed photons are much lower, the threshold for Δ-resonance causes the neutrino energies to be much higher with energies on the order of $\approx$100 PeV [52] (see equation 2.7). So far, no neutrinos have been observed in this energy range.

2.3.3 X-Ray Flares

X-ray flares are thought to be late activity of the central engine [53, 54]. These flares can have a fluence that exceeds that of the prompt phase of the GRB. They are often observed up to a day after the prompt phase, but X-ray flares have been seen as late as five days after the initial burst.

Recent models have also begun to suggest the production of neutrinos in these X-ray flares [55]. Neutrinos produced in X-ray flares are expected to be less numerous than the neutrinos produced in the prompt emission at around 1 TeV. At higher energies over 1 PeV, however, neutrino production for the flares is expected to exceeded that of the prompt emission. This fact combined with the delayed onset of the flares makes long timescale GRB-neutrino searches of great interest.

2.4 GRB Detectors

While large advancements have been made the past decades into the understanding of GRBs, there are still many aspects of GRBs that are not well understood. There are currently several observatories designed for the purpose of detecting and observing GRBs.

Through these observations, scientists hope to better understand how GRBs work.

One problem with the detection of GRBs is due to Earth's atmosphere. Thankfully, the atmosphere of the Earth is opaque to gamma rays which are actually quite harmful to life on Earth, but this makes them difficult to detect. In order to observe gamma rays and therefore GRBs, gamma-ray detectors are usually located on satellites outside the Earth's atmosphere. The *Swift* and *Fermi* satellites are dedicated to the observation of gamma rays and GRBs. Each has specific hardware designed to trigger when it detects a GRB. After a GRB has been detected by one of the satellites, an alert is sent out to the Gamma-ray Coordinates Network which forwards the information on to other gamma-ray observatories allowing them the opportunity to observe the GRB as well. These follow up observations can provide addition information such as observations in different energy bands and can provide extended observation that may not be possible for satellites that can lose site of the burst due to observational limitations.

While the majority of the initial observations of the GRBs used in this analysis were done by the *Fermi* Space Telescope or the *Swift* satellite, in many cases, follow up searches were performed by additional satellites listed below. These follow up searches contributed additional information such as better positional resolution for many of the GRBs used in this study.

2.4.1 The Gamma-ray Coordinates Network (GCN)

The Gamma-ray Coordinates Network (GCN) [56] is network run by NASA to facilitate in the sharing of GRB information in the scientific community. GCN sends out the received location of GRBs and other transients and reports of follow-up observations. GRBs detected and observed by satellites or ground-based observatories are able to send notices to GCN to circulate the information they collect through email, sockets, and pagers. The information distributed by GCN from the various observatories makes it possible for other gamma-ray and X-ray observatories to make follow up observations that can provide valuable information for the study of GRBs.

2.4.2 Fermi Gamma-ray Space Telescope

The *Fermi* Gamma-ray Space Telescope was launched in 2008. It comprises two detectors: the Gamma-burst Monitor (GBM) and the Large Area Telescope (LAT). A set of sample lightcurves for the GBM and LAT are given in figure 2.7.

The GBM is composed of twelve sodium iodide (NaI) and two bismuth germante (BGO) detectors. The NaI detectors are arranged in groups of three at each of the four edges of the spacecraft and the two BGO detectors are placed symmetrically on opposite sides of the spacecraft. It is sensitive over energy ranges of 8 keV-1 MeV and 150 keV-40 MeV. The GBM has a field of view of $\approx$9.5 sr and has a systematic uncertainty on the position of 10.4°. GRBs are first detected in the GBM where a general location is given and then afterwards located by the LAT.

The LAT is a pair production telescope composed of a 4x4 array of identical towers. Each tower includes a tracker of silicon strip planes with foils of tungsten converter interleaved, followed by a cesium iodide calorimeter with a hodoscopic layout. The array is covered with by a segmented anti-coincidence detector of plastic scintillators which are designed to efficiently identify and reject charged particle background events. It is sensitive to gamma rays in the energy range from 20 MeV to over 300 GeV. It has a field of view of $\approx$2.4 sr at 1GeV, and can provide more accurate localizations of gamma ray sources to better than 1°.

2.4.3 Swift Gamma Ray Burst Mission

The *Swift* detector is a multi-wavelength satellite observatory dedicated to the detection and observation of GRBs. Swift was launched in 2004. Swift has three different components that allow it to first detect and then perform follow up observations of GRBs and other gamma-ray sources. GRBs are first detected by the Burst Alert Telescope (BAT) which has a larger field of view. Sources can then be followed up on by the X-ray Telescope (XRT) and the Ultraviolet/Optical Telescope (UVOT). A sample lightcurve from *Swift* is shown in figure 2.8.

It has an energy range of 15-150keV for imaging and a non-coded response up to 500 keV. The BAT can calculate an initial burst position within a few seconds. The field of

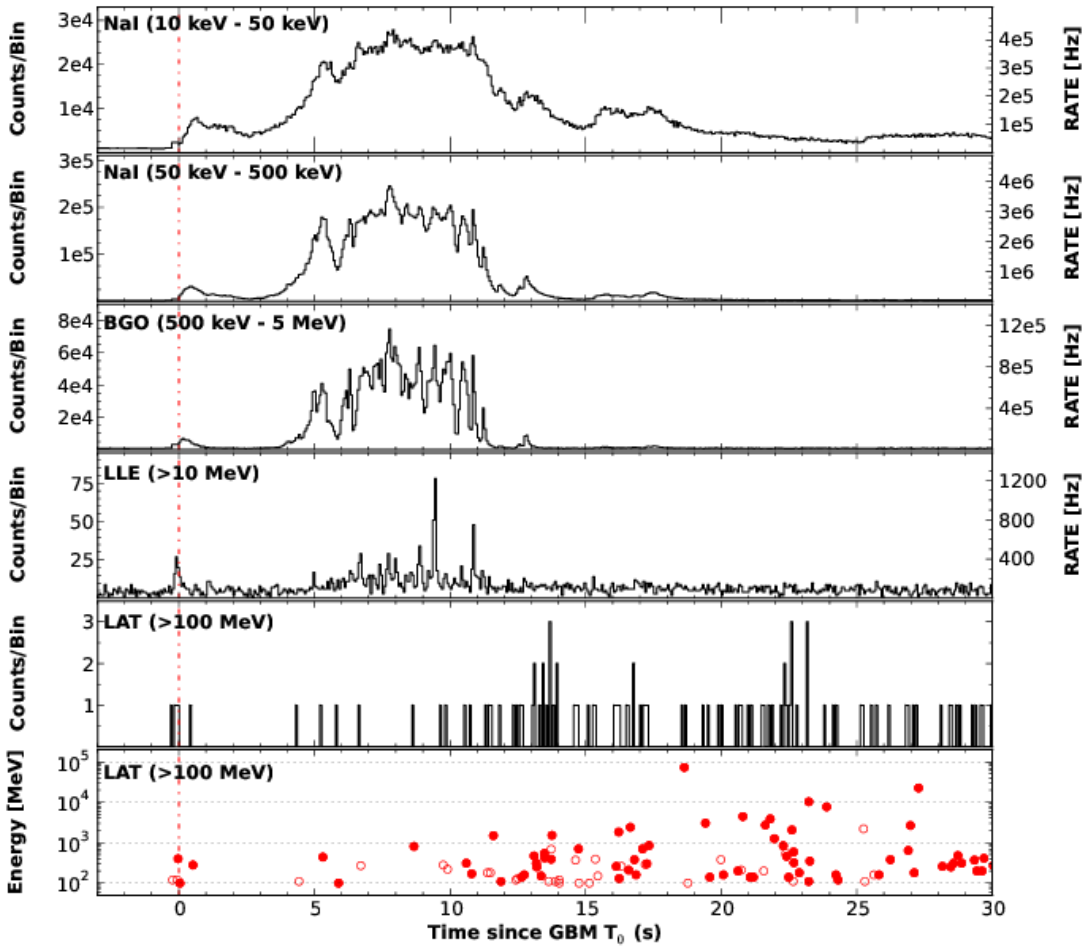

Figure 2.7: Lightcurve for GRB 130427A from the *Fermi* Space Telescope. This is a sample lightcurve for a bright burst in *Fermi*. Figure from [57].

view of the BAT is 1.5 sr and it has a resolution up to 4 arcmin. The BAT is able to detect bursts by using a two-dimensional coded aperture mask and a large area solid state detector array. Due to the overlap of the BAT field of view with the field of view of the XRT and UVOT, data can be simultaneously taken with the BAT when observing X-ray and UV/optical emission [58, 59].

The XRT on swift has an energy range of .2-10 keV and is designed to measure the fluxes, spectra, and lightcurves of GRBs and GRB afterglows. It is able to locate typical GRBs to an accuracy of 5 arcsec within 10 s of target acquisition. Within 20 to 70 s from

the discovery of the burst, it will be able to start studying X-ray counterparts to the GRB where it can continue for weeks [60].

Finally the UVOT is designed to study the optical and ultraviolet components of GRBs and GRB afterglows. The UVOT observations make it possible for ground-based observations as well by providing optical imaging through its 2048x2048 pixel CCD. It has a field of view of 17 x 17 arcmin [61].

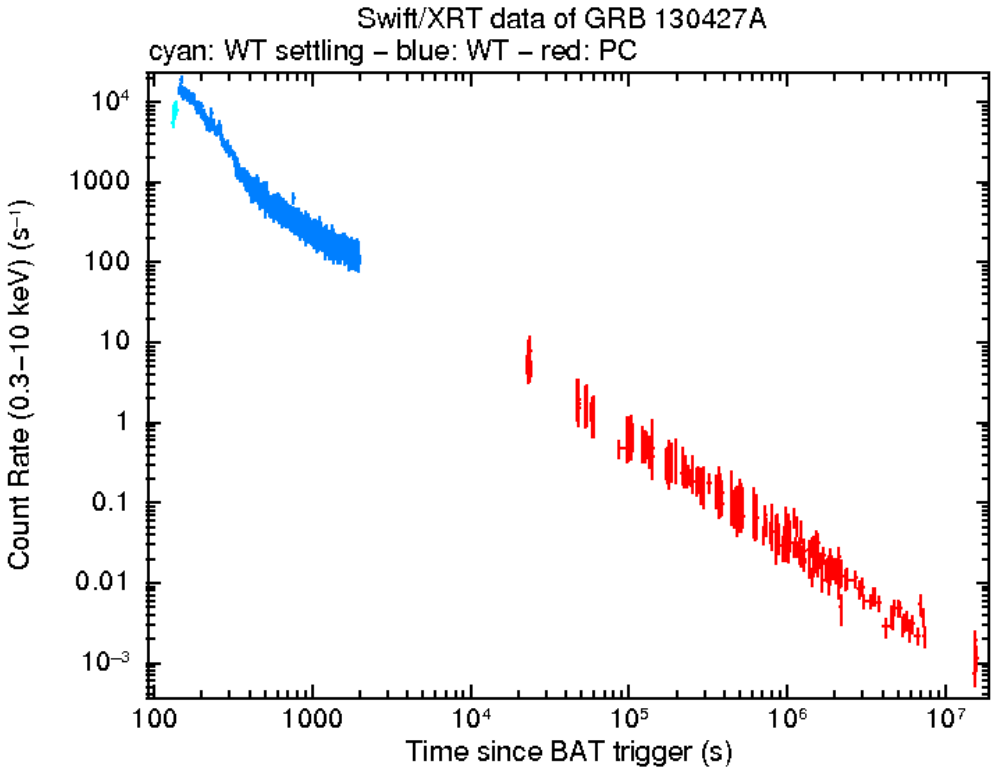

Figure 2.8: Light Curve for GRB 130427A from the *Swift* Observatory. This is a sample lightcurve for a bright burst in *Swift*. Figure from [62].

2.4.4 INTEGRAL

The INTErnational Gamma-Ray Astrophysics Laboratory (INTEGRAL) was designed to observer gamma rays, X-rays, and optical light simultaneously. It was launched in 2002 by the European Space Agency (ESA). The primary gamma-ray instrument has an energy range from 20 keV to 8 MeV and a field of view of up to 31° with an angular resolution of 2.5° [63–65].

2.4.5 Konus-WIND

The WIND spacecraft was launched in 1994 by NASA to study solar winds. It is currently located at the L1 Lagrange point and has enough fuel to remain in orbit for several more years. The KONUS experiment on the WIND spacecraft is a gamma ray detector that is used to monitor GRBs. It is able to provide GRB timing information including the start time of GRB used in this analysis [66] but has poor directional resolution.

2.4.6 MAXI

The MAXI detector is an experimental payload located on the International Space Station. It has been in operation since 2009. MAXI has a energy range from 2 to 30 keV. It has a field of view of $3^\circ \times 160^\circ$ [67, 68].

2.4.7 AGILE

The AGILE [69–71] satellite was launched in 2007 by the Italian Space Agency (ASI) with one of its primary objectives to study GRBs. It is composed of three detectors: the Gamma-Ray Imaging Detector (GRID), Super-AGILE (SA), and the CsI Mini-Calorimeter (MCAL). The GRID is gamma ray detector with an energy range of 30 MeV-50 GeV and an angular resolution on the order of 30 arcmin for intense sources. The field of view is around 2 sr. Combined with the GRID is the MCAL which provides spectral and timing information. SuperAGILE is a hard X-ray detector and has an energy range of 10-50 keV with an angular resolution of 10 arcmin. The field of view is $60^\circ \times 60^\circ$.

2.4.8 Suzaku

Suzaku is a Japanese X-ray observatory and satellite launched in 2005 [72]. It has an energy range of 0.3 to 600 keV. It comprises several components. The X-Ray Telescope (XRT) has a field of view of 17 arcmin at 1.5 keV up to 13 arcmin at 8 keV and an angular resolution of 2 arcmin. The X-Ray Imaging Spectrometer (XIS) has a field of view of 17.8×17.8 arcmin. The energy range is 0.2-12 keV with an energy resolution of $\approx$130 eV at 6 keV. Finally the Hard X-ray Detector (HXD) has field of view of $4.5^\circ \times 4.5^\circ$ at energies greater than 100 keV and down to 34×34 arcmin for energies below 100 keV.

2.4.9 Ground Based Detectors

While gamma rays are unable to penetrate through Earth's thick atmosphere, it is still possible to make observations of GRBs on the surface of the earth. Ground based observatories are able to make direct observations of GRBs in the optical and X-ray frequency bands. This can provide valuable information on the location and properties of GRBs.

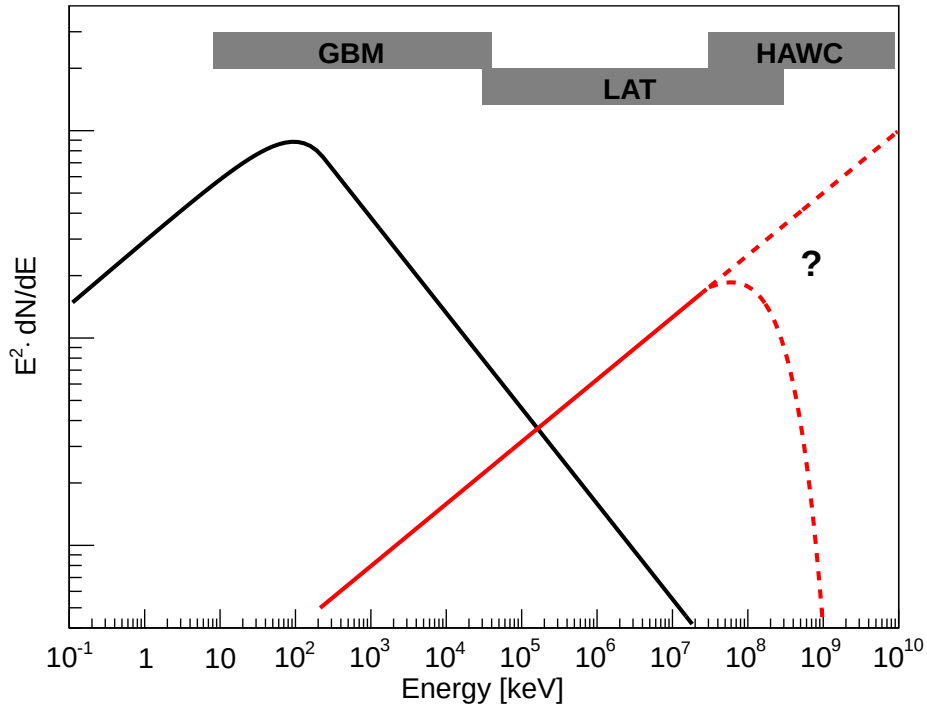

Figure 2.9: High Energy Tail Found In Some GRBs. This energy tail extends beyond the observable energies for satellite observatories. Ground based gamma ray observatories may one day be able to observe the cutoff energy and determine the mechanisms generating the tail. Figure from [73].

Optical observatories can provide greater position resolution and spectroscopy. There are also ground based detectors such as HAWC, VERITAS, and eventually CTA that are working to observe higher energy components of GRBs through various air or water Cherenkov methods. These detectors have a much higher energy threshold allowing them to observe GRBs up to GeV and TeV energies which is more difficult for satellites due to their limited sizes. One goal of these ground based gamma ray detectors is to determine the cutoff energy of bursts that show an extra power law component as seen in figure 2.9.

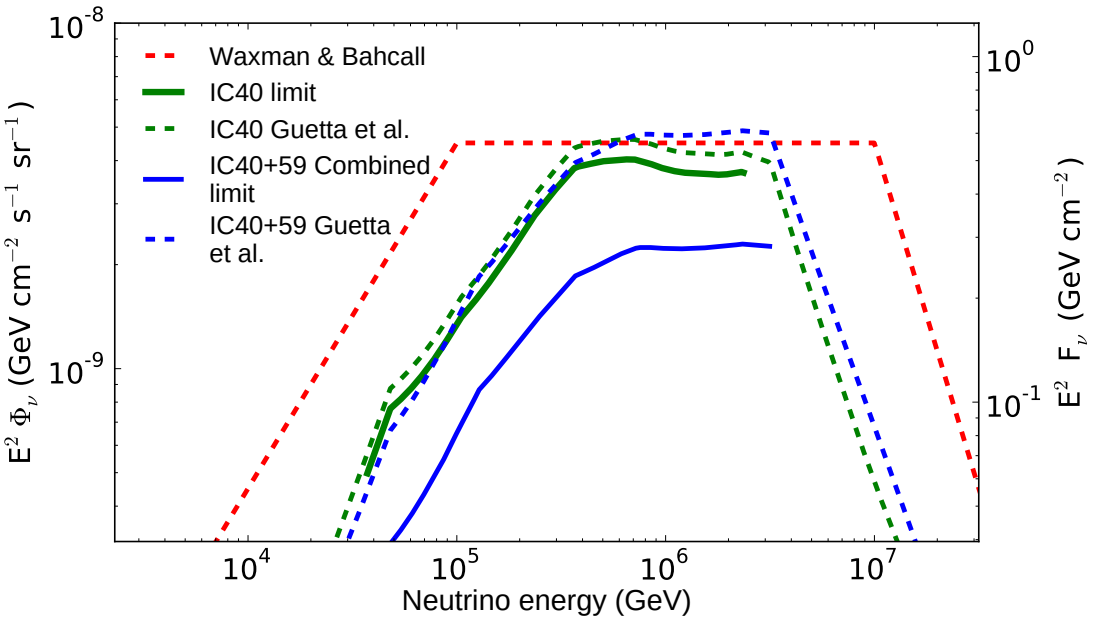

Figure 2.10: Figure from [75].

So far, this cutoff has only been observed in one GRB [74] and is still not well understood.

2.5 GRB Neutrino Searches in IceCube

There have been several searches for neutrinos generated in GRBs using the IceCube Neutrino Observatory (chapter 3). Previous searches have focused on muon neutrinos primarily from GRBs in the northern hemisphere [75–77]. These searches also looked for neutrino events coincident with the GRB prompt emission and, to a lesser extent, possible precursor and afterglow emission. So far, these searches have shown no significant correlations with IceCube events and the observed GRBs.

A search was performed for GRB-neutrinos using two years of data from April 2008 to May 2010 with 40 and 59 string configurations [76]. The search focused on muon neutrinos from 215 Northern hemisphere GRBs. No significant correlations were found allowing the rejection of the fireball model by Guetta et al [78]. Figure 2.10 shows the flux prediction from Guetta et al. compared with the limits on the flux due to the non-observation in IceCube.

This null result prompted a revision of the estimates for the number of neutrinos generated in this model. While the foundations of these model are similar, the calculations have been improved to lower the neutrino signal expectation by an order of magnitude. Nevertheless, the models remain within the realm of observation with IceCube through a few more years of observation.

This search was also able to reject neutron escape models [79]. In these models protons are confined in the burst by magnetic fields and cosmic rays are entirely attributed to the beta decay of neutrons produced from Δ-resonances from γp interactions

$$\gamma + p \longrightarrow \Delta \longrightarrow n + \pi^{+}. \tag{2.9}$$

The neutron flux is directly weighted to the observed cosmic ray spectrum. The neutrino flux can then be determined directly from the neutron flux.

A similar search to the one presented here was performed over the same time frame as the above analysis, but included Southern hemisphere GRBs for the IC-59 season. This was a model independent search for GRB neutrinos that relied on overlapping time windows centered on the earliest reported detection time of the burst. The search was a likelihood search for neutrino events coincident in time and space with a stacked list of GRBs. Unlike other IceCube GRB neutrino searches, longer time windows were explored around the burst where time windows up to 10,000 s were reported. Two coincident events were found with low significance giving no significant correlations between the neutrinos and GRBs. Figure 2.11 shows the upper limits for general precursor with emission up to 100 s before the prompt emission and afterglow models with emission as late as 1000 s after the prompt emission.

A four year GRB-neutrino search using data collected from May 5, 2008 to May 15, 2012 was recently completed by the IceCube Collaboration [80]. This search examined 506 bursts located in the Northern hemisphere. The analysis was a likelihood search that focused on the prompt phase of the GRB using track like events from ν_μ charged current interactions. One neutrino was observed in coincidence with the GRBs with a p-value of 0.33 allowing IceCube to continue to set upper limits on GRB models predicting neutrino production. The limits

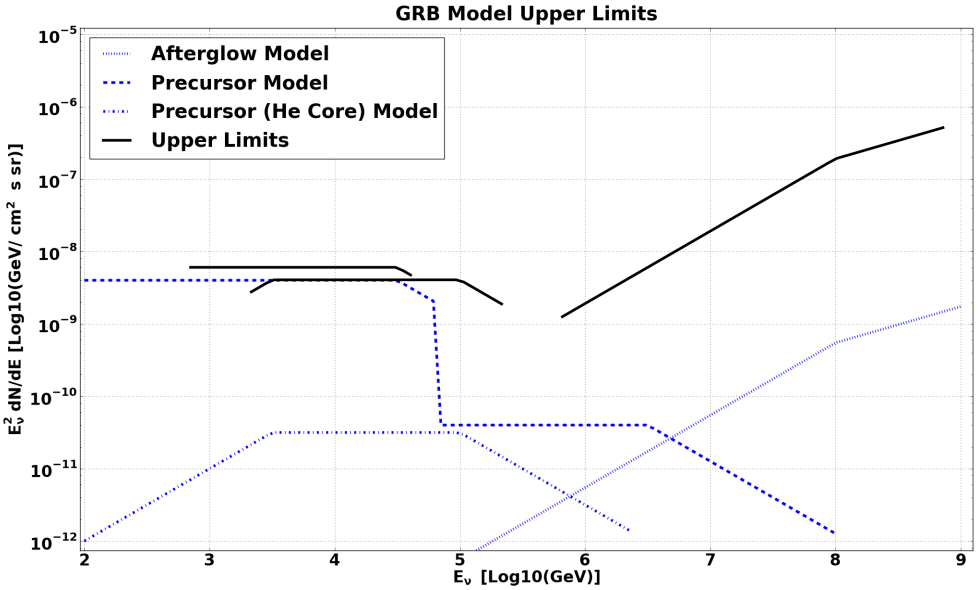

Figure 2.11: Upper Limits on Generic Models From IC-40/IC-59.

on the flux from two models are shown in figure 2.12. The figure shows the upper limits on the standard fireball model [81] (see section 2.2.1) and the photospheric model [82,83] where neutrino production is shifted to the photosphere as the fireball transitions from optically thick to optically thin for $\gamma\gamma$ interactions.

Additionally, the neutron escape models were reexamined with the full four years of data where the model was further excluded. Figure 2.13 shows the exclusion regions as a function of flux and break energy. The prediction for the neutron escape model (Ahlers) is plotted along with the case were protons are allowed to escape (Waxman-Bahcall). While the models that allow only neutrons to escape the burst are excluded, models that allow protons to escape may be disfavored but are not strongly excluded.

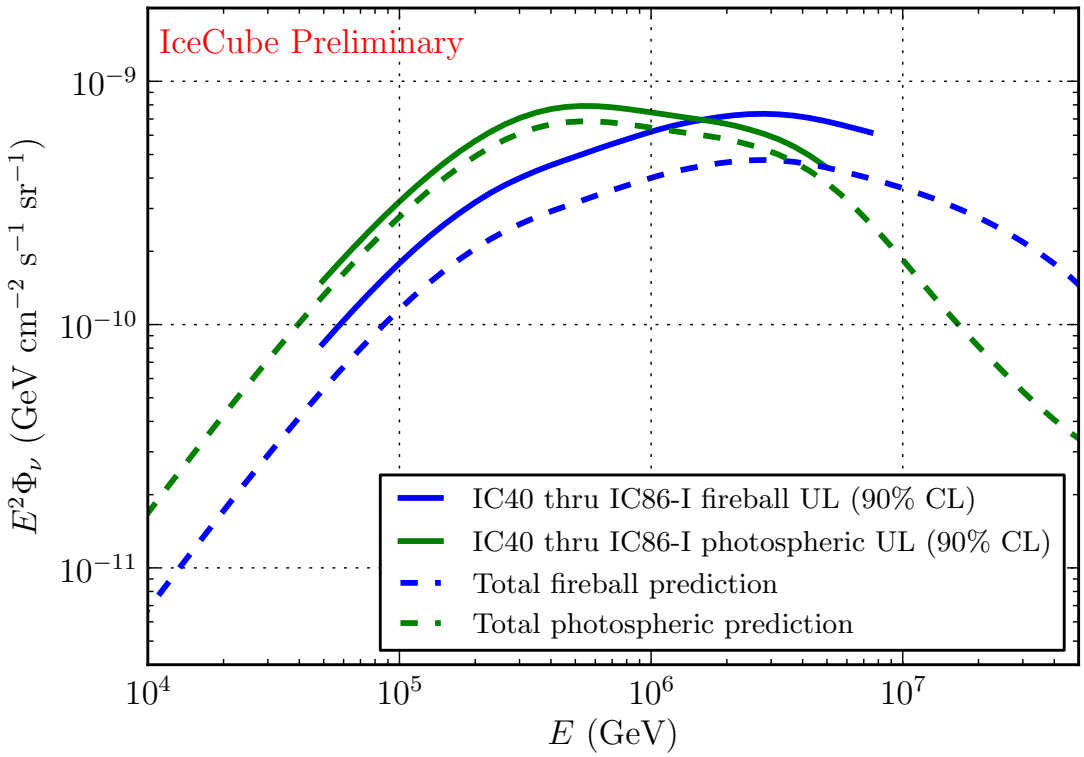

Figure 2.12: Limits on the improved fireball models. Figure from the IceCube Collaboration.

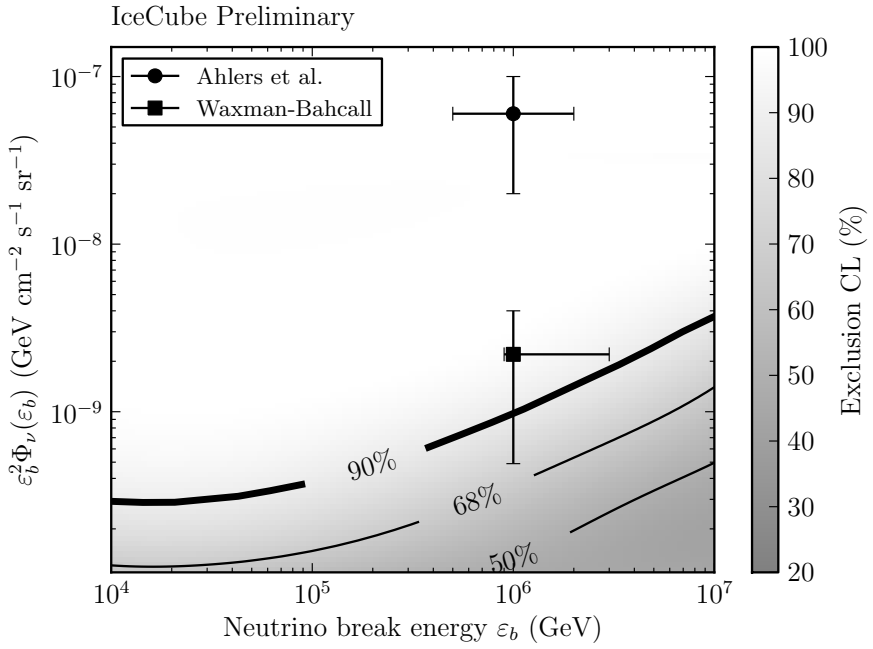

Figure 2.13: Neutron escape models in IceCube. Models where only neutrons escape to generate the cosmic ray flux are excluded. Models that allow for protons to escape are disfavored but not yet excluded. Figure from [80]

CHAPTER III

THE ICECUBE NEUTRINO OBSERVATORY

"One neutrino is a source. Two neutrinos are a spectrum. Three neutrinos are a skymap!"

— Francis Halzen, *IceCube PI*

The IceCube Neutrino Observatory is a neutrino detector located at the geographic South Pole. IceCube was constructed with the purpose of observing astrophysical neutrinos to determine the source of UHECRs. IceCube is also used in many other scientific explorations including searches for dark matter, determining the neutrino mass hierarchy, exploring the cosmic ray anisotropy, measuring neutrino oscillations, and other exotic particle and astrophysics.

IceCube is currently one of the largest neutrino detectors in operation. With its location at the South Pole it is able to observe the full sky with an emphasis on the Norther Hemisphere where the Earth below the detector acts as a filter for muons generated by cosmic rays in the atmosphere. Recently IceCube reported the observation of 35 astrophysical neutrino candidates (see Chapter 4). These are the highest energy neutrinos that have ever been observed and have started a new era in high energy neutrino astrophysics.

3.1 Hardware

IceCube comprises 5,160 Digital Optical Modules (DOMs) extending from 1,450 m to 2,450 m below the surface of the ice. The instrumented volume of IceCube is roughly 1 km^3. Each DOM is composed of an outer glass sphere that encloses a photomultiplier tube (PMT) and a set of electronics that digitizes the raw PMT output and sends it to the surface for processing. The DOMs are arranged onto 86 strings where each string consists of 60 DOMs. The strings are a arranged in a hexagonal grid. For 78 of the strings, the DOMs are separated by ≈17 m. The spacing between the strings themselves is ≈125 m. The remaining eight strings have much smaller separations and are located in the center of

the detector with a DOM separation of ≈7 m. These eight strings make up an area of the detector known as DeepCore. IceCube is sensitive to energies around 1 TeV; however, with the addition of the DeepCore sub array, searches in IceCube can extend down to 10 GeV.

IceCube also has a surface component called IceTop that is used to study cosmic rays and act as a veto for background events generate by cosmic rays above the detector. It is composed of 162 tanks organized into 81 stations. Each tank contains 2 DOMs similar to the ones used in the in-ice component of IceCube. The DOMs are frozen into the tanks and observe cosmic rays by detecting Cherenkov radiation generated by charged secondaries such as muons and electrons from cosmic ray air showers passing through the tanks.

Cosmic rays incident on the upper atmosphere also generate atmospheric muons and neutrinos that can mimic signal inside the IceCube detector. The location of the IceCube detector deep in the ice uses the ice as a filter to many of the background particles, but there is still a large background due to cosmic ray air showers. Air showers that occur above the detector are seen in IceTop, and therefore any events that are seen in IceCube from that shower are able to be discarded as background. Atmospheric muons generated in air showers that occur below the detector are blocked by the Earth. Atmospheric neutrinos generated in cosmic ray air showers below the detector are a nearly irreducible background. Figure 3.1 shows the layout of the IceCube detector at the South Pole.

IceCube began taking data early in construction. Detector configures during this time are labeled by the number of strings in operation the time of the data collection. For instance, IC-59 and IC-79 refer to configurations where 59 and 79 strings were operational respectively. Construction of IceCube was completed in December 2010, with the full 86 strings. During construction, each configuration remained static with respect to data collection for the duration of the year and the data are labeled by the configuration at that time. To avoid ambiguity for the data taking after the completion of IC-86, data are identified by appending the starting year of the data to the configuration, e.g. IC-86-2011. Figure 3.2 shows the layout of the detector as viewed from above and is color coded by the string configuration seasons.

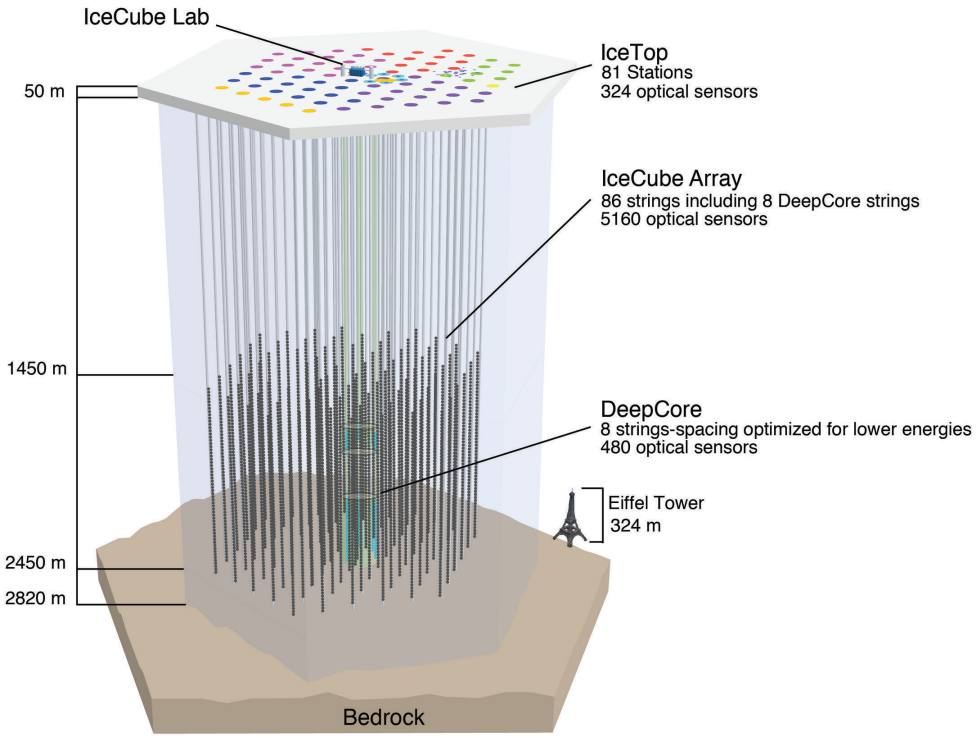

Figure 3.1: The IceCube Neutrino Observatory located at the geographic South Pole. This figure shows the layout of the detector and specifically highlights the DeepCore sub array, IceTop surface detector, and the IceCube Lab on the surface where events are processed. The Eiffel Tower is shown as a reference to the size (Courtesy of the IceCube Collaboration).

3.2 Neutrino Detection in IceCube

Neutrinos are indirectly detected in IceCube through the observation of Cherenkov radiation generated by charged secondaries from neutrino-matter interactions in the ice. High energy neutrinos interact in with a nucleon in the ice to generate hadronic showers or relativistic charged particles such as muons or electrons. Charged particles created in these interactions are moving at a velocity high enough to create light in the form of Cherenkov radiation. At the energies relevant to IceCube, the generated particles are roughly collinear with the generating neutrino [84] to within the uncertainty of the reconstructed direction.

There are two primary channels of neutrino detection in IceCube: the track channel and the cascade channel. In both channels, energy is deposited in the detector in the form of Cherenkov radiation as a neutrino scatters off of a nucleon in the ice (*see* sction 1.1).

Cascades are generated during neutral current interactions of all flavors and charged

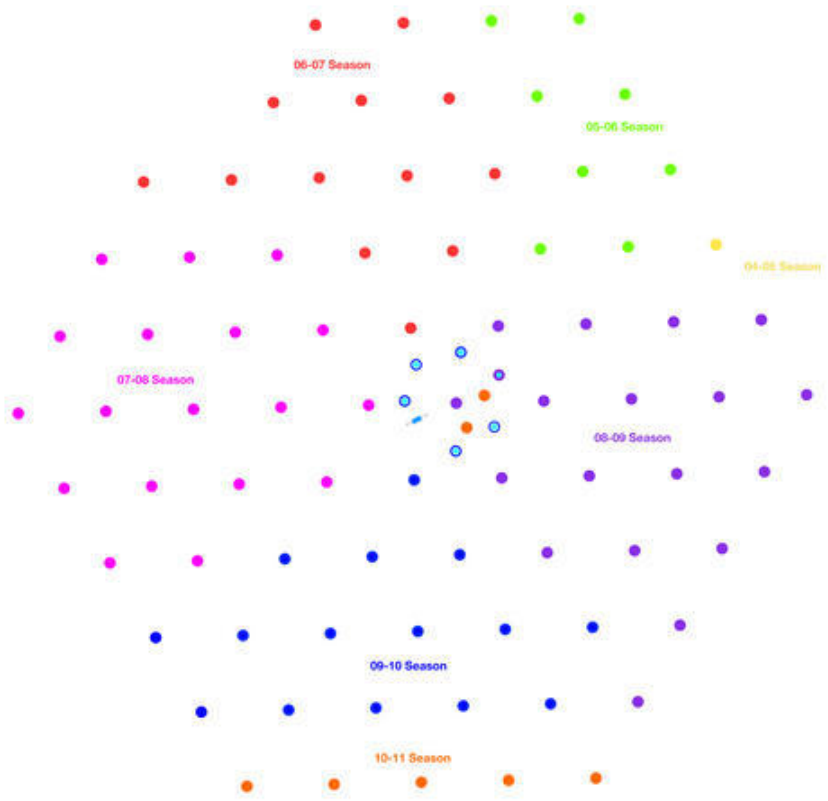

Figure 3.2: Top View of the IceCube Neutrino Observatory. The strings are color coded by the season of deployment.

current interactions from electron or tau neutrinos. Figure 3.4 shows a cascade event interacting in IceCube. In neutral current interactions a neutrino scatters off of a nucleon through the exchange of a Z boson and generates a hadronic shower. The energy from the shower is deposited in a relatively small volume compared to the spacing of the DOMs and creates a nearly spherical distribution of light in the detector. Due the spherical nature of the deposited light, directional resolution is limited; however, as the light can mostly be contained within the detector, energy resolution can be fairly accurate.

Tracks are generated in IceCube through charged current interactions of muon neutrinos. Figure 3.3 shows a track like event interacting in IceCube. In charged current interactions, neutrinos interact with nucleons through the exchange of W boson which results in the generation of lepton. Electrons and taus generated in these interactions will deposit their energy in a small space relative to the string spacing and generate cascades as described

above. Muons generated in charged current interactions have long track lengths on the order of 10 km [6] and have directional resolutions to better than 1°. Since the muon tracks are so long, the tracks will either start outside the detector or extend beyond it's boundaries and only deposit a fraction of their energy inside the detector. The energy measured for muon tracks is lower limit on the energy of the originating neutrino. The relatively good directional resolution of tracks make them more useful for astronomy.

There is another channel of detection in IceCube when a high energy tau scatters off of a nucleon in a charged current interaction. It is possible for the light deposited to have more exotic features such as a double bang that produces two cascades, but these events have not yet been observed [85]. Due to the very high mass of the tau particle, taus usually decay very quickly to other leptons. If the tau is not energetic enough, it will decay so fast that it has a signature in the detector very similar to a cascade. The IceCube collaboration is currently searching for these exotic signatures from high energy tau particles

3.3 Ice Properties

The IceCube Neutrino Observatory is located at the South Pole to take advantage of the highly transparent ice. The ice in the detector has a higher purity than any ice that can be created in the lab [86]. The effective scattering length is 25-40 m and the effective absorption length is between 100-200 m. Due to the stochastic nature of light propagating in the ice, there is some uncertainty associated with this propagation of the light in the ice.

In order to account for the properties of the ice, measurements have been taken using the built-in LEDs in the IceCube DOMs and the analogous equipment in the AMANDA detector, a precursor to IceCube. Ice properties were also measured by measuring the dust in the ice during string deployment and through various ice core samples. The results of these analyses shown in figure 3.5 have provided a description of the ice that has been confirmed through the observations of muon data in the detector. There is substantial structure to the ice as a function of depth. Some of this structure is as a result of shift in the climate over time and other geological events. The IceCube detector starts at about 1.5 km of depth. Above 1.4 km, the ice has air bubbles that can scatter light. From 2000 m

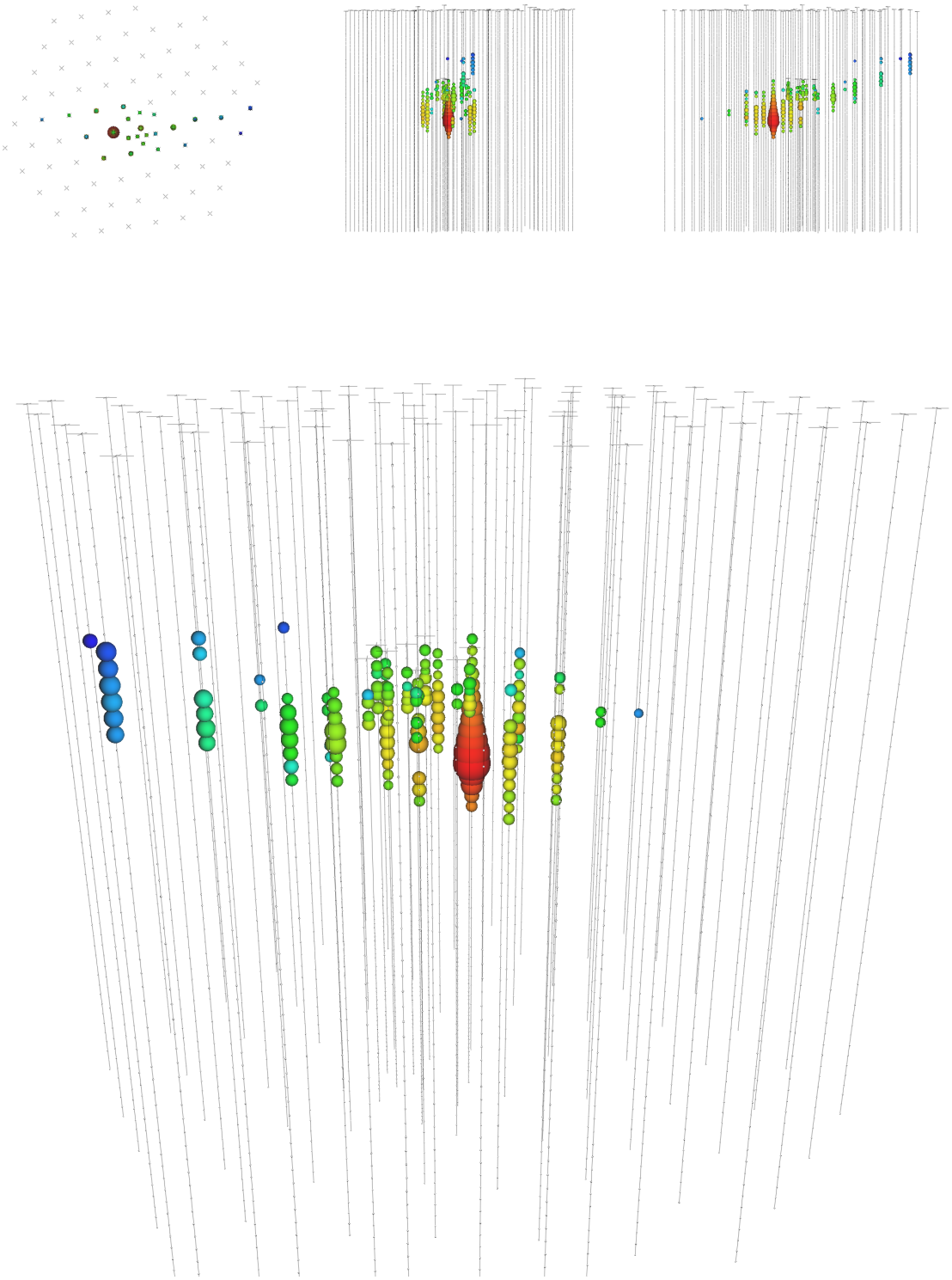

Figure 3.3: High energy starting event track in IceCube. The size of the spheres represents the amount of light deposited in the DOM and the color represents relative detection time where red means an earlier time and blue a later time.

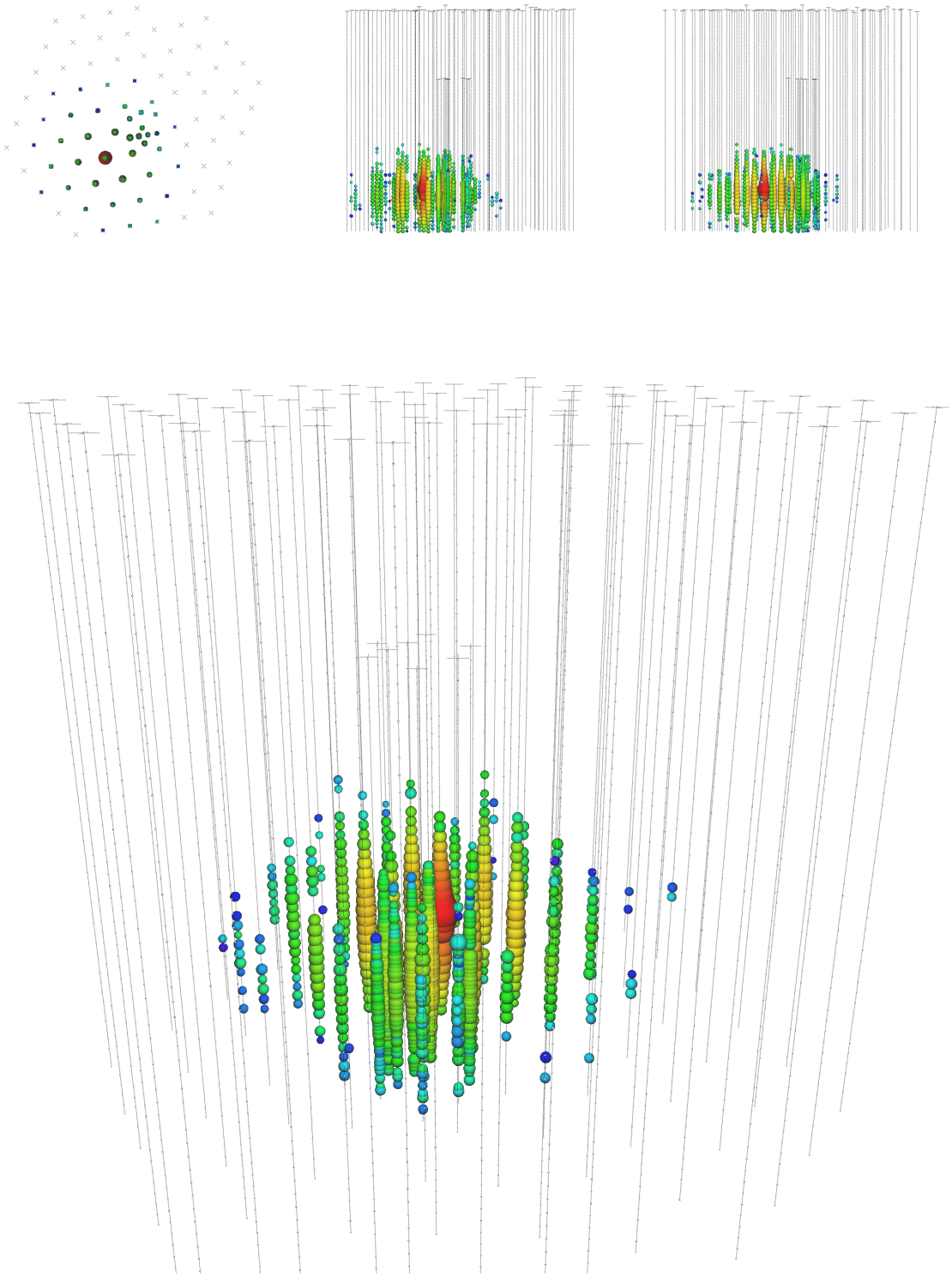

Figure 3.4: High energy starting event cascade in IceCube. The size of the spheres represents the amount of light deposited in the DOM and the color represents relative detection time where red means an earlier time and blue a later time.

to 2100 m, there is a layer of the ice that is contaminated with extra dust. This is often refereed to as the dust layer in IceCube.

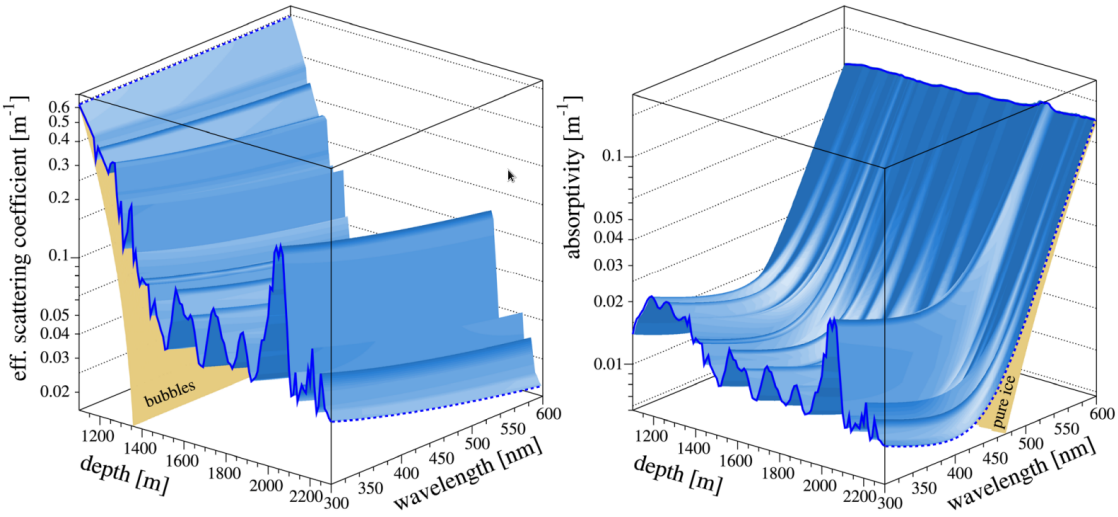

Figure 3.5: The effective scattering (left) and absorption (right) are given as a function of the wavelength and depth in the ice at the South Pole. Figure from [86]

Using the known ice measurements, reconstructions are able to simulate the structure of the ice. Various models for the ice have been proposed and simulated giving a reasonable estimate of the uncertainty associated with the ice properties. These simulations make it possible to estimate the uncertainty of the energy and direction of particles interacting in the detector.

3.4 Digital Optical Modules (DOMs)

Each DOM contains a 10" Hammamatsu photomultiplier tube (PMT), mainboard with digitizing circuits, and a flasher board for calibration. Figure 3.6 shows an illustration of an IceCube DOM. The PMTs are connected to a set of custom circuits that digitize the electrical pulses from generated by the PMTs when a photon is detected. The digitizing hardware consists of an FADC (Fast Analog to Digital Converter) and two ATWDs (Analog Transient Waveform Digitizers) that alternate use to mitigate dead time. Figure 3.7 shows a block diagram of the electronics in a DOM.

The FADCs generate a readout consisting of 256 samples. Each sample is 25 ns wide with a 10-bit resolution. This allows it to generate waveforms on the order of 6.4 μsec in

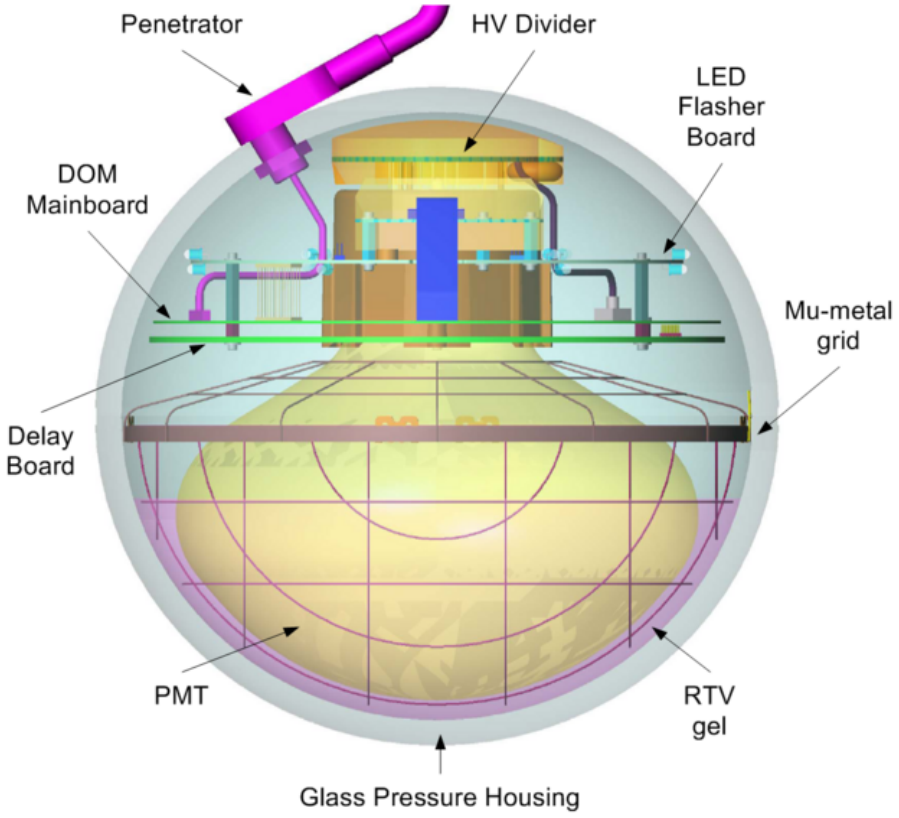

Figure 3.6: Diagram of the IceCube DOM. There are 5,160 DOMs located in the ice on 86 strings. Each DOM has a photomultiplier tube connected to a set of electronics that digitizes signals and sends collected light information to the surface.

duration. The two ATWDs are each composed of four channels. Three of the channels are used for digitizing the PMT waveform and the fourth is used for calibration signals. Each of the three digitizing channels has a different input gain corresponding to amplifications of x16, x2, and x0.25. and generates 128 samples of length 3.3 ns with a 10 bit resolution for each sample.

When the FADC receives a signal from the PMT greater than 0.25 photoelectrons, the DOM triggers and FADC and one of the ATWD digitizers start sampling the PMT output. The waveform is stored by one of the ATWDs, and a signal is sent out to the neighboring DOMs, where the neighboring DOMs are the two DOMs immediately above and below the triggering DOM. If a neighboring DOM also triggers within 1 μsec, it is referred to as a Hard Local Coincidence (HLC), and the ATWD will digitize the signal. If there is no trigger in the neighbors, it is called a Soft Local Coincidence (SLC). Signals are read out from the

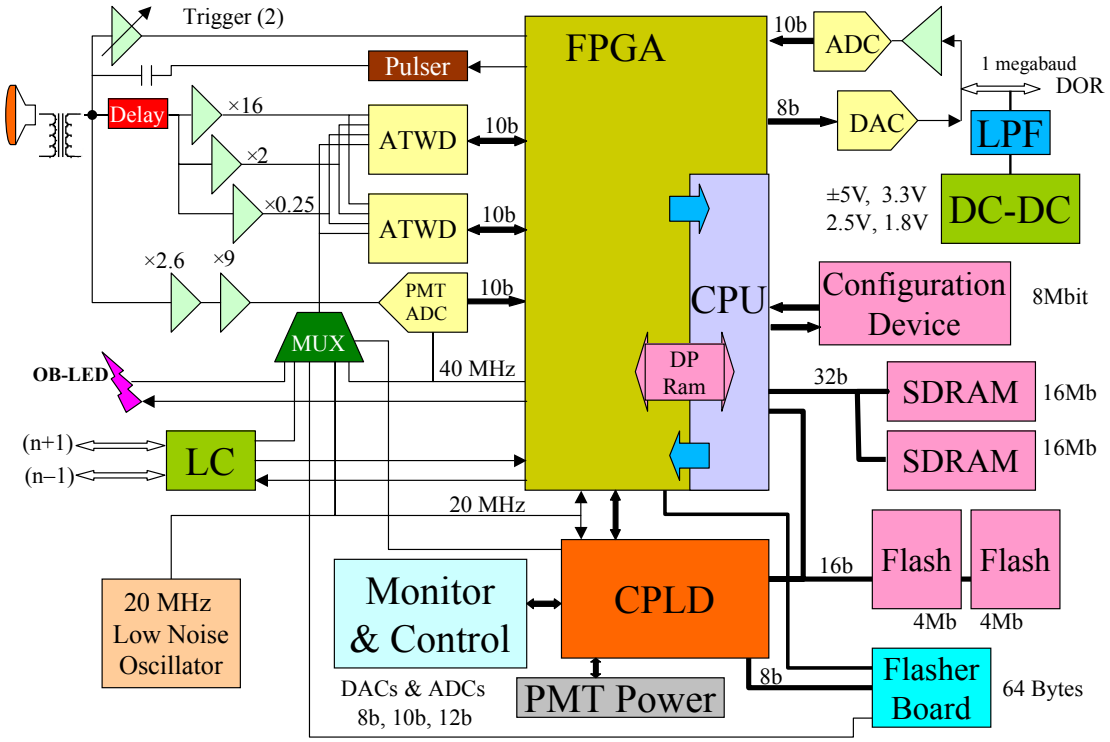

Figure 3.7: Block Diagram for an IceCube DOM

FADC and the ATWD in order of high gain to low gain, where the lower gain is not read unless the high gain is saturated. Figure 3.8 gives a diagram of the signal digitization for ATWD and FADC. Due to the time it takes the ATWD to digitize the waveform, there is a dead time of 29 μsec. If there is another trigger during this time, the waveform will be sent to the alternate ATWD for processing. The information sent to the surface is called a hit.

For HLC hits the FADC and ATWD waveforms are combined as seen in figure 3.8 and will be sent to the surface for more processing. If, however, there is no additional trigger, then only the timing information and a charge estimate from the FADC are sent to the surface.

The DOMs also contain calibration hardware consisting of a flasher circuit board with LEDs that are used to characterize the detector hardware and the ice inside the detector. Their are twelve LEDs (or flashers), with six LEDs tilted up at an angle and 6 LEDs

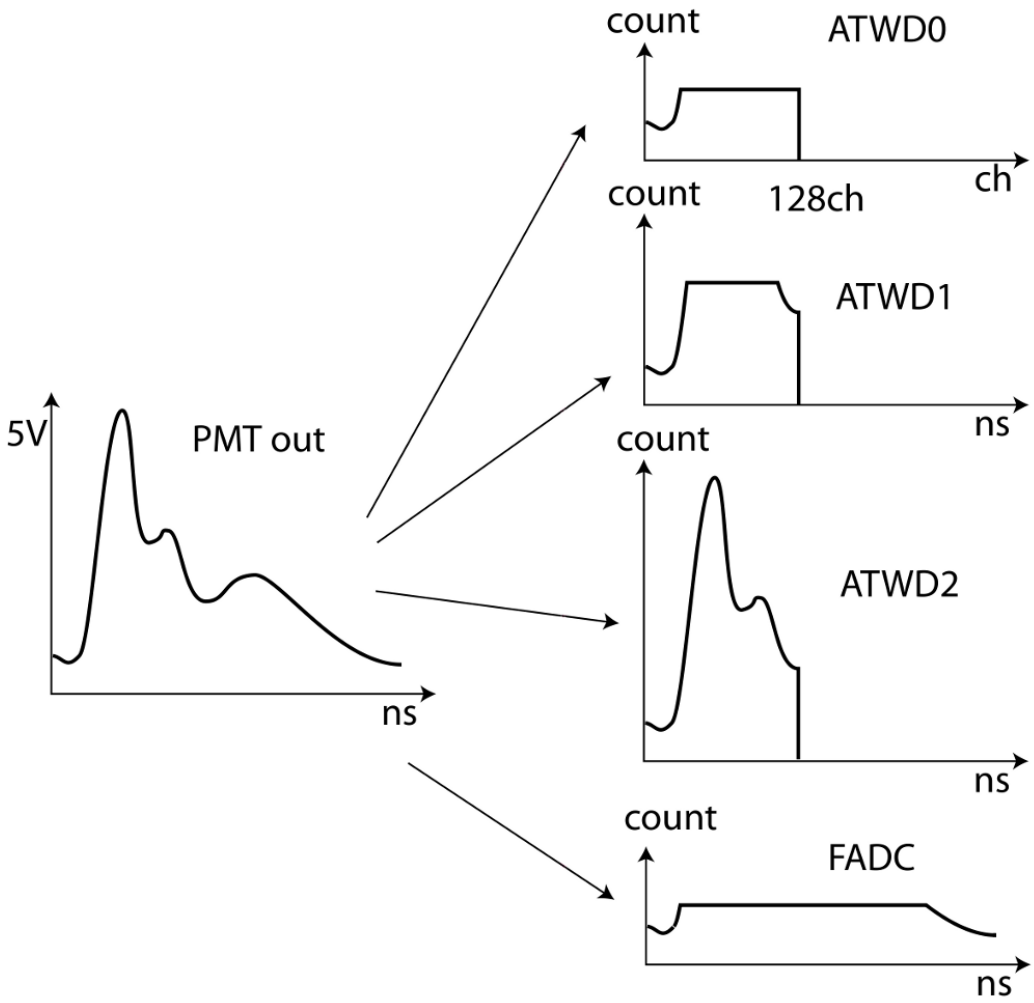

Figure 3.8: Example processing layout of the ATWD and FADC channels. The signal is read out for each of the ATWD channels from the highest gain to the lowest gain. The lower gain channels are only read if the higher gain channels become saturated. After the signal has been digitized, the digitizing waveform is sent to the surface for more processing.

horizontal. The LEDs are in pairs, one horizontal and one tilted, set 60° apart around flasher board. The wavelength of the LEDs is 405 nm to match peak sensitivity of Cherenkov photons. On a small subset of DOMs, the LEDs produce light at different wavelengths and are used to characterize the ice as a function of wavelength of the light.

A more detailed description of the DOM hardware can be found in reference [87].

3.5 Data Acquisition (DAQ)

After a DOM triggers, a hit is generated by the electronics in the DOM as described in section 3.4. Hit information is stored in a FPGA (Field Programmable Gate Array) in the

DOM until a readout is requested from the surface components. Readouts are requested at a rate of about 40 MHz by a DOMHub. Each string has a dedicated DOMHub that provides power and communication between all DOMs on a given string and the main DAQ.

The hit information is then sent to the DOMHub on the surface where trigger timing information is forwarded to the DAQ for more processing. The DAQ examines the hits from all the DOMs and creates triggers based on hit coincidences for a time window based on the type of trigger. Events are collections of hits around a trigger from the IceCube DAQ and theoretically represent particle interactions in the detector. A common trigger in IceCube is the SMT8 trigger. This requires a minimum of 8 HLC hits within a time window of 5 μsec. An SMT8 trigger event contains all hits from 4 μsec before trigger to 6 μsec after the trigger. It is possible for an event to have multiple triggers associated with it. The rate of triggers in IceCube is $\approx$3 kHz. The majority of these events are background muons that will be filtered out in later processing.

After the events have been recorded, the data pass through several filters that perform basic processing based on their associated triggers. These filters screen out events that are likely background or contain too little information to be useful. A common filter used in IceCube is the muon filter. Events that show indications that they may have been generated by muon neutrinos are processed to determine the direction of the generating neutrino. Events that do not pass through the filters are stored on tape and transported North at a later time, and events that pass the filters are sent North via satellite communication.

A more detailed description of the DAQ can be found in reference [87].

3.6 Event Reconstruction

Using the hit information from the detector, event directions and energies are reconstructed through various techniques. For cascades energy and direction can be reconstructed through a module known as monopod. The monopod reconstruction uses a likelihood function to determine the energy deposited from a cascade. The likelihood of observing an k photons from and event with energy loss E in a DOM follows a Poissonian distribution

$$\mathcal{L} = \frac{\lambda^k}{k!} e^{-\lambda}. \tag{3.1}$$

The value of λ is given by $\lambda = E\Lambda$. In this equation E is the deposited energy and Λ is the expected number of photons for 1 GeV from a simulated electromagnetic cascade, which is then scaled to match the amount of energy collected by each DOM. The log of the likelihood is then given by

$$\log \mathcal{L} = k \log(E\Lambda) - E\Lambda - \log(k!). \tag{3.2}$$

Summing over all of the DOMs and then maximizing $\mathcal{L}$ with respect to energy gives

$$0 = \frac{\partial \sum_i \log \mathcal{L}}{\partial E} \tag{3.3}$$

$$= \sum_i \left(\frac{k_i \Lambda_i}{E\Lambda_i} - \Lambda_i \right) \tag{3.4}$$

$$= \sum_i \frac{k_i}{E} - \sum_i \Lambda \tag{3.5}$$

and finally

$$E = \frac{\sum_i k_i}{\sum_i \Lambda_i}. \tag{3.6}$$

where i represents the ith DOM. This can be generalized to include PMT noise and other contributions by substituting $\lambda = E\Lambda + \rho$ where ρ is the additional photons expected from other contributions. Following the same procedure above gives

$$\log \mathcal{L} = k \log(E\Lambda + \rho) - (E\Lambda + \rho) - \log(k!) \tag{3.7}$$

and

$$\sum \Lambda_i = \sum_i \frac{k_i \Lambda_i}{(E\Lambda_i + \rho_i)} \tag{3.8}$$

which can be solved numerically for E. Equation 3.7 can also be maximized with respect to direction and location of the event as Λ is dependent on both. This will give the best fit to the direction of the cascade event.

A commonly used reconstruction is line-fit [88], which uses a similar likelihood method as described above to find a first estimate on the direction. This algorithm gives a quick estimate of the muon direction by assuming the light is a plane wave moving with the same velocity as the generating muons. A χ^2 value for the direction is generated using a likelihood function that uses a probability distribution function that takes into consideration the observation and non-observation of light in the DOMs. Line-fit has a relatively poor

directional resolution of about 5° but provides a good first estimate for later reconstructions that need an estimated starting direction.

In this analysis, energy and direction for tracks are determined by a module called millipede which breaks tracks down into small segments and applies monopod over each segment and then minimizes the result to find the best fit for the track energy and direction. There are more advanced methods to estimate the direction and energy of the observed events. Reconstructions are also dependent on the type of events observed. Each analysis in IceCube uses the methods that are the best balance between processing time, required accuracy, and the type of events being observed.

CHAPTER IV

ASTROPHYSICAL NEUTRINOS IN ICECUBE

IceCube has reported the first ever detection of very-high-energy neutrinos with an astrophysical origin. During the time period from May 31, 2010 to May 2, 2013 with a livetime of 988 days, the IceCube collaboration detected 37 astrophysical neutrino candidates with an estimated background of 8.4 ± 4.2 cosmic ray muon events and $6.6^{+5.9}_{-1.6}$ atmospheric neutrinos. The data provide a rejection of a purely atmospheric background at 5.7σ. The sources for these events have yet to be determined. A point source search was performed looking for spatial clustering of the events and clustering around known sources, but no significant correlations were observed. The events showed a weak clustering around the galactic center, but this clustering is still consistent with the background only hypothesis. The purpose of the search presented in this work is to look for correlations between the observed events and a stacked list of observed GRBs.

4.1 Event Selection

Due to the relatively large background of atmospheric muons which is on the order of 3 kHz, it can be difficult to isolate pure neutrino events interacting in IceCube. Recently, a new method was proposed that only selects events that have high energies and that appear to start inside the detector. The events are often referred to as High Energy Starting Events or HESE.

The initial selection of events includes all events that pass the filter at the South Pole (see section 3.5). In order to filter out background events, a veto is set that requires that the light from the event start inside the detector. As described in chapter 1, neutrinos are observed indirectly. Neutrinos interact with nucleons in the ice to generate charged particles that move relativistically creating Cherenkov radiation. The veto requires that the Cherenkov radiation generated by these charged particles is detected first inside some fiducial volume of the detector as seen in figure 4.1. Events that generate light in the outer

edges of the detector during the initial observation the event are classified as background. There is also an excluded region near the middle of the detector where there is more dust in the ice that could obscure the Cherenkov radiation from background muons entering the detector in that region. Events starting inside the detector are more likely to be generated by neutrinos. Atmospheric muons will begin generating Cherenkov light as soon as they enter the ice, whereas neutrinos will not generate light until they interact with nucleons in the ice creating charged particles that generate the observed Cherenkov emission.

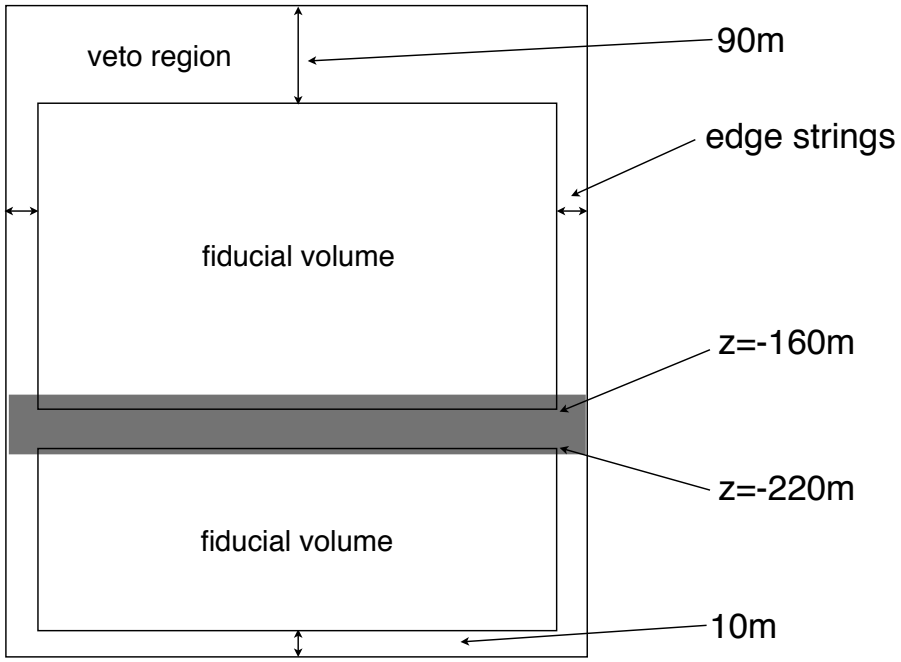

Figure 4.1: The High Energy Starting Event (HESE) containment veto is shown. Events that have early detection by DOMs in the veto region are rejected as background events.

The containment is evaluated by determining the start time of the event and excluding events that show light deposited in DOMs located in the veto region from the start time up to and including a threshold time where the start time is the time when the event first interacted inside the detector and the threshold time is the time when the light in the detector exceeds 250 cumulative PE (photoelectrons). If light with $\geq$3 HLC PE is detected in the boundary DOMs from the start time up until the threshold time, the event will be rejected as background.

Using the containment cuts described above also make it possible to use the data to

set the uncertainty on the signal event rate. Occasionally, a through-going muon may slip past the veto when the DOMs on the outer layer of the detector do not detect the light from muon. The likelihood that a muon generates light that is not seen by any given layer of the detector is independent of the layer. The event uncertainty can then be estimated by looking at events that are tagged as through-going muons by showing light in the outer layer, but do not show light in an inner layer. By counting these events the background is estimated.

The second cut is based on the deposited energy of the event. The events must deposit at least 6000 PE in the detector. This ensures that only high energy events are selected since the number of observed PEs act as a proxy for the energy of the event. Background events are more likely at lower energies as the spectrum for background events is softer than the expected spectrum from astrophysical sources. Assuming a power law distribution, background muons follow a $dN/dE = E^{-2.7}$ spectrum and atmospheric neutrinos follow an $E^{-3.7}$ spectrum while signal neutrinos would be closer to an E^{-2} spectrum. Figure 4.2 shows the rate of observed events as a function of PMT charge calibrated in PEs. Events in the shaded region are below the energy cut and are discarded. The colored and hatched regions show the expected rates for background events and the crosses are the observed data. The data represent a clear excess over the expected background and show rough agreement with an E^{-2} spectrum as indicated by the light gray line.

Events that pass the containment cut and deposit enough energy into the detector are processed further. Using the digitized PMT information for the light deposited in the detector for each event, the direction and energy of the events are estimated.

4.2 Energy and Direction Reconstructions

By examining the amount of light and the timing of the light deposited into each of the PMTs in the detector, the energy and direction were reconstructed for the HESE events. The directions and energies are reconstructed through a module called Millipede. Millipede estimates the energy of the particle by comparing the amount of light deposited by an event to a simulated reference particle. For a more complete description of Millipede see

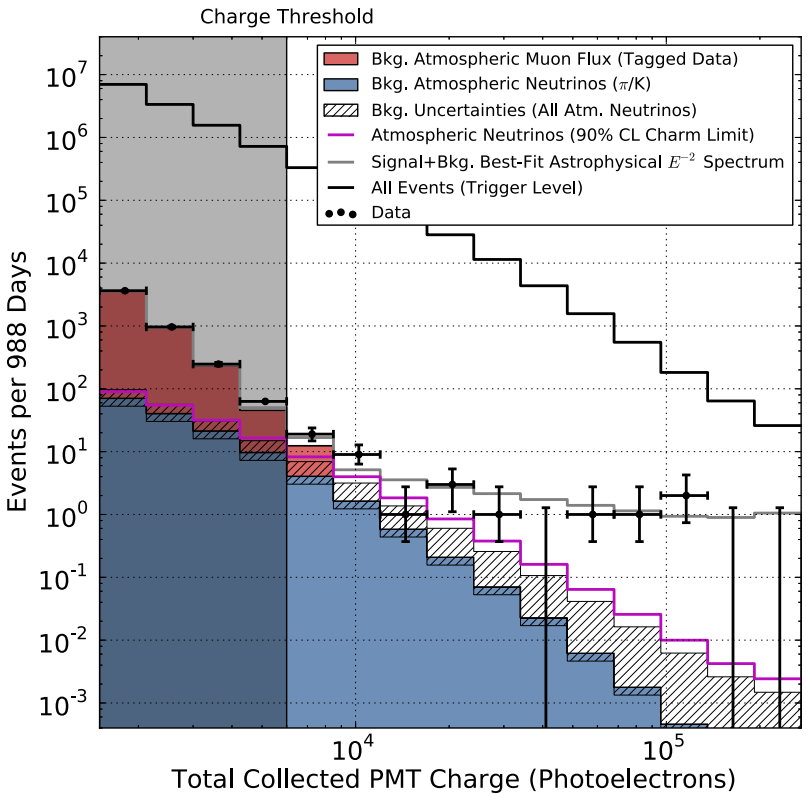

Figure 4.2: Charge Distribution

reference [89].

Energy loss by particles in ice is stochastic in nature. Particles lose energy through a variety of means including bremsstrahlung, photo-nuclear interactions, and pair production. This makes the energy estimation for track like events somewhat complicated. Millipede determines the energy of the tracks by breaking the tracks into smaller segments where each segment can represent a separate source. It then performs energy fits on each segment which are combined in a likelihood equation to find the best fit for the overall energy of the particle. Millipede applies the procedure described for monopod in section 3.6 to reconstruct the energy for each segment.

The directions of the events are found through the results of the Millipede likelihood fit across the full sky. A skymap is generated using Healpix [90] with uniform bins spread over the full 4π sr. Each bin is fed as a source direction into the Millipede likelihood which is then minimized to determine the best fit of the energies given that source direction. The value for the best fit of the likelihood is stored as a log of the likelihood. The full calculation

of the directions for the skymap of the event can take weeks due to the time required for the computation of every bin in the sky.

For cascade like events, the energy resolution is on the order of 2% and the directional uncertainty is around 15°. For track like events, the deposited energy resolution is similarly on the order of a few percent and the directional uncertainty is $< 1°$; though, this is an lower bound on the energy of originating particle. These are the statistical uncertainties and do not include any systematic uncertainty associated with the ice properties. The reported energy of the tracklike events is a lower bound on the energy as the tracks are not fully contained in the detector.

4.3 Effective Area

The effective area of the detector provides a measure of how efficiently neutrinos are detected. Theoretically, it is the equivalent area of a detector able to detect every neutrino passing through it that would observe the same number of neutrinos as the actual detector at a given energy. The effective area for the search is determined from Monte Carlo simulations. Neutrinos are simulated with an E^{-2} spectrum and then the propagation through the detector is simulated. This propagation includes the loss of energy through stochastic processes all the way through the scattering and absorption of photons in the ice. The effective area as a function of energy for this search after the energy and containment cuts is given in figure 4.3 where the effective area has been plotted for each of the neutrino flavors averaged with their antiparticle.

4.4 Event Flavor Ratios

Of the original reported 37 events two have been excluded from this search. Upon closer examination, one of these events was determined to be two muons interacting simultaneously and bypassing the veto. The other event was coincident with an IceTop event, indicating that it was likely a background muon event. These events can be excluded as this is a correlation study between a set of observed events and a list of GRBs and is not intended to measure a flux. This search specifically sets limits on the fraction of the selected events that can be attributed to a list of GRBs. Of the remaining 35 events, 7 were track like and

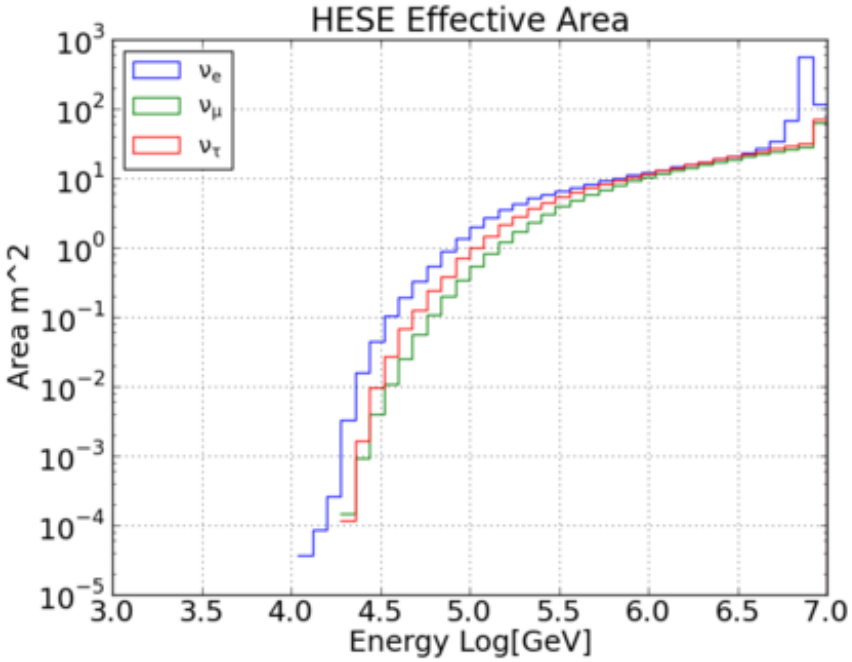

Figure 4.3: The effective area for the high energy starting event selection after the containment and energy cuts

28 were cascade like. The event information for all of the events are given in table A.1. The event ids of the omitted events are 28 and 32.

Most GRB models predict a neutrino flavor ratio at the source of $\Phi_{\nu_e}:\Phi_{\nu_\mu}:\Phi_{\nu_\tau} = 1:2:0$ (see section 2.3) which after neutrino oscillations over long distances gives an observed flavor ratio of $\Phi_{\nu_e}:\Phi_{\nu_\mu}:\Phi_{\nu_\tau} = 1:1:1$. As described in section 3.2, charged current ν_μ interactions inside IceCube will be track like and almost all others will be cascade like. For a flavor ratio of $\Phi_{\nu_e}:\Phi_{\nu_\mu}:\Phi_{\nu_\tau} = 1:1:1$, $\approx 1/3$ of the interactions should come from each flavor. Additionally, the effective area of neutral current interactions for ν_μ is roughly 1/2 the effective area of charged current interactions making 2/3 of ν_μ events track like and 1/3 cascade like. Using this information, it can be seen that the ratio of track to cascade like events is roughly 2:7 which is in rough agreement with the observed 7:28. Table 4.1 shows the distribution of cascade and track like events for N neutrinos.

The above calculations provide a back of the envelope estimation. A more thorough calculation was performed by the IceCube collaboration for a HESE search extended to lower energies in reference [91]. Simulation was used to estimate the flavor ratio for this

Table 4.1: Back of the envelope calculation for the neutrino detection channel distribution based on the flavor of the neutrino. For this study, N = 35 giving a ratio for tracks to cascades of 2:7 which is in agreement with the observed 7 tracks and 28 cascades.

Flavor	Cascades	Tracks
ν_e	$\frac{N}{3}$	0
ν_μ	$\left(\frac{1}{3}\right) \times \frac{N}{3}$	$\left(\frac{2}{3}\right) \times \frac{N}{3}$
ν_τ	$\frac{N}{3}$	0

extended set of events. As seen in figure 4.4, the observed events were consistent with a flavor ratio of $1 : 1 : 1$ with a 90% confidence level.

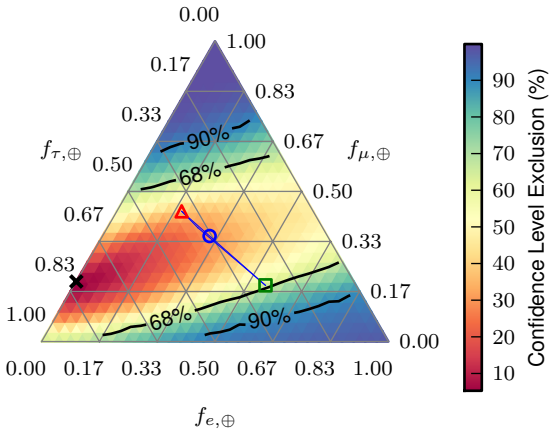

Figure 4.4: Flavor ratio scan for the low energy HESE search. The blue circle represents the best fit for the flavor ratios.

4.5 Zenith Distribution

Another interesting attribute of the observed events is the distribution as a function of declination of the events with respect to the celestial equator. Clustering in declination could have implications as to the source class of the events being observed such as galactic vs. extra galactic. The distribution of the events as a function of the sine of the declination angle are given in figure 4.5. As can be seen in the figure, there are also different types of background that dominate for different declination regions. Atmospheric muons are more prevalent above the detector in the Southern hemisphere where they are not filtered by the earth. In the Northern hemisphere, the dominate background is from atmospheric

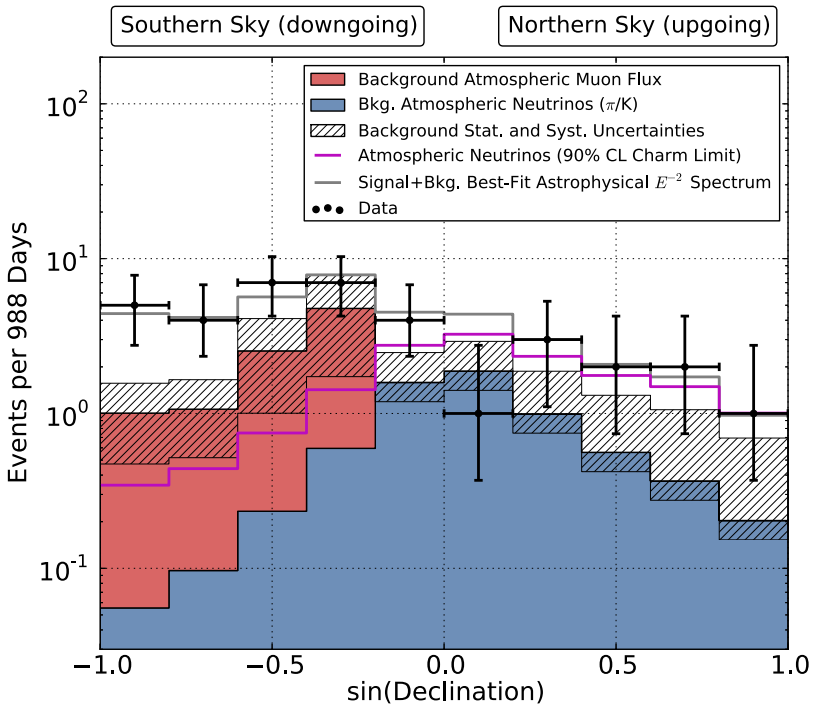

Figure 4.5: Distribution for HESE as a function of declination. The background expectation is given in the colored regions and the data shown as the crosses. The distribution of the data shows consistency with an E^{-2} spectrum.

neutrinos. The data points, indicated by the dots with crosses through them, show the declination distribution is consistent with an E^{-2} spectrum as seen from the gray line.

CHAPTER V

ANALYSIS

The search presented in this dissertation is a model independent likelihood search using a stacked list of 856 observed GRBs and 35 neutrino events in IceCube. This analysis searches for correlations between the events and GRBs in 8,976 overlapping time windows centered on the start time of the GRB extending from 10 s to 15 days before and after the burst. Each time window extends from ΔT before the start of the GRB to ΔT after giving a width for the time window of $2\Delta T$. Beginning with a value of 10 s, ΔT is increased in steps of 10 s up to one day, and between 1 day and 15 days ΔT is increased in steps of 1 hour.

5.1 GRB Selection

This search focuses on 856 reported GRBs detected by satellites. All reported GRBs from May 31, 2010 to May 2, 2013 are included in this study. The GRBs were reported via GCN and the High Energy Astrophysics Science Archive Research Center (HEASARC) database (see chapter 2). Of the 856 GRBs, $\approx$ 64% were first detected by the Gamma-ray Burst Monitor (GBM) on the *Fermi Space Telescope*, and $\approx$24% were first detected by the *Swift*/Burst Alert Telescope (BAT). After the initial detection, many of the GRBs had follow up observations which contributed additional information, specifically improved directional resolution.

This search uses the earliest reported detection time of the burst by any satellite as the GRB start time and the most accurate reported location of the burst from either the initial detection or from follow up searches for the GRB direction and localization uncertainty.

5.2 Likelihood Method

To identify correlations between the included IceCube events and GRBs, this search uses a likelihood ratio test. This method is similar to the method employed by other studies performed by IceCube [92]. A likelihood function $\mathcal{L}(n_s)$ is constructed using both temporal

and directional information for the events and GRBs. The likelihood function provides a measure of how well a signal hypothesis n_s is described by the observations. In order to characterize the signal a figure of merit or test statistic, denoted by $\hat{\lambda}$, is calculated using the likelihood equation. In order to determine $\hat{\lambda}$, λ is first defined as $\lambda = 2\log\Lambda$, where

$$\Lambda = \frac{\mathcal{L}(n_s)}{\mathcal{L}(n_s = 0)}. \tag{5.1}$$

That is, the value of Λ is the ratio of the likelihood given a signal hypothesis of n_s to the likelihood of the background only case where $n_s = 0$. A higher value of λ indicates that n_s is a better estimate for the number of signal like events whereas a lower value of λ means that the data is not well described by a signal of n_s events. In order to get the best signal hypothesis, the value of λ is maximized with respect to n_s. The value of λ at this maximized point is $\hat{\lambda}$.

5.3 Signal and Background PDFs

The likelihood function is the product of the signal PDF added to background PDF over all of the neutrino events. Both PDFs can be broken down into spatial and temporal components. The likelihood equation is given by

$$\mathcal{L}(n_s) = \prod_{e=1}^{N_E} \left[\frac{n_s}{N_E} \cdot \bar{S}_e + \left(1 - \frac{n_s}{N_E}\right) \cdot B_e \right], \tag{5.2}$$

where $\bar{S}_e$ is the signal PDF, B_e is the background PDF, n_s is a putative total number of signal events, and $N_E = 35$ is the total number of events.

The signal PDF in the likelihood equation is given by equation 5.3 where $\bar{S}_e$ is the probability that an event is signal and coincident with any one of the $\mathrm{N}_G = 856$ GRBs.

$$\bar{S}_e(\theta, \phi, t, \Delta T) = \frac{1}{N_G} \sum_g S_{e,g}(\theta, \phi, t, \Delta T) \tag{5.3}$$

The individual event-GRB PDF is $\mathrm{S}_{e,g}$ in equation 5.3 and is given by

$$S_{e,g}(\theta, \phi, t, \Delta T) = S^T_{e,g}(t, \Delta T) S^S_{e,g}(\theta, \phi) \tag{5.4}$$

where $S^T_{e,g}$ and $S^S_{e,g}$ are the temporal and spatial components of the signal PDF respectively.

The temporal component of the signal PDF is a function of the time window ΔT being examined as seen in equation 5.5 where t_e and t_g are the time of the event and GRB respectively. Any events that fall outside of the time window have a value of zero. If any event is inside the time window, it receives a normalized value of $1\text{s}/2\Delta T$.

$$S^T_{e,g}(t, \Delta T) = \begin{cases} \frac{1\text{s}}{2\Delta T} & |t_e - t_g| < \Delta T \\ 0 & |t_e - t_g| < \Delta T \end{cases} \tag{5.5}$$

The spatial component of the signal PDF $S^S_{e,t}$ is determined by the likelihood reconstruction maps. For each event a likelihood reconstruction map was generated covering the full sky. This map uses the time of arrival and number of photoelectrons in each one of IceCube's DOMs as well as those DOMs that did not record any information. The maps provide the likelihood of the direction of the event as a function of θ and ϕ, spherical coordinates in IceCube's reference frame. In other IceCube studies [75–77], the event directional uncertainty is described as a normalized Gaussian function. This is not done in this study as the likelihood maps for cascade like events can be complex and poorly represented by a Gaussian function. These per-event likelihood reconstruction maps are used to determine the signal PDF after the maps have been smoothed and normalized as described below to account for IceCube systematic uncertainty and the uncertainty of the localization of the GRBs.

The background PDF $B_{e,g}$ is given by

$$B_{e,g}(t, \theta, \phi) = B^T_{e,g}(t, \Delta T) B^S_{e,g}(\theta, \phi). \tag{5.6}$$

The temporal component of the PDF $B^T_{e,g}(t, \Delta T)$ is a constant derived by the livetime of the analysis, where the livetime is the time data was being taken for the analysis. The probability of observing a background neutrino events at any time during the analysis is uniform over the livetime of the analysis, so the probability is given as $1\text{s}/\tau$, where τ is the detector livetime. Similarly, a background event could occur at roughly any point in space relative to a GRB. There may be a weak zenith dependence on the event distribution, but the distribution of the GRBs is uniform and since the dependence is weak, the spatial background PDF can approximated as uniform where $B^S_{e,g} = 1/4\pi$ sr. The full background

PDF is then given by

$$B_e = \frac{1}{4\pi}\frac{1\text{s}}{\tau}. \tag{5.7}$$

5.3.1 Likelihood Reconstruction Maps

The likelihood reconstruction maps are Healpix maps [90] which form discrete equal area bins over the full sky. Each map contains $12{*}n_{side}^2$ bins where n_{side} is either 64 or 512 for cascades and tracks respectively. The value of the bins is a log likelihood value, which gives the likelihood that the event originated in the direction of that bin in the local IceCube coordinate system. The direction for each bin is given as the center of the bin.

Each likelihood reconstruction map must be smoothed with any directional uncertainty and then normalized to be used in the directional PDF. The smoothing processes incorporates the directional uncertainties not already accounted for into the likelihood reconstruction maps. The two sources of directional uncertainty included are the GRB positional uncertainty and the IceCube systematic uncertainty. While most satellites report GRB directions with angular resolutions far better than IceCube's angular resolution (e.g. for GRBs detected by *Swift*/BAT, the localization uncertainty is 1-4 arcminutes [93]), the localization uncertainty for *Fermi* GBM is typically 3-5° but can be as large as 15-20°. A conservative systematic uncertainty of 10.4° [94] is also included for GBM. The IceCube systematic uncertainty is primarily due to the uncertainties of the ice properties. Since most of the GRBs can have different directional uncertainties, this process must be completed for each event-GRB pair.

The smoothing kernel, equivalent to a Gaussian function on a sphere [95], smooths of an angle σ that is determined for each event-GRB combination,

$$\sigma = \sqrt{\sigma_{IC}^2 + \sigma_{GRB}^2}. \tag{5.8}$$

Here σ_{IC} is the estimated systematic uncertainty of directional reconstruction for tracks, 1° and cascades, 10°, and σ_{GRB} is the GRB localization uncertainty. The smoothed and normalized event reconstruction maps are denoted as $S_{e,g}^S(\theta, \phi)$. Figure 5.1a is a sample likelihood reconstruction map where the coloring indicates the value of the log of likelihood.

In figure 5.1b, the figure has been smoothed with an uncertainty of 10° in linear space converted back to log space.

As the likelihood reconstruction maps are in log space, each must be converted to linear space before it can be used. Each map, however, spans several orders of magnitude in log space, which makes exponentiation computationally prohibitive without special considerations. To compensate for the extreme ranges that each map is shifted and has a lower boundary or floor set for the minimum value of the map. The floor has been chosen such that it has a negligible impact on the search as any value below the floor would be too low to have a significant contribution to the likelihood.

The initial value of the map is given by $f_{start}(z)$ where z is the Healpix bin related to the direction in the sky. To set the floor, first the maximum value of the map is selected:

$$f_{max} = \max[f_{start}(z)]. \tag{5.9}$$

The floor is set before exponentiating to 1000 e-foldings below the peak value of the likelihood map.

$$f_{floor} = f_{max} - 1000 \tag{5.10}$$

Any value falling below the floor is given the value at the floor.

$$f_{floored}(z) = \begin{cases} f_{start}(z) & \text{for } f_{start} > f_{floor} \\ f_{floor} & \text{for } f_{start} \leq f_{floor} \end{cases} \tag{5.11}$$

After the floor has been set, the likelihood reconstruction map is rescaled such that the midpoint is at zero. This prevents any problems with numerical overflows during exponentiation. The values will be normalized in linear space afterwards, so this has no effect on the results.

$$f_{rescaled}(z) = f_{floored}(z) - \frac{\max[f_{floored}(z)] + \min[f_{floored}(z)]}{2} \tag{5.12}$$

The values are then exponentiated to move them from log space to linear space.

$$f_{linear}(z) = e^{(f_{rescaled}(z))} \tag{5.13}$$

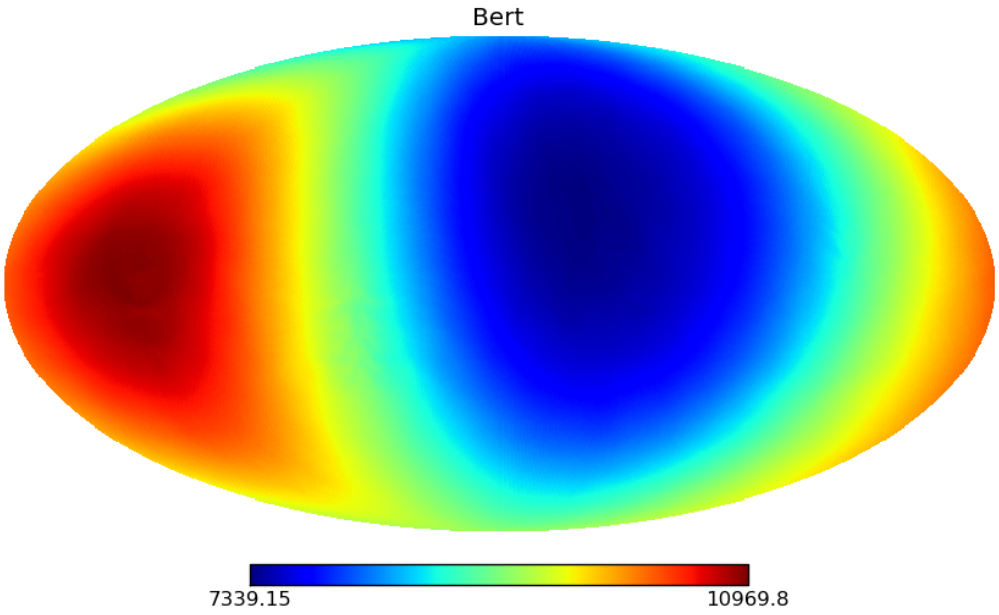

(a) Likelihood reconstruction map for a cascade event before smoothing

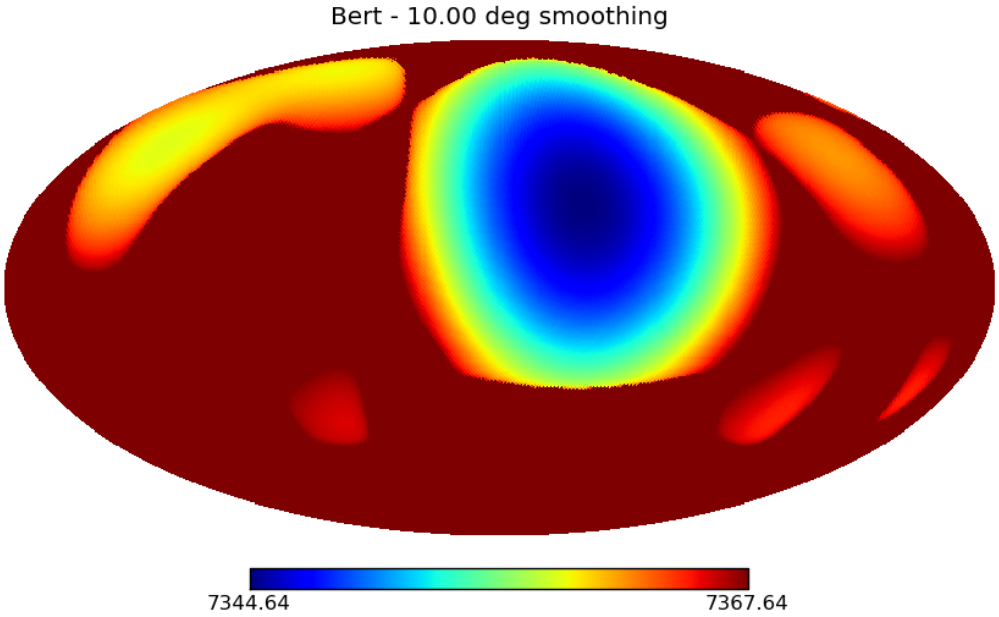

(b) Likelihood map for a cascade event after 10° smoothing

Figure 5.1: Cascade Likelihood Reconstruction Map Before and After 10° Smoothing
Likelihood reconstruction map for a cascade event before and after 10° Smoothing

Next, the map is converted from a Healpix map to a set of spherical harmonic coefficients. This step is handled by the Healpix software and gives a mapping from the function to the coefficients:

$$f_{linear}(z) \longrightarrow f_l^m, \tag{5.14}$$

where

$$f(\theta,\phi) = \sum_{l=0}^{\infty} \sum_{m=-l}^{l} f_l^m Y_l^m(\theta,\phi) \tag{5.15}$$

and

$$Y_l^m(\theta,\phi) = \sqrt{\frac{(2l+1)(l-m)!}{4\pi(l+m)!}} P_l^m(\cos(\theta)) e^{im\phi}. \tag{5.16}$$

The $P_l^m(\cos(\theta))$ are associated Legendre polynomials. All of the f_l^m are constant for each map and will not change. The values are stored for each map so this process does not have to be continually repeated.

As stated above, each event-GRB pair has a different smoothing applied due to the difference in the uncertainty of the GRB and the event type. The smoothing is done by convolving the likelihood map with a smoothing function analogous to a Gaussian with a smoothing angle given by σ. The convolution $h(\theta,\phi)$ of a function in spherical coordinates is given by

$$h(\theta,\phi) = f \circ g(\theta,\phi) = \oint \oint \sin(\theta_0) d\theta_0 d\phi_0 f(\theta,\phi) g(\theta-\theta_0, \phi-\phi_0). \tag{5.17}$$

This can be simplified by using spherical harmonics where

$$\oint \oint \sin(\theta_0) d\theta_0 d\phi_0 f(\theta,\phi) g(\theta-\theta_0, \phi-\phi_0) = \sum_{l=0}^{\infty} \sum_{m=-l}^{l} f_l^m g_l^m Y_l^m(\theta,\phi). \tag{5.18}$$

Additionally by using spherical harmonics, $h(\theta,\phi)$ can be rewritten as

$$h(\theta,\phi) = \sum_{l=0}^{\infty} \sum_{m=-l}^{l} h_l^m Y_l^m(\theta,\phi) \tag{5.19}$$

Combining equations 5.18 and 5.17 with 5.19 gives

$$\sum_{l=0}^{\infty} \sum_{m=-l}^{l} h_l^m Y_l^m(\theta,\phi) = \sum_{l=0}^{\infty} \sum_{m=-l}^{l} f_l^m g_l^m Y_l^m(\theta,\phi). \tag{5.20}$$

From equation 5.20, it can be seen that

$$h_l^m = f_l^m g_l^m \tag{5.21}$$

where f_l^m are the spherical harmonic coefficients for $f(\theta,\phi)$, g_l^m are the spherical harmonic coefficients for $g(\theta,\phi)$, and h_l^m are the spherical harmonic coefficients of $h(\theta,\phi)$ which is the convolution of $f(\theta,\phi)$ with some function $g(\theta,\phi)$.

For the purposes of this analysis, the function $g(\theta,\phi)$ is a smoothing function where the spherical harmonic coefficients are given by:

$$g_l^m = \sqrt{-l(l-1)*\sigma^2}. \tag{5.22}$$

As can be seen in equation 5.22, the coefficients decrease with increasing l. This indicates that higher order terms in h_l^m will have smaller contributions as l increases. In practice, the calculations are truncated for higher order values of l as it is obviously impossible to sum over $l \to \infty$, but as was seen above, the higher order terms contribute less and less.

The normalization is done such that for a given event e and GRB g

$$\oint\oint A_{e,g} h(\theta,\phi)\sin(\theta)d\theta d\phi = 1, \tag{5.23}$$

where $A_{e,g}$ is a normalization constant. Using the spherical harmonics from above, equation 5.23 can be rewritten as

$$\oint\oint A_{e,g}\sum_{l=0}^{\infty}\sum_{m=-l}^{l} h_l^m Y_l^m(\theta,\phi)\sin(\theta)d\theta d\phi = 1. \tag{5.24}$$

Since the spherical harmonic coefficients are independent of the angles, they can be taken outside of the integral with the normalization constant.

$$A_{e,g}\sum_{l=0}^{\infty}\sum_{m=-l}^{l} h_l^m \oint\oint Y_l^m(\theta,\phi)\sin(\theta)d\theta d\phi = 1 \tag{5.25}$$

The integral is independent of the map or smoothing and can be determined for all l and m and stored for quicker access. This value can the be rewritten as I_m^l to give

$$A_{e,g}\sum_{l=0}^{\infty}\sum_{m=-l}^{l} h_l^m I_l^m = 1 \tag{5.26}$$

where

$$I_l^m = \oint\oint Y_l^m(\theta,\phi)\sin(\theta)d\theta d\phi. \tag{5.27}$$

Equation 5.27 can then be rearranged to give the normalization constant:

$$A_{e,g} = \frac{1}{\sum_{l=0}^{\infty}\sum_{m=-l}^{l} h_l^m I_l^m}. \tag{5.28}$$

Each I_l^m is computed ahead of time to save resources and then used to calculate the normalization constant $A_{e,g}$ for each event-GRB pair. All of the normalization constants are then stored so they can be accessed quickly without having to be regenerated each time they are used.

To speed computation even further, the likelihood value is only generated for a single point rather than the entire map. In practice this is done by calculating

$$h(\theta,\phi) = A_{e,g} \sum_{l=0}^{lmax} \sum_{m=-l}^{l} f_l^m g_l^m Y_l^m(\theta,\phi) \tag{5.29}$$

where $lmax = 3 * n_{side} - 1$ and $n_{side} = 64$. The number of harmonics is obviously truncated to some finite number due to the fact that it is impossible to calculate an infinite number harmonics.

While the higher order terms that are discarded do not contribute significantly to the likelihood, the truncation does introduce some small numerical artifacts for small values of the smoothed normalized likelihood reconstruction map. To mitigate the impact of these artifacts an additional floor is set for the final function. The peak value is found by taking the maximum value of the function.

$$h_{max} = \max[h(\theta,\phi)] \tag{5.30}$$

The maximum value of $h(\theta,\phi)$ is found by looking at the location of the maximum value of $f(z)$ which will be at the same location. The location of the maximum is approximated by converting the Healpix bin z to a θ and ϕ coordinate. Only ten orders of magnitude (or 22 e-foldings) below the peak of the likelihood function are kept. Any value below this will be too low to have a significant contribution to the likelihood value. The floor is then set in linear space:

$$h_{min} = \log(h_{max}) - 22 \tag{5.31}$$

and

$$h_{floor} = e^{h_{min}}. \tag{5.32}$$

The final form of the directional PDF is given as

$$h_{final}(\theta,\phi) = \begin{cases} h(\theta,\phi) & \text{for } h(\theta,\phi) > h_{floor} \\ h_{floor} & \text{for } h(\theta,\phi) \leq h_{floor} \end{cases} \tag{5.33}$$

The value of the spatial signal PDF is given by the value of the normalized smoothed likelihood reconstruction map:

$$S^{S}_{e,g}(\theta,\phi) = h_{final}(\theta,\phi) \tag{5.34}$$

In order to simplify computation, the value of signal spatial PDF is computed by using the location of the GRB on the event smoothed normalized likelihood reconstruction map. As the maps are in local IceCube coordinates, the location of the GRB is converted to local coordinates where the value of the likelihood is read off of the map at that location.

5.4 Signal Characterization

The likelihood equation provides a measure of the number of signal like events, but the significance of these events must also be characterized since background events may appear signal-like. This analysis uses time randomized data to compare the observed data to background-like data.

5.4.1 Scramblings

In order to determine the significance of the events, the value of $\hat{\lambda}$ from observed events and GRBs is compared to the $\hat{\lambda}$ distribution from time randomized events. Randomizing the time of the event also shifts the location of events in azimuth, while preserving the zenith information from the events. In so doing, the time randomized data creates a distribution of $\hat{\lambda}$ values that are characteristic of background only events. This distribution must be generated for each of the 8,976 time windows being examined as each time window will have different $\hat{\lambda}$ since the signal PDF is a function of the time window.

Each data set where the event times have been randomized is called a scrambling and includes one full set of time windows giving 8,976 different $\hat{\lambda}$ values for the scrambling. For this search, ≈10,000 random scramblings were generated where each scrambling is generated

by randomizing the times of the 35 events over the detector livetime and taking into account, the very brief (on the order of minutes), periods when the detector was not operating.

After the distribution of $\hat{\lambda}$ has been generated for the background scramblings, the $\hat{\lambda}$ from the data is compared to the background distribution. In figure 5.2 the distribution of $\hat{\lambda}$ is shown for a time window of 10,000 s. As can be seen in the figure, higher values of $\hat{\lambda}$, which indicate more signal like characteristics, are less likely to occur randomly. This can be quantified by the use of the p-value. The p-value is probability of finding a $\hat{\lambda}$ from the scramblings that is as significant or more significant than the value of $\hat{\lambda}$ from the observed events. A lower p-value implies more significant and more signal-like data.

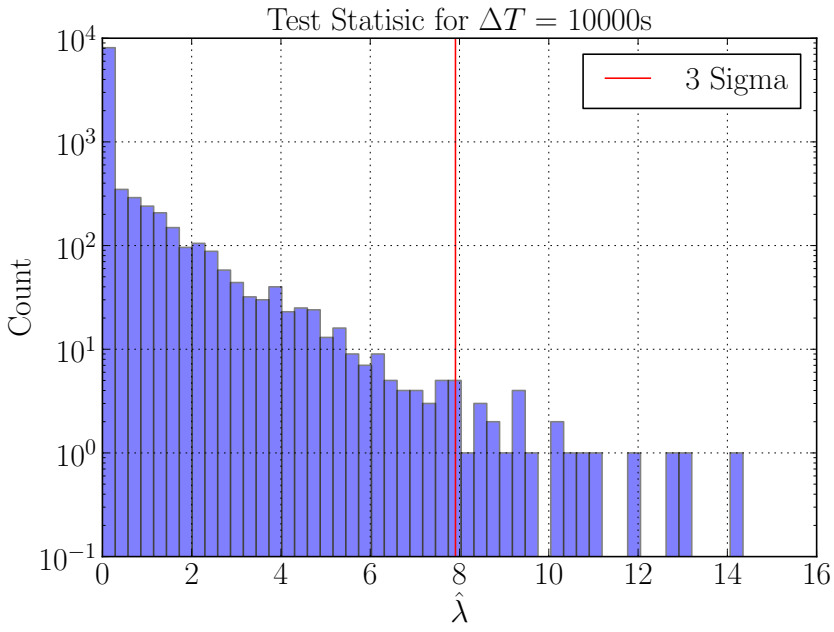

Figure 5.2: This is a sample test statistic distribution from 10,000 scramblings. The distribution is for the 10,000 s time window. Higher values of $\hat{\lambda}$ indicate more signal like events and lower values indicate less signal like events. The value where $\hat{\lambda}$ passes 3-σ is given by the red line.

As stated above, this analysis examines 8,976 different time windows. Following the procedure described to find the p-value for each time window will result in 8,976 different p-values, one for each time window. The most significant p-value from all of the time windows is called the pre-trials p-value. The pre-trials p-value provides an initial measure of the significance of the data, but does not take into the consideration the trials factor. The

trials factor is an adjustment made to the pre-trials p-value that accounts for looking into multiple time windows. For each time window examined, the significance of the observation decreases by this trials factor.

In order to determine the post-trials p-value, which is the pre-trials p-value corrected for the trials factor, a distribution of p-values is generated from the scramblings. To generate the distribution of p-values, each scramblings is processed similar to data to create a p-value for each time window based on the value of $\hat{\lambda}$ from the scrambling. This creates 8,976 new $\hat{\lambda}$ values from the scrambling which are then used to create 8,976 p-values from the $\hat{\lambda}$ distributions, one for each time window. The most significant p-value from all the time windows in the scrambling is selected. This process is repeated for all 10,000 scramblings to generate a distribution of 10,000 p-values, one from each scrambling. The p-value distribution from 10,000 scramblings is shown in figure 5.3.

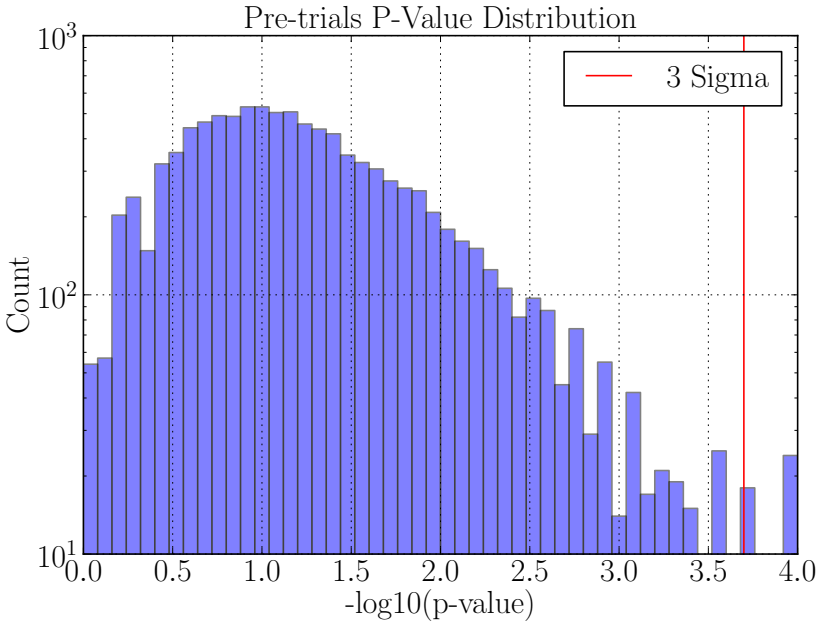

Figure 5.3: This is the distribution for the most significant p-value over all windows for 10,000 scramblings. The post-trials p-value is the probability of finding a random scrambling with a p-value as significant or more significant than the pre-trials p-value from the observed data.

After the distribution of p-values has been constructed, the post-trials p-value can be

determined. The post-trials p-value is the probability of finding a p-value from the scramblings that is as significant or more significant than the pre-trials p-value determined from the data. The post-trials p-value is found by taking the ratio of the number of pre-trials p-values as significant or more significant than the observed data to the total number of pre-trials p-values. This is equivalent to integrating to the right on the normalized plot.

5.4.2 Time Windows and Trials Factor

In this search, the time windows increase in steps of ± 10 s up to one day and then increase ± 1 hour up to 15 days. For time scales less than a day, the increase in the step size is determined by the typical observed duration of a GRB and computational requirements. GRBs generally have durations on the order of 100 s or less. The choice of 10 s gives some finer resolution on these time scales, while not increasing the number of time windows to cause excessive computation. As the windows are highly correlated, the effect on using 10 s as compared to some similar time scale such as 20 s should have very little effect on the trials-factor. After a day, the mechanisms for neutrino production are longer lived and can therefore allow for extension of the time window in steps of ± 1 hour. Similar time scales could be used however, the impact on the trials-factor will again be minimal due to the highly correlated windows.

Using the method above, an effective trials-factor can be calculated to determine the effect of looking in the multiple time windows. The maximum time window for this analysis was chosen as fifteen days. This timescale was selected as it gives an extended search window with a reasonably low expected background of less than 7 events and was still computationally favorable. This can be seen in the sensitivity plotted in figure 6.7. Additionally, the effect of examining the additional time windows on the post-trials p-value can be seen by comparing the effective trials-factor for various maximum time windows. Extending the time window also increases the number of time windows being examined and will have an effect on the trials factor. For the additional maximum time window information, the procedure above was repeated with the maximum time window set to 12 hours, 1 day, and 5 days.

For low values of the p-value, which are the ones where such consideration is warranted, an effective trials factor can be determined by comparing the pre-trials p-value to the post-trials p-value. In, this case, the effective trials-factor is the post-trials p-value divided by the pre-trials p-value. In figure 5.4a, the pre-trials p-value is plotted as a function of the post-trials p-value for the above mentioned maximum time windows and the chosen maximum time window of 15 days. Figure 5.4b explicitly shows the effective trials factor for a maximum time window of 12 hours and 15 days.

By examining figure 5.4a, it can be seen that extending the maximum time window and using more time windows does indeed have a somewhat negative effect on the post-trials p-value. The effect is highlighted in figure 5.4b where it is shown that the for the 12 hour maximum time window, the effective trials-factor is around 12 whereas a maximum time window of 15 days gives an effective trials-factor of around 20. To put this in perspective, a pre-trials p-value that corresponds to 4 σ will have a post-trials p-value corresponding to 3.367 σ for the 12 hour maximum time window and 3.223 σ for the 15 day maximum time window. During the development of this analysis, it was decided that small increase in the trials-factor was worth the ability to examine correlations between the events and GRBs up to the full 15 days.

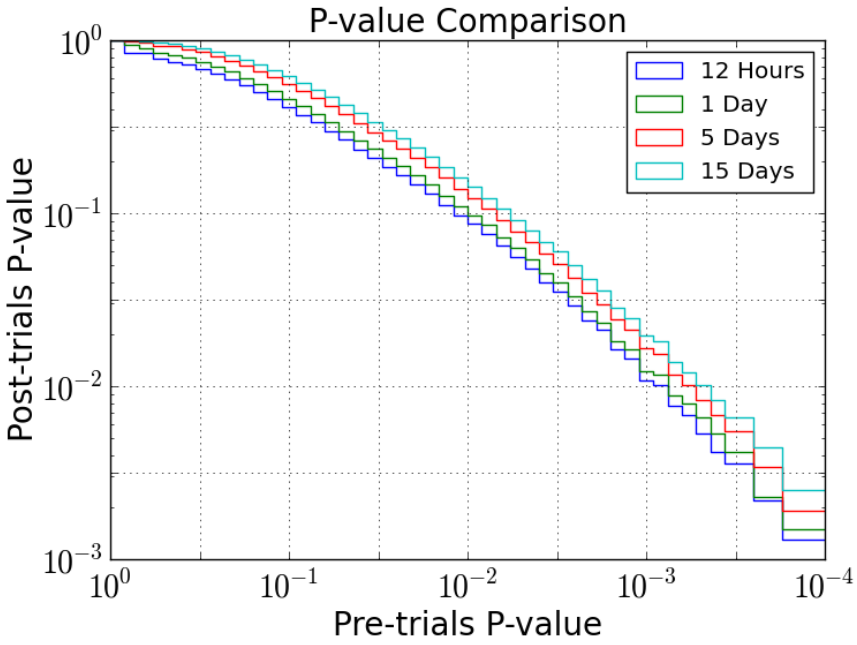

(a) Post-trials p-value as a function of pre-trials p-value for four different maximum time windows.

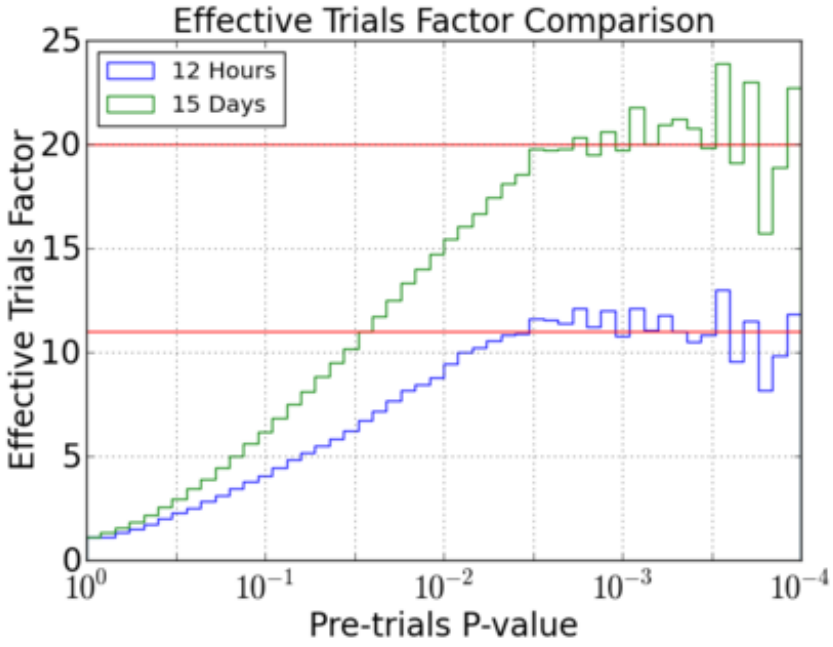

(b) The effective trials factor for the most extreme maximum time windows examined, 12 hours and 15 days.

Figure 5.4: Effective Trials-factor
The effective trials-factor is calculated to determine the effect of extending the search to 15 days before and after the GRBs. The effect on post-trials p-value can be seen to give slightly better results for a shorter maximum time window but not enough to shorten the length of the search.

CHAPTER VI

RESULTS AND DISCUSSION

The method was applied using blind techniques. In particular, the event times were kept unknown to the analyzer before the study was completed to avoid bias. The time window with the most significance is $\Delta T = 424{,}800$ s with a pre-trials p-value of 19% and a post-trials p-value of 77%. This indicates that there is not a significant correlation between the reported GRBs and the astrophysical neutrino events reported by IceCube. The lack of correlation exists over all times scales between ± 10 s and $\pm$ 15 days. The test statistic for the most significant time window (i.e. the time window with the smallest p-value) is $\hat{\lambda} = 0.622$. The maximized value of the signal for this time window is $n_s = 3.09$. Figure 6.1a shows the $\hat{\lambda}$ distribution for the this time window. The value of the observed $\hat{\lambda}$ is plotted as the dashed vertical red line. Figure 6.1b shows the p-value distribution for the scramblings. The value of the observed p-value is plotted as the dashed vertical red line.

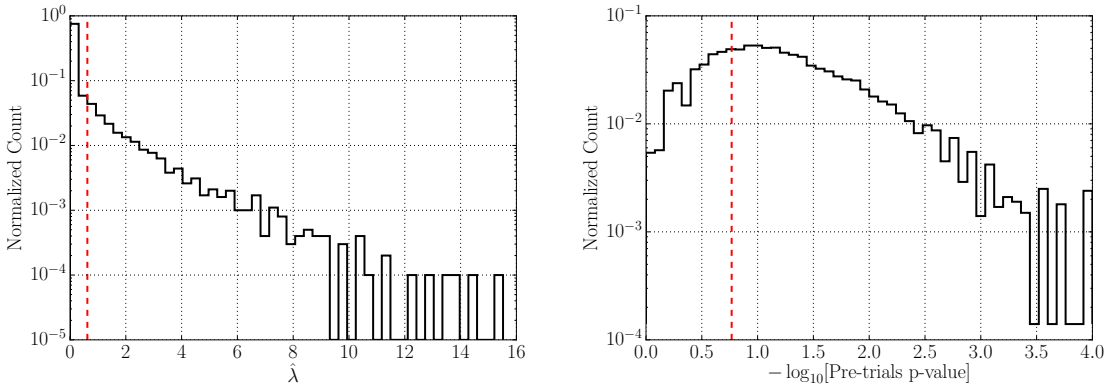

(a) Test statistic distribution

(b) P-value Distribution

Figure 6.1: Results for the test statistic and p-value distributions. On the left is the test statistic distribution for the time window with the most significant p-value with the $\hat{\lambda}$ given as the dashed vertical red line. On the right is distribution of p-values for the scramblings with the observed p-value marked with the veritable red line.

Figure 6.2 shows $\hat{n}_s$ plotted as a function of time window for the data; the dashed red

line is at the time window with the most significant $\hat{n}_s$. Similarly the p-value as a function of time window is plotted in figure 6.3 with the most significant time p-value at the dashed vertical red line.

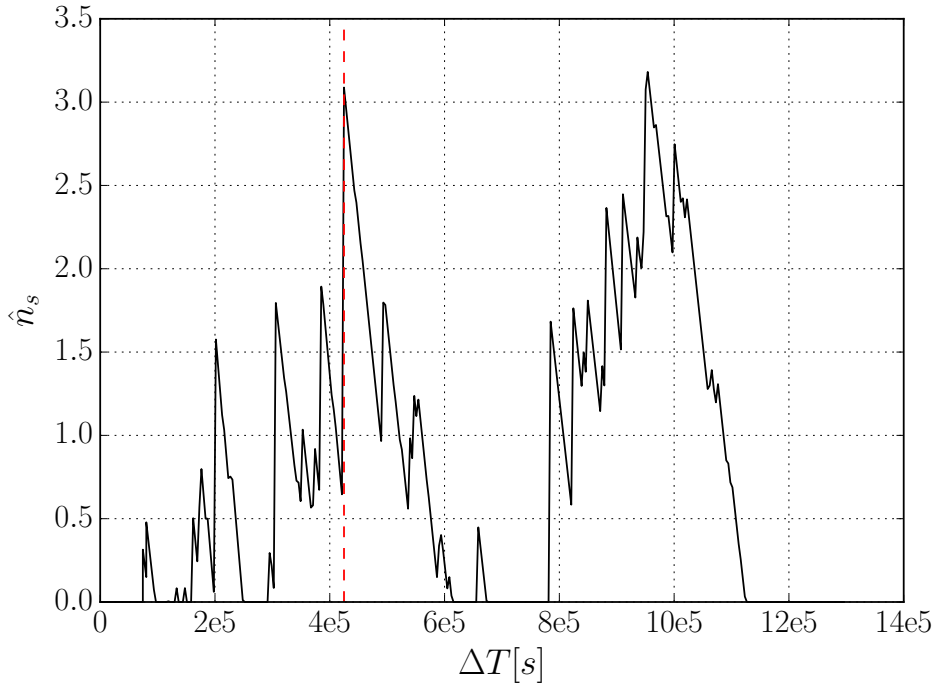

Figure 6.2: Best Fit Signal as a Function of Time Window

One event-GRB pair contributed the most to the significance. The event was track like and had a deposited energy of 31.5 TeV. The event happened 421,992 s (≈5 days) before the corresponding GRB. The location of the event was centered on RA 345.6°, Dec -24.8° with a median angular uncertainty of ≤1.3°. The peak of the event direction was 4.35° away from the GRB direction. The GRB was detected by *Fermi* GBM with trigger bn120102416 [96] and had a localization uncertainty of 11° with a duration of 20.2 s. The lightcurve for the GRB from the GBM is shown in figure 6.4. The GRB is plotted on the smoothed likelihood reconstruction map of the event in figure 6.5 with the one sigma and two sigma regions of the event shown as the dashed white and black lines respectively.

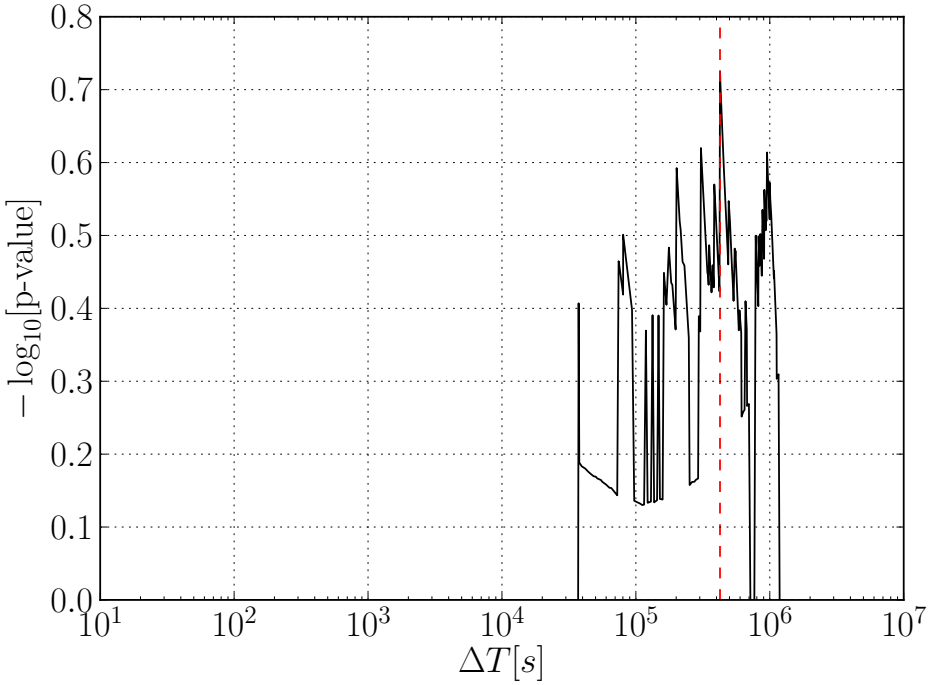

Figure 6.3: P-value as a Function of Time Window

6.1 Feldman-Cousins Confidence Belt

The method described by Feldman and Cousins in [97] is used to establish the 90% confidence level (C.L.) upper limit on the number of events correlated with known GRBs. To generate the upper limit, more scramblings are performed in which GRB times and positions are modified to simulate signal events. Signal is simulated for sets of 1 to 20 events. For each set of n simulated events, 100,000 scramblings are generated.

In order to simulate signal events, GRBs are repositioned in space and time to be coincident with a set of time randomized events. First, as with the original scramblings (see section 5.4.1), the event times are randomized over the livetime of the analysis. After the events have been randomized, a random set of n distinct events is selected, where n is the desired number of signal events. Similarly, a set of n distinct GRBs is also selected. The time of each GRB is then set to the time of one of the events. This is done to simplify computation. Since the signal PDF of the event-GRB pair is uniform over any given time window, it does not matter at which point in time the event falls relative to the GRB.

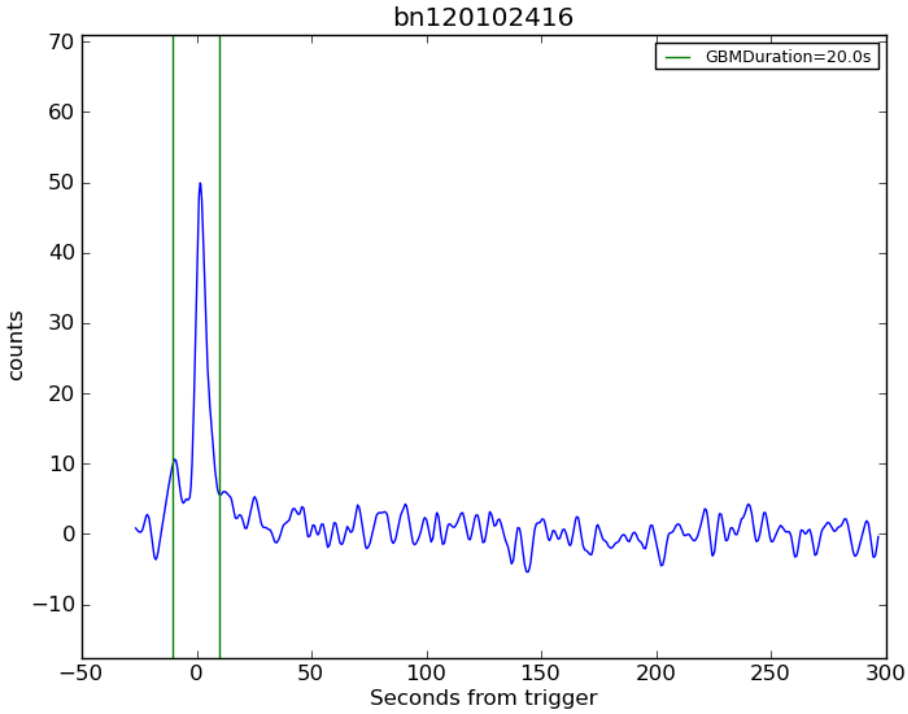

Figure 6.4: Lightcurve for the GRB with the highest contribution to the likelihood in the most significant time Window. The burst was detected by the *Fermi* GBM and had a duration of ≈22 s.

In so doing, the spatial component of the PDF can be calculated for all time windows simultaneously and the likelihood will only have to be updated for the time PDF which is a function of the time window. The GRBs are then repositioned randomly in space using a Gaussian distribution with a width σ given by

$$\sigma = \sqrt{\sigma_g^2 + \sigma_{e_{med}}^2}, \tag{6.1}$$

where σ_g is the uncertainty in the direction of the GRB and $\sigma_{e_{med}}$ is the median angular uncertainty of the event.

The Feldman Cousins confidence belt is calculated for each time window using the $\hat{\lambda}$ distributions with Poisson weighting to generate fractional events of the simulated signal. The $\hat{\lambda}$ values are binned logarthmically due to a significant number of near zero values of $\hat{\lambda}$ for low signal injection values. Since most values of the $\hat{\lambda}$ are near zero for data and the null hypothesis scramblings, this extra resolution for low values of the test statistic allows

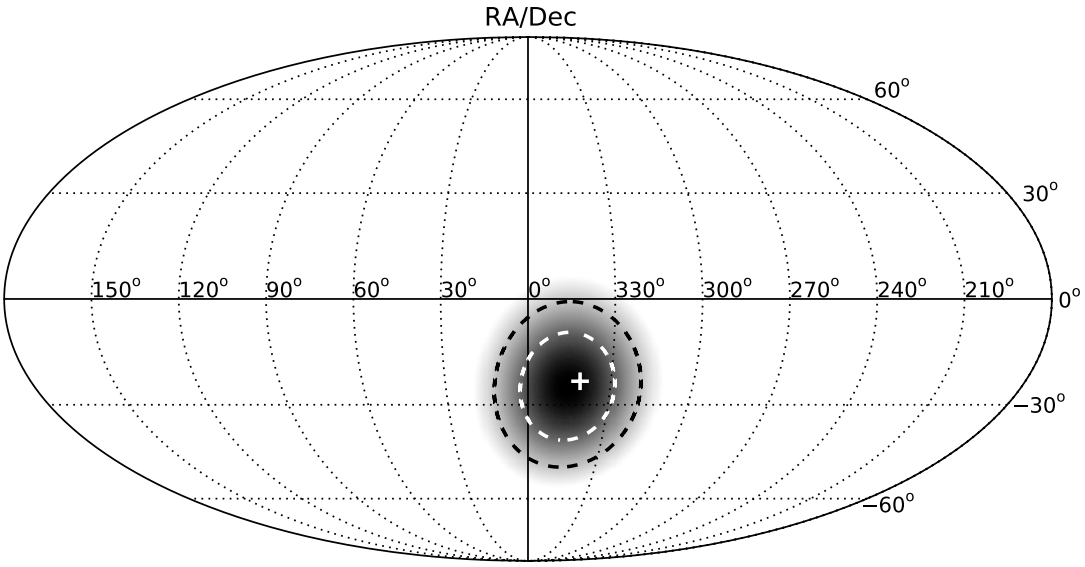

Figure 6.5: Smoothed log-likelihood map for the most significant event-GRB pair. The dashed white line represents the one sigma region, and the dashed black line represents the two sigma region where sigma is the IceCube systematic uncertainty of 1° for track like events added in quadrature with the GRB localization uncertainty of 11°. The cross marks the location of the GRB.

some finer resolution for the upper limit. A sample upper limit for $\Delta T = 100$ is given in figures 6.6a and 6.6b. In figure 6.6a, $\hat{\lambda}$ is shown up to 100, and in figure 6.6b a zoomed in version is shown with $\hat{\lambda}$ limited to smaller values near zero.

The Feldman-Cousins 90% C.L. upper limit is then determined for each time window by reading off the number events corresponding to the observed $\hat{\lambda}$ using the Feldman-Cousins upper limits generated for the given time window.

Similarly, the sensitivity for the search is the average upper limit for 10,000 random scramblings. Figure 6.7 shows the event sensitivity and the 90% C.L. upper limit as a function of time window. The upper limit is determined using the test statistic for each time window from data. The right hand side of the plot shows the percent of the astrophysical signal that can be attributed to GRBs assuming the best fit spectrum of $E^{-2.3}$.

From figure 6.7 it can be seen that the upper limit on the signal for times below 70,000 s is around 2.4 events and is at most 7.5 events for up to 15 days. Using these values, limits on the signal from spectral fits due to spectra determined from the observations of the energies of the events that could be attributed to GRBs can be determined.

Two spectral fits were examined for the observed HESE events. The signal expectations from these fits were used to generate a signal expectation based on the fitted spectra and the effective area of IceCube for the HESE search. The signal expectation is found by integrating the effective area from the simulation data (see section 4.3) folded with the desired flux. The first spectrum is a power-law with a spectral index of -2 and a best fit to the normalization of

$$E^2\phi(E) = 0.95 \pm 0.3 \times 10^{-8} \text{ GeV cm}^{-2} \text{ s}^{-1} \text{ sr}^{-1}. \tag{6.2}$$

The use of an E^{-2} power law is common due to many model predictions. An E^{-2} spectrum given the above normalization results in an all-flavor signal of 18.2 events. For correlation time scales up to ≈70,000 s, which covers most of the time scales for which neutrino emission is predicted, at most 13% of the astrophysical neutrino signal can be correlated with known GRBs. Even assuming emission correlation times as large as ±15 days, at most 41% of the astrophysical flux recently reported by IceCube, can be attributed to known GRBs.

The second spectrum examined is based on the best fit spectrum where the spectral index is allowed to vary resulting in an $E^{-2.3}$ power law given by

$$E^2\phi(E) = 1.5 \times 10^{-8}(E/100\text{TeV})^{-0.3} \text{ GeV cm}^{-2} \text{ s}^{-1} \text{ sr}^{-1} \tag{6.3}$$

which gives a signal expectation of 20.0 events. For shorter timescales around the bursts, this gives a limit of 12% of the expected signal and only 38% at around 15 days. As can be seen from the signal expectation of the two different spectra, the limits are weakly dependent on the neutrino spectral index.

6.2 Discussion

This search focuses on possible correlations between a stacked list of GRB sources and a set of observed astrophysical neutrinos in IceCube. These are the first high energy neutrino events ever observed that show an astrophysical component, and the sources of these events remains a mystery. These events show no significant spatial or temporal clustering and no significant correlation with the galactic plane and center. The events also show no correlation with a list of TeV photon sources including a catalog of 36 galactic sources and

42 extragalactic sources. The isotropic distribution of the events gives indications that the events could be extragalactic in nature and generated in the same processes that accelerate UHECRs for which GRBs have been suggested as possible sources. The determination of the sources of these neutrinos would give insight into the still unknown sources of UHECRs. In this work we show there is also no significant correlation between the 35 astrophysical neutrinos and 856 known GRBs. It was shown that the upper limit of the signal expectation on the possible correlation to these GRBs is at most 41%.

Previous searches for neutrinos generated in GRBs have focused on neutrinos that are expected to be generated during the prompt phase [76, 77, 77] and to a lesser extent the precursor phase (≈100 s before the burst) or early afterglow phase (≈1000 s after the burst) [75, 77]. The current limits constrain emission due to extended afterglow and X-ray flares as well as other unexpected mechanisms by extending the timescales of the search up to ±15 days, longer than any other searches to date. The early afterglow phase, lasting a few thousands of seconds, of the GRBs may result in the production of ≈100 PeV neutrinos through the interaction of the accelerated cosmic rays and afterglow X-ray photons [52]. Bright X-ray flares, suggested to be late activity of the central engine of the GRB [98], are often observed within a day after the prompt phase, and up to 5 days after the initial burst. These X-ray flares may have a total fluence that exceeds that of the initial burst. Neutrinos are also predicted to be produced in correlation with these X-ray flares [55].

The present result is unique in several ways. It is the first study by IceCube on GRBs that uses all neutrino flavors. Earlier GRB analysis focused on muon neutrinos that generated track like events in charged current interactions. It is also the first to study a correlation between GRBs and a known astrophysical signal. Finally, the correlation time between GRBs and neutrinos has been constrained for a very long scale: ±15 days. The results presented here scan the largest time difference between neutrinos and GRBs to date. Future models that may suggest neutrino production on longer time scales can also be constrained by this lack of neutrino observation.

Future searches will be able to extend this search to include more observed neutrino events from IceCube. This new class of astrophysical neutrinos is opening a new window

into the Universe that may help answer questions about the origin of cosmic rays. Model independent searches like this may also create new questions as unexpected neutrino observations could challenge the way scientists think about the cosmos.

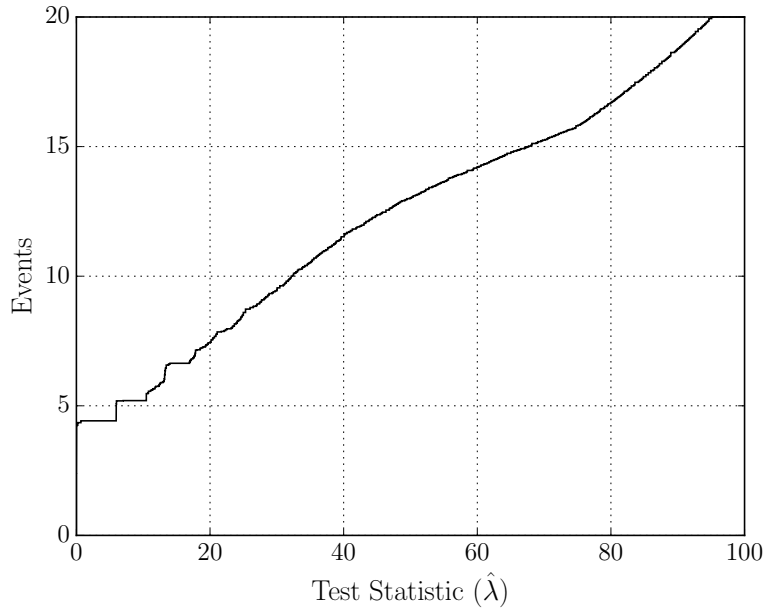

(a) Zoomed Out View

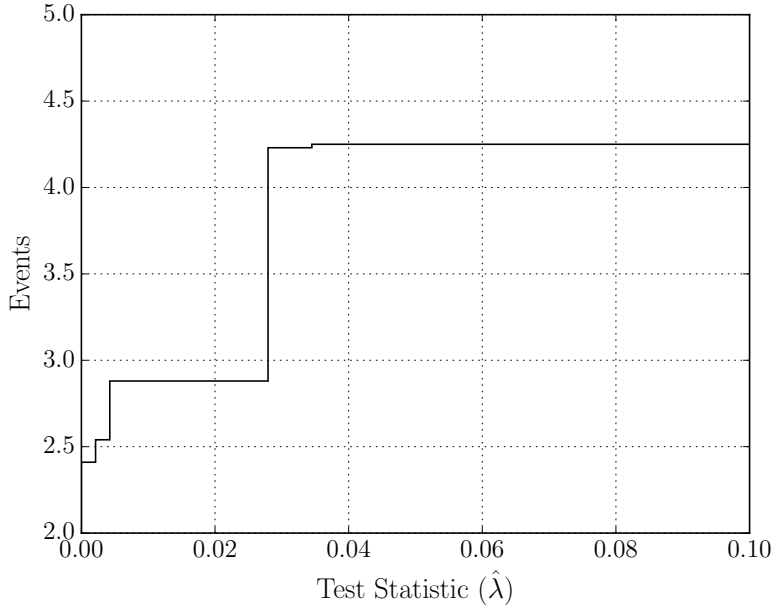

(b) Zoomed In View

Figure 6.6: Feldman Cousins upper limit for $\Delta T = 100$ s. On the top, $\hat{\lambda}$ extends from zero to 100. The figure on the bottom is zoomed in around $\hat{\lambda} = 0$ to show the structure for lower values of $\hat{\lambda}$.

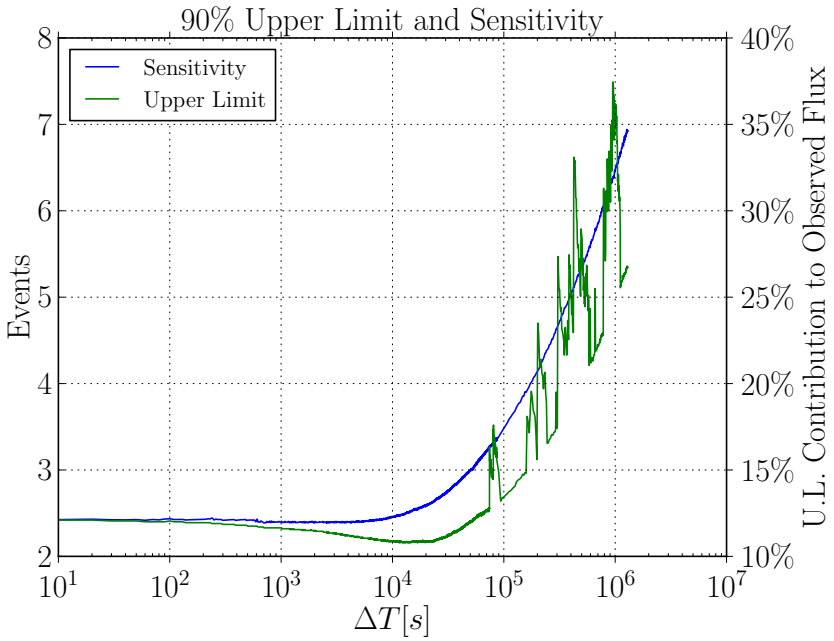

Figure 6.7: Feldman Cousins 90% C.L. sensitivity and upper limit. The left hand side of the plot shows the upper limit and sensitivity for events correlated with known GRBs. The right hand axis shows the percentage of the number of signal events that could be contributed to GRBs assuming the best fit astrophysical-neutrino spectrum of $E^{-2.3}$.

APPENDIX A

ADDITIONAL TABLES AND FIGURES

Table A.1: High Energy Starting Event Data

ID	Dep. Energy (TeV)	Observation Time (MJD)	Decl. (deg.)	R.A. (deg.)	Med. Error (deg.)	Topology
1	$47.6^{+6.5}_{-5.4}$	55351.3222143	−1.8	35.2	16.3	Shower
2	117^{+15}_{-15}	55351.4659661	−28.0	282.6	25.4	Shower
3	$78.7^{+10.8}_{-8.7}$	55451.0707482	−31.2	127.9	$\lesssim 1.4$	Track
4	165^{+20}_{-15}	55477.3930984	−51.2	169.5	7.1	Shower
5	$71.4^{+9.0}_{-9.0}$	55512.5516311	−0.4	110.6	$\lesssim 1.2$	Track
6	$28.4^{+2.7}_{-2.5}$	55567.6388127	−27.2	133.9	9.8	Shower
7	$34.3^{+3.5}_{-4.3}$	55571.2585362	−45.1	15.6	24.1	Shower
8	$32.6^{+10.3}_{-11.1}$	55608.8201315	−21.2	182.4	$\lesssim 1.3$	Track
9	$63.2^{+7.1}_{-8.0}$	55685.6629713	33.6	151.3	16.5	Shower
10	$97.2^{+10.4}_{-12.4}$	55695.2730461	−29.4	5.0	8.1	Shower
11	$88.4^{+12.5}_{-10.7}$	55714.5909345	−8.9	155.3	16.7	Shower
12	104^{+13}_{-13}	55739.4411232	−52.8	296.1	9.8	Shower
13	253^{+26}_{-22}	55756.1129844	40.3	67.9	$\lesssim 1.2$	Track
14	1041^{+132}_{-144}	55782.5161911	−27.9	265.6	13.2	Shower
15	$57.5^{+8.3}_{-7.8}$	55783.1854223	−49.7	287.3	19.7	Shower

Continued on next page

Table A.1 – continued from previous page

ID	Dep. Energy (TeV)	Observation Time (MJD)	Decl. (deg.)	R.A. (deg.)	Med. Error (deg.)	Topology
16	$30.6\,^{+3.6}_{-3.5}$	55798.6271285	−22.6	192.1	19.4	Shower
17	$200\,^{+27}_{-27}$	55800.3755483	14.5	247.4	11.6	Shower
18	$31.5\,^{+4.6}_{-3.3}$	55923.5318204	−24.8	345.6	$\lesssim 1.3$	Track
19	$71.5\,^{+7.0}_{-7.2}$	55925.7958619	−59.7	76.9	9.7	Shower
20	$1141\,^{+143}_{-133}$	55929.3986279	−67.2	38.3	10.7	Shower
21	$30.2\,^{+3.5}_{-3.3}$	55936.5416484	−24.0	9.0	20.9	Shower
22	$220\,^{+21}_{-24}$	55941.9757813	−22.1	293.7	12.1	Shower
23	$82.2\,^{+8.6}_{-8.4}$	55949.5693228	−13.2	208.7	$\lesssim 1.9$	Track
24	$30.5\,^{+3.2}_{-2.6}$	55950.8474912	−15.1	282.2	15.5	Shower
25	$33.5\,^{+4.9}_{-5.0}$	55966.7422488	−14.5	286.0	46.3	Shower
26	$210\,^{+29}_{-26}$	55979.2551750	22.7	143.4	11.8	Shower
27	$60.2\,^{+5.6}_{-5.6}$	56008.6845644	−12.6	121.7	6.6	Shower
28	$46.1\,^{+5.7}_{-4.4}$	56048.5704209	−71.5	164.8	$\lesssim 1.3$	Track
29	$32.7\,^{+3.2}_{-2.9}$	56108.2572046	41.0	298.1	7.4	Shower
30	$129\,^{+14}_{-12}$	56115.7283574	−82.7	103.2	8.0	Shower
31	$42.5\,^{+5.4}_{-5.7}$	56176.3914143	78.3	146.1	26.0	Shower

Continued on next page

Table A.1 – continued from previous page

ID	Dep. Energy (TeV)	Observation Time (MJD)	Decl. (deg.)	R.A. (deg.)	Med. Error (deg.)	Topology
32	—	56211.7401231	—	—	—	Coincident
33	$385\,^{+46}_{-49}$	56221.3424023	7.8	292.5	13.5	Shower
34	$42.1\,^{+6.5}_{-6.3}$	56228.6055226	31.3	323.4	42.7	Shower
35	$2004\,^{+236}_{-262}$	56265.1338677	−55.8	208.4	15.9	Shower
36	$28.9\,^{+3.0}_{-2.6}$	56308.1642740	−3.0	257.7	11.7	Shower
37	$30.8\,^{+3.3}_{-3.5}$	56390.1887627	20.7	167.3	$\lesssim 1.2$	Track

Table A.2: High Energy Starting Event Data

Name	Time (UTC)	RA	Dec	Err
100604A	2010-06-04 06:53:35	248.30	-73.19	11.02
100605A	2010-06-05 18:35:10	273.43	-67.60	12.92
100606A	2010-06-06 19:12:41	350.63	-66.24	0.0005
100608A	2010-06-08 09:10:07	30.54	20.45	11.69
100609A	2010-06-09 18:48:12	90.48	42.78	10.7
100612A	2010-06-12 13:04:22	63.53	13.74	10.74
100612B	2010-06-12 17:26:06	352.00	-1.83	10.52
100614A	2010-06-14 21:38:26	263.50	49.23	0.0005
100614B	2010-06-14 11:57:24	224.76	40.87	10.82
100615A	2010-06-15 01:59:03	177.20	-19.48	0.0005
100616A	2010-06-16 18:32:32	342.91	3.09	46.91
100619A	2010-06-19 00:21:07	84.62	-27.00	0.0004
100620A	2010-06-20 02:51:29	80.10	-51.68	10.5
100621A	2010-06-21 03:03:32	315.31	-51.11	0.0005
100621B	2010-06-21 10:51:19	103.83	37.35	10.77
100621C	2010-06-21 12:42:16	160.86	14.72	15.44
100625A	2010-06-25 18:32:28	15.80	-39.09	0.0005
100625B	2010-06-25 21:22:45	338.26	20.29	11.31
100628A	2010-06-28 08:16:40	225.94	-31.65	0.035
100629A	2010-06-29 19:14:04	231.21	27.81	10.92
100701B	2010-07-01 11:45:23	43.11	-2.22	0.277
100702A	2010-07-02 01:03:47	245.69	-56.55	0.0233
100703A	2010-07-03 17:43:37	9.52	-25.71	0.0467
100704A	2010-07-04 03:35:08	133.64	-24.20	0.0005
100706A	2010-07-06 16:38:19	255.16	46.89	16.05

Continued on next page

Table A.2 – continued from previous page

Name	Time (UTC)	RA	Dec	Err
100707A	2010-07-07 00:46:38	358.02	-8.66	3.365
100709A	2010-07-09 14:27:33	142.53	17.38	11.32
100713A	2010-07-13 14:36:06	255.21	28.39	0.0417
100714A	2010-07-14 16:07:24	106.37	51.14	11.04
100714B	2010-07-14 16:27:20	307.94	61.30	14.21
100715A	2010-07-15 11:27:18	299.27	-54.71	13.97
100717A	2010-07-17 08:55:06	287.06	-0.66	13.65
100717B	2010-07-17 10:41:47	304.31	19.53	13.88
100718A	2010-07-18 03:50:10	121.83	-46.18	11.97
100718B	2010-07-18 19:06:23	298.47	41.43	14.6
100719A	2010-07-19 03:30:57	112.32	-5.86	0.04
100719B	2010-07-19 07:28:18	304.87	-67.14	18.59
100719C	2010-07-19 19:48:09	231.41	18.56	14.65
100719D	2010-07-19 23:44:04	113.30	5.40	10.45
100722A	2010-07-22 02:18:37	238.80	-15.60	10.46
100722B	2010-07-22 06:58:25	31.81	56.23	13.16
100724A	2010-07-24 00:42:19	194.54	-11.10	0.0004
100724B	2010-07-24 00:42:05	120.04	76.74	1.1
100725A	2010-07-25 07:12:52	166.48	-26.67	0.0005
100725B	2010-07-25 11:24:34	290.03	76.96	0.0005
100727A	2010-07-27 05:42:17	154.18	-21.39	0.0004
100728A	2010-07-28 02:18:24	88.76	-15.25	0.0004
100728B	2010-07-28 10:31:55	44.06	0.28	0.0006
100730A	2010-07-30 11:06:15	339.79	-22.23	11.72
100802A	2010-08-02 05:45:36	2.47	47.75	0.0006

Continued on next page

Table A.2 – continued from previous page

Name	Time (UTC)	RA	Dec	Err
100804A	2010-08-04 02:29:26	248.97	27.45	10.45
100805A	2010-08-05 04:12:42	299.88	52.63	0.0005
100805B	2010-08-05 07:12:12	22.80	34.19	12.91
100805C	2010-08-05 20:16:30	112.72	-35.93	11.06
100807A	2010-08-07 09:13:13	55.30	67.67	0.0005
100810A	2010-08-10 01:10:34	124.77	-1.61	11.84
100811A	2010-08-11 02:35:49	345.87	15.86	12.03
100811B	2010-08-11 18:44:10	108.14	62.19	11.0
100814A	2010-08-14 03:50:08	22.47	-18.00	0.0004
100814B	2010-08-14 08:25:25	122.80	18.50	10.72
100816A	2010-08-16 00:37:50	351.74	26.58	0.0004
100816B	2010-08-16 00:12:42	102.12	-26.66	10.45
100819A	2010-08-19 11:56:36	279.60	-50.04	11.09
100820A	2010-08-20 08:56:58	258.79	-18.51	10.62
100823A	2010-08-23 17:25:35	20.70	5.83	0.0006
100825A	2010-08-25 06:53:49	253.44	-56.57	12.18
100826A	2010-08-26 22:58:29	279.59	-22.13	4.811
100827A	2010-08-27 10:55:49	193.90	71.89	11.85
100829A	2010-08-29 21:02:09	90.41	30.31	0.808
100829B	2010-08-29 08:59:07	115.45	-3.99	11.4
100831A	2010-08-31 15:37:26	161.26	33.65	14.54
100901A	2010-09-01 13:34:10	27.27	22.76	0.0006
100902A	2010-09-02 19:31:54	48.63	30.98	0.0004
100902B	2010-09-02 23:45:20	306.04	42.31	12.65
100904A	2010-09-04 01:33:43	172.91	-16.18	0.03

Continued on next page

Table A.2 – continued from previous page

Name	Time (UTC)	RA	Dec	Err
100905A	2010-09-05 15:08:14	31.55	14.93	0.0004
100905B	2010-09-05 21:46:23	262.65	13.08	11.14
100906A	2010-09-06 13:49:27	28.68	55.63	0.0004
100907A	2010-09-07 18:01:11	177.29	-40.63	12.48
100909A	2010-09-09 09:04:00	73.95	54.65	0.0333
100910A	2010-09-10 19:37:43	238.10	-34.62	10.45
100911A	2010-09-11 19:35:40	151.32	58.99	15.71
100915A	2010-09-15 01:31:05	315.69	65.67	0.0004
100915B	2010-09-15 05:49:40	85.39	25.09	0.0333
100916A	2010-09-16 18:41:12	152.00	-59.40	10.97
100917A	2010-09-17 05:03:25	289.25	-17.12	0.035
100918A	2010-09-18 20:42:18	308.41	-45.96	10.45
100919A	2010-09-19 21:12:17	163.24	6.02	10.56
100922A	2010-09-22 14:59:43	356.98	-25.19	18.28
100923A	2010-09-23 20:15:10	106.12	39.60	11.7
100924A	2010-09-24 03:58:08	0.67	7.00	0.0167
100925A	2010-09-25 08:05:05	254.74	-15.24	0.05
100926A	2010-09-26 14:17:04	222.75	-72.35	11.08
100926B	2010-09-26 16:39:55	43.58	-11.10	15.88
100928A	2010-09-28 02:19:52	223.04	-28.54	0.0383
100929A	2010-09-29 05:38:53	166.33	62.29	16.95
100929B	2010-09-29 07:33:04	243.62	33.33	26.0
100929C	2010-09-29 21:59:45	183.03	-24.94	12.99
101002A	2010-10-02 06:41:27	323.35	-27.47	19.39
101003A	2010-10-03 05:51:08	175.85	2.49	12.76

Continued on next page

Table A.2 – continued from previous page

Name	Time (UTC)	RA	Dec	Err
101004A	2010-10-04 10:13:50	232.22	-43.99	12.7
101008A	2010-10-08 16:43:15	328.88	37.07	0.0006
101010A	2010-10-10 04:33:47	47.19	43.56	21.34
101011A	2010-10-11 16:58:35	48.30	-65.98	0.0005
101013A	2010-10-13 09:52:43	292.08	-49.64	10.52
101014A	2010-10-14 04:11:52	26.94	-51.07	10.45
101015A	2010-10-15 13:24:03	73.16	15.46	11.98
101016A	2010-10-16 05:50:16	133.04	-4.62	10.77
101017A	2010-10-17 10:32:47	291.39	-35.15	0.0007
101017B	2010-10-17 14:51:30	27.47	-26.55	11.51
101020A	2010-10-20 23:40:41	189.61	23.13	0.0567
101021A	2010-10-21 00:13:26	0.87	-23.71	10.48
101021B	2010-10-21 01:30:32	0.46	47.34	16.5
101023A	2010-10-23 22:50:12	317.96	-65.39	0.0005
101024A	2010-10-24 11:39:34	66.51	-77.27	0.0005
101025A	2010-10-25 03:30:19	240.19	-8.49	26.48
101026A	2010-10-26 00:49:16	263.70	-0.37	12.86
101027A	2010-10-27 05:30:30	79.02	43.97	15.42
101030A	2010-10-30 15:56:31	166.38	-16.38	0.0005
101031A	2010-10-31 14:59:32	184.12	-7.47	18.97
101101A	2010-11-01 17:51:34	13.55	45.75	10.84
101101B	2010-11-01 21:34:09	266.04	-29.00	11.74
101102A	2010-11-02 20:10:08	284.68	-37.03	13.03
101104A	2010-11-04 19:26:14	161.02	-7.08	13.45
101107A	2010-11-07 00:16:26	168.33	22.43	11.18

Continued on next page

Table A.2 – continued from previous page

Name	Time (UTC)	RA	Dec	Err
101112A	2010-11-12 22:10:24	292.22	39.36	10.4
101112B	2010-11-12 23:36:56	100.10	9.62	11.6
101113A	2010-11-13 11:35:36	29.08	0.21	10.74
101114A	2010-11-14 00:32:50	303.19	14.03	0.03
101116A	2010-11-16 11:32:27	32.00	-81.20	12.68
101117A	2010-11-17 11:54:46	57.19	-26.87	10.55
101117B	2010-11-17 19:13:23	173.00	-72.66	0.0005
101119A	2010-11-19 16:27:03	226.49	59.61	19.24
101123A	2010-11-23 22:51:34	131.38	5.56	1.022
101126A	2010-11-26 04:44:28	84.77	-22.55	10.45
101127A	2010-11-27 02:13:59	290.31	7.89	25.4
101127B	2010-11-27 02:27:31	70.95	-11.32	12.29
101128A	2010-11-28 07:44:05	145.47	-35.20	11.86
101129A	2010-11-29 15:39:31	155.92	-17.64	0.05
101129B	2010-11-29 17:25:25	271.54	1.01	13.26
101130A	2010-11-30 09:39:26	61.80	-16.75	0.588
101130B	2010-11-30 01:45:55	274.61	26.62	25.8
101201A	2010-12-01 10:01:50	1.96	-16.20	0.0333
101202A	2010-12-02 03:41:54	254.02	58.48	12.07
101204A	2010-12-04 23:53:29	167.55	-20.43	0.05
101204B	2010-12-04 08:14:19	191.91	55.67	14.69
101205A	2010-12-05 07:24:25	322.10	-39.10	15.21
101206A	2010-12-06 00:52:17	164.08	-38.11	10.97
101207A	2010-12-07 12:51:42	175.75	8.72	11.05
101208A	2010-12-08 04:52:57	212.40	4.04	15.65

Continued on next page

Table A.2 – continued from previous page

Name	Time (UTC)	RA	Dec	Err
101208B	2010-12-08 11:57:01	280.94	-59.02	10.5
101211A	2010-12-11 11:37:55	31.84	10.06	15.32
101213A	2010-12-13 10:49:19	241.31	21.90	0.0005
101213B	2010-12-13 20:22:26	260.99	-64.51	12.57
101214A	2010-12-14 17:57:04	0.69	-28.27	11.79
101214B	2010-12-14 23:50:01	181.13	-31.06	11.87
101216A	2010-12-16 17:17:52	284.27	-20.97	10.61
101219A	2010-12-19 02:31:29	74.59	-2.53	0.0167
101219B	2010-12-19 16:27:53	12.23	-34.57	0.0004
101220A	2010-12-20 13:49:59	241.57	46.14	10.47
101220B	2010-12-20 20:43:54	2.70	27.20	10.5
101223A	2010-12-23 20:00:19	250.55	48.22	11.27
101224A	2010-12-24 05:27:13	285.94	45.71	0.035
101224B	2010-12-24 13:52:59	289.14	-55.25	11.46
101224C	2010-12-24 14:43:33	290.16	34.46	13.66
101224D	2010-12-24 23:57:35	325.17	-38.66	13.3
101225A	2010-12-25 18:37:45	0.20	44.60	0.0004
101225B	2010-12-25 09:02:54	60.68	32.77	10.56
101227A	2010-12-27 04:40:29	186.79	-83.55	12.63
101227B	2010-12-27 09:45:07	240.50	-24.50	10.53
101227C	2010-12-27 12:51:46	150.87	-49.44	10.72
101231A	2010-12-31 01:36:51	191.71	17.64	10.5
110101A	2011-01-01 04:50:20	264.26	36.54	15.26
110101B	2011-01-01 12:08:22	105.50	34.58	19.5
110102A	2011-01-02 18:52:25	245.88	7.61	0.0005

Continued on next page

Table A.2 – continued from previous page

Name	Time (UTC)	RA	Dec	Err
110105A	2011-01-05 21:02:40	85.11	-17.12	10.6
110106A	2011-01-06 15:25:16	79.31	64.17	0.0005
110106B	2011-01-06 21:26:16	134.15	47.00	0.0005
110107A	2011-01-07 21:15:51	299.89	41.89	0.05
110108A	2011-01-08 23:26:19	11.62	-9.64	10.74
110112A	2011-01-12 04:12:18	329.93	26.46	0.0009
110112B	2011-01-12 22:24:54	10.60	64.41	0.0433
110117A	2011-01-17 08:44:51	130.87	47.59	14.17
110117B	2011-01-17 15:01:27	129.51	-12.88	11.0
110118A	2011-01-18 20:34:19	226.57	-39.55	11.17
110119A	2011-01-19 22:20:58	348.59	5.99	0.0005
110120A	2011-01-20 15:59:39	60.48	-10.55	5.327
110123A	2011-01-23 19:17:45	247.00	28.00	10.53
110124A	2011-01-24 18:49:09	53.83	36.35	13.85
110125A	2011-01-25 21:27:28	331.35	-46.21	11.89
110128A	2011-01-28 01:44:36	193.90	28.07	0.0005
110130A	2011-01-30 05:31:53	111.51	38.25	12.4
110131A	2011-01-31 18:42:38	183.79	72.91	17.86
110201A	2011-02-01 09:35:08	137.49	88.61	0.0217
110204A	2011-02-04 04:17:12	1.82	-17.40	11.15
110205A	2011-02-05 02:02:41	164.63	67.53	0.0004
110205B	2011-02-05 00:39:04	359.73	-80.44	13.91
110205C	2011-02-05 14:07:20	312.69	-55.85	14.51
110206A	2011-02-06 18:08:05	92.36	-58.81	0.0333
110206B	2011-02-06 04:50:36	333.70	1.61	18.64

Continued on next page

Table A.2 – continued from previous page

Name	Time (UTC)	RA	Dec	Err
110207A	2011-02-07 11:17:20	12.54	-10.79	0.0217
110207B	2011-02-07 23:00:26	179.00	-58.43	13.77
110208A	2011-02-08 21:10:46	22.46	-20.59	0.0004
110209A	2011-02-09 03:58:09	329.70	-21.93	14.87
110210A	2011-02-10 09:52:41	13.06	7.78	0.0005
110212A	2011-02-12 01:09:08	69.03	43.72	0.0233
110212B	2011-02-12 13:12:34	311.33	-74.50	11.27
110213A	2011-02-13 05:17:29	42.96	49.27	0.0004
110213B	2011-02-13 14:31:48	41.77	0.95	0.5
110213C	2011-02-13 21:00:52	6.28	27.54	15.01
110217A	2011-02-17 14:10:47	274.74	32.35	13.43
110220A	2011-02-20 18:16:22	185.49	16.58	12.04
110221A	2011-02-21 05:51:20	15.18	66.05	10.47
110223A	2011-02-23 20:56:59	345.85	87.56	0.0006
110223B	2011-02-23 21:25:48	150.23	-68.30	0.0004
110226A	2011-02-26 23:44:31	199.29	35.77	12.58
110227A	2011-02-27 00:12:28	148.72	-54.04	15.83
110227B	2011-02-27 05:30:11	25.24	15.89	12.79
110227C	2011-02-27 10:04:12	232.73	-9.94	11.54
110228A	2011-02-28 00:15:59	10.27	-45.67	10.71
110228B	2011-02-28 18:59:51	245.09	16.41	11.43
110301A	2011-03-01 05:08:43	229.35	29.40	10.45
110302A	2011-03-02 01:01:52	122.35	2.91	12.45
110304A	2011-03-04 01:42:34	322.93	33.27	11.23
110305A	2011-03-05 06:38:01	260.88	-15.80	0.0005

Continued on next page

Table A.2 – continued from previous page

Name	Time (UTC)	RA	Dec	Err
110307A	2011-03-07 23:19:08	193.12	15.64	12.87
110311A	2011-03-11 19:29:22	117.59	34.29	14.21
110312A	2011-03-12 17:55:37	157.48	-5.26	0.0005
110315A	2011-03-15 23:57:04	279.19	17.54	0.0004
110316A	2011-03-16 03:19:42	46.70	-67.58	20.62
110318A	2011-03-18 13:14:19	338.29	-15.28	0.0167
110318B	2011-03-18 15:27:09	211.68	-51.58	0.0005
110319A	2011-03-19 02:16:41	356.50	-66.01	0.0005
110319B	2011-03-19 19:34:02	326.09	-56.77	0.0167
110319C	2011-03-19 15:04:46	207.96	-51.58	11.51
110319D	2011-03-19 19:34:03	325.57	-57.11	12.43
110321A	2011-03-21 08:17:43	13.31	-21.81	15.75
110322A	2011-03-22 13:23:43	99.04	-48.90	11.42
110328A	2011-03-28 12:57:45	251.21	57.58	0.0005
110328B	2011-03-28 12:29:19	117.65	43.10	10.54
110331A	2011-03-31 14:29:07	6.66	25.99	11.4
110401A	2011-04-01 22:04:19	268.56	26.87	11.07
110402A	2011-04-02 00:12:58	197.40	61.25	0.0006
110406A	2011-04-06 03:44:06	17.34	35.81	0.512
110407A	2011-04-07 14:06:41	186.03	15.71	0.0005
110407B	2011-04-07 23:56:57	97.41	-11.95	10.45
110409A	2011-04-09 04:17:21	238.70	-34.32	15.06
110410A	2011-04-10 03:10:52	30.94	-15.95	11.03
110410B	2011-04-10 18:31:19	337.17	-21.96	20.26
110411A	2011-04-11 19:34:11	291.44	67.71	0.0005

Continued on next page

Table A.2 – continued from previous page

Name	Time (UTC)	RA	Dec	Err
110411B	2011-04-11 15:05:16	210.30	-64.99	12.15
110412A	2011-04-12 07:33:35	133.49	13.49	0.0317
110413A	2011-04-13 22:31:09	352.67	32.33	15.61
110414A	2011-04-14 07:42:14	97.87	24.36	0.0004
110415A	2011-04-15 12:59:23	213.82	9.05	13.91
110420A	2011-04-20 11:02:24	2.16	-37.89	0.0004
110420B	2011-04-20 22:42:11	320.05	-41.28	0.0367
110421A	2011-04-21 18:10:40	277.23	50.80	10.54
110422A	2011-04-22 15:41:55	112.05	75.11	0.0005
110422B	2011-04-22 00:41:49	226.69	43.02	23.9
110424A	2011-04-24 18:11:36	293.31	-11.12	16.15
110426A	2011-04-26 15:06:26	219.90	-8.70	2.1
110428A	2011-04-28 09:18:30	5.30	64.80	0.15
110428B	2011-04-28 08:07:05	128.44	19.94	10.81
110430A	2011-04-30 09:00:14	147.06	67.95	10.7
110503A	2011-05-03 17:35:45	132.78	52.21	0.0005
110503B	2011-05-03 03:28:26	70.51	-10.90	11.25
110505A	2011-05-05 04:52:57	16.81	-32.30	10.85
110509A	2011-05-09 03:24:39	180.81	-34.00	11.37
110509B	2011-05-09 11:24:15	74.65	-26.98	13.31
110511A	2011-05-11 14:47:13	214.10	-45.42	14.86
110517A	2011-05-17 10:52:35	296.09	-73.76	13.73
110517B	2011-05-17 13:44:47	190.15	6.29	10.61
110518A	2011-05-18 20:38:10	67.18	-34.19	0.601
110519A	2011-05-19 02:12:16	261.64	-23.43	0.0167

Continued on next page

Table A.2 – continued from previous page

Name	Time (UTC)	RA	Dec	Err
110520A	2011-05-20 20:28:48	134.34	56.43	0.0004
110520B	2011-05-20 07:14:27	71.01	-85.93	16.19
110521A	2011-05-21 15:51:31	120.13	45.83	0.0005
110521B	2011-05-21 11:28:59	57.54	-62.34	10.48
110522A	2011-05-22 06:08:18	228.91	55.53	11.79
110522B	2011-05-22 07:06:02	184.46	49.33	12.21
110522C	2011-05-22 15:11:57	180.57	-26.81	16.26
110523A	2011-05-23 08:15:55	219.03	-15.42	11.33
110526A	2011-05-26 17:09:02	102.48	-16.42	11.93
110528A	2011-05-28 14:58:45	44.79	-6.87	10.69
110529A	2011-05-29 00:48:42	118.33	67.91	10.51
110529B	2011-05-29 06:17:41	172.60	8.79	10.61
110529C	2011-05-29 19:27:13	340.62	1.86	11.46
110530A	2011-05-30 15:31:02	282.07	61.93	0.0004
110531A	2011-05-31 10:45:11	190.51	11.85	15.18
110601A	2011-06-01 16:20:16	310.71	11.48	10.82
110604A	2011-06-04 14:49:45	271.00	18.47	0.0833
110605A	2011-06-05 04:23:32	14.95	52.46	10.45
110605B	2011-06-05 18:42:49	242.09	-3.14	14.52
110609A	2011-06-09 04:26:11	327.83	44.59	16.43
110609B	2011-06-09 10:12:06	317.63	-38.16	11.42
110610A	2011-06-10 15:22:06	308.18	74.83	0.0005
110613A	2011-06-13 15:08:47	336.86	-3.47	10.77
110616A	2011-06-16 15:33:26	274.45	-34.02	15.85
110618A	2011-06-18 08:47:37	176.81	-71.69	1.506

Continued on next page

Table A.2 – continued from previous page

Name	Time (UTC)	RA	Dec	Err
110618B	2011-06-18 18:14:17	147.05	-7.48	10.61
110622A	2011-06-22 03:47:19	133.96	19.46	10.55
110624A	2011-06-24 21:44:26	65.02	-15.95	20.22
110625A	2011-06-25 21:08:22	286.75	6.75	0.0217
110625B	2011-06-25 13:53:24	315.33	-39.44	11.37
110626A	2011-06-26 10:44:54	131.91	5.56	12.92
110629A	2011-06-29 04:09:58	69.37	25.01	11.46
110702A	2011-07-02 04:29:29	5.62	-37.66	11.43
110703A	2011-07-03 13:22:15	155.39	-29.30	11.06
110705A	2011-07-05 03:37:12	156.02	40.10	0.483
110705B	2011-07-05 08:43:44	122.96	28.80	10.85
110706A	2011-07-06 04:51:04	100.08	6.14	13.14
110706B	2011-07-06 11:26:16	94.15	-50.77	10.6
110706C	2011-07-06 17:27:57	9.06	31.73	11.18
110706D	2011-07-06 23:26:52	347.47	7.11	10.72
110708A	2011-07-08 04:43:22	340.12	53.96	0.0267
110708B	2011-07-08 13:59:46	170.38	-50.57	0.49
110709A	2011-07-09 15:24:27	238.89	40.92	0.0004
110709B	2011-07-09 21:32:44	164.65	-23.45	0.0004
110709C	2011-07-09 11:06:53	155.38	23.12	10.51
110709D	2011-07-09 20:40:50	156.21	-41.79	15.02
110710A	2011-07-10 22:53:51	229.09	48.40	11.1
110715A	2011-07-15 13:13:49	237.68	-46.24	0.0006
110716A	2011-07-16 00:25:20	329.68	-76.98	11.09
110717A	2011-07-17 04:19:50	308.47	-7.85	12.79

Continued on next page

Table A.2 – continued from previous page

Name	Time (UTC)	RA	Dec	Err
110717B	2011-07-17 07:39:56	312.84	-14.84	10.47
110719A	2011-07-19 06:09:11	24.58	34.59	0.0007
110720A	2011-07-20 04:14:32	198.65	-44.29	10.72
110721A	2011-07-21 04:47:43	332.46	-38.63	0.87
110722A	2011-07-22 16:39:17	215.06	5.00	10.59
110722B	2011-07-22 17:01:46	8.28	62.74	11.4
110725A	2011-07-25 05:39:42	270.14	-25.20	13.79
110726A	2011-07-26 01:30:40	286.72	56.07	0.0004
110726B	2011-07-26 05:04:00	317.71	2.47	11.08
110728A	2011-07-28 01:20:23	166.60	20.11	10.71
110729A	2011-07-29 03:25:06	353.39	4.97	10.49
110730A	2011-07-30 00:11:55	263.08	-22.78	11.25
110730B	2011-07-30 15:50:44	335.10	-2.89	11.07
110731A	2011-07-31 11:09:30	280.50	-28.54	0.0004
110801A	2011-08-01 19:49:42	89.44	80.96	0.0005
110801B	2011-08-01 08:01:43	248.27	-57.06	12.71
110802A	2011-08-02 15:19:16	44.46	32.59	0.349
110803A	2011-08-03 18:47:26	300.42	-11.44	12.82
110806A	2011-08-06 22:25:31	112.04	2.38	10.68
110807A	2011-08-07 19:57:46	278.70	-8.76	0.05
110808A	2011-08-08 06:18:54	57.27	-44.20	0.0009
110808B	2011-08-08 15:44:55	266.18	-37.74	0.208
110809A	2011-08-09 11:03:34	172.17	-13.93	10.56
110812A	2011-08-12 00:20:08	358.41	72.21	0.05
110812B	2011-08-12 21:35:08	77.76	1.71	10.69

Continued on next page

Table A.2 – continued from previous page

Name	Time (UTC)	RA	Dec	Err
110813A	2011-08-13 05:40:51	61.24	34.56	10.45
110815A	2011-08-15 09:40:55	85.30	32.44	0.341
110817A	2011-08-17 04:35:12	336.04	-45.84	10.51
110818A	2011-08-18 20:37:49	317.34	-63.98	0.0004
110819A	2011-08-19 15:57:54	139.49	-76.64	10.88
110820A	2011-08-20 17:38:27	343.19	70.30	0.0006
110820B	2011-08-20 21:27:48	157.58	-54.60	1.5
110820C	2011-08-20 11:25:44	90.51	21.63	11.13
110824A	2011-08-24 00:13:10	152.05	1.32	10.53
110825A	2011-08-25 02:26:50	44.90	15.40	1.031
110825B	2011-08-25 06:22:12	251.31	-80.28	11.62
110827A	2011-08-27 00:01:52	164.06	53.82	0.0367
110828A	2011-08-28 13:48:15	110.58	-23.81	10.45
110831A	2011-08-31 06:45:27	352.35	33.66	11.94
110901A	2011-09-01 05:31:44	141.28	-15.79	10.93
110903A	2011-09-03 02:39:34	197.06	58.98	0.0333
110903B	2011-09-03 00:13:06	164.21	42.08	10.47
110904A	2011-09-04 02:58:16	359.69	35.90	10.73
110904B	2011-09-04 03:54:36	190.40	-28.85	12.06
110904C	2011-09-04 12:44:20	323.74	23.94	10.53
110905A	2011-09-05 05:48:40	278.96	-19.27	0.0517
110906A	2011-09-06 12:25:13	296.89	-26.21	0.0633
110906B	2011-09-06 07:15:14	26.32	17.65	11.15
110909A	2011-09-09 02:46:59	347.34	-24.22	10.59
110911A	2011-09-11 01:41:42	258.58	-66.98	51.07

Continued on next page

Table A.2 – continued from previous page

Name	Time (UTC)	RA	Dec	Err
110915A	2011-09-15 13:20:44	310.82	-0.72	0.0004
110915B	2011-09-15 18:24:19	77.55	1.93	0.0667
110916A	2011-09-16 00:23:02	4.11	40.36	24.21
110918A	2011-09-18 21:27:02	32.58	-27.28	0.167
110919A	2011-09-19 15:12:16	279.97	66.43	10.45
110920A	2011-09-20 08:07:17	87.57	38.76	11.54
110920B	2011-09-20 13:05:44	209.82	-27.56	10.45
110921A	2011-09-21 13:51:20	294.10	36.33	0.0005
110921B	2011-09-21 10:38:48	6.09	-5.83	12.71
110923A	2011-09-23 20:01:58	323.40	-10.89	11.04
110924A	2011-09-24 09:03:20	234.75	-66.31	0.05
110926A	2011-09-26 02:33:37	69.44	10.43	10.9
110928A	2011-09-28 01:51:31	257.73	36.54	0.0006
110928B	2011-09-28 04:19:52	153.40	34.29	10.5
110929A	2011-09-29 04:28:54	288.19	-62.21	11.15
110930A	2011-09-30 13:32:32	187.31	-53.66	11.56
111001A	2011-10-01 19:17:59	340.01	-15.33	18.34
111003A	2011-10-03 11:10:00	276.80	-62.30	10.46
111005A	2011-10-05 08:05:14	223.31	-19.72	0.035
111005B	2011-10-05 09:33:04	340.30	75.80	11.66
111008A	2011-10-08 22:12:58	60.45	-32.71	0.0005
111008B	2011-10-08 23:49:02	220.75	-5.67	11.27
111009A	2011-10-09 06:45:40	183.04	-56.82	10.46
111010A	2011-10-10 15:50:22	183.54	-31.70	12.58
111010B	2011-10-10 17:00:36	69.80	41.88	10.53

Continued on next page

Table A.2 – continued from previous page

Name	Time (UTC)	RA	Dec	Err
111010C	2011-10-10 21:34:14	77.02	-14.96	12.93
111011A	2011-10-11 02:15:09	37.96	-12.53	12.41
111012A	2011-10-12 10:56:38	154.01	68.09	10.61
111012B	2011-10-12 19:27:39	97.22	67.05	10.54
111015A	2011-10-15 10:15:13	220.65	-58.41	10.58
111016A	2011-10-16 18:37:04	153.83	27.46	0.0004
111016B	2011-10-16 22:41:40	290.50	-4.58	0.541
111017A	2011-10-17 15:45:23	8.10	-7.01	10.45
111018A	2011-10-18 17:26:24	271.49	-3.91	0.0006
111018B	2011-10-18 14:16:48	106.08	66.14	12.62
111018C	2011-10-18 18:50:15	124.18	81.29	12.8
111020A	2011-10-20 06:33:49	287.05	-38.01	0.0004
111022A	2011-10-22 16:07:04	275.87	-23.67	0.0167
111022B	2011-10-22 17:13:04	108.97	49.68	0.0005
111022C	2011-10-22 20:29:24	104.50	-33.11	13.97
111024A	2011-10-24 07:21:27	222.18	25.84	0.22
111024B	2011-10-24 17:19:03	162.74	-44.94	10.71
111024C	2011-10-24 21:30:02	91.23	-1.75	16.77
111025A	2011-10-25 01:52:46	325.62	-35.52	10.75
111026A	2011-10-26 06:47:29	244.26	-47.44	0.03
111029A	2011-10-29 09:44:40	44.78	57.11	0.0007
111103A	2011-11-03 10:35:13	327.11	-10.53	0.0183
111103B	2011-11-03 10:59:03	265.69	1.61	0.0004
111103C	2011-11-03 22:45:05	201.58	-43.16	15.13
111105A	2011-11-05 10:57:36	153.48	7.28	17.63

Continued on next page

Table A.2 – continued from previous page

Name	Time (UTC)	RA	Dec	Err
111107A	2011-11-07 00:50:24	129.48	-66.52	0.0005
111107B	2011-11-07 01:49:46	315.46	-38.53	10.98
111109A	2011-11-09 02:57:46	118.20	-41.58	0.0007
111109B	2011-11-09 10:52:33	133.73	-33.35	12.75
111109C	2011-11-09 20:57:16	129.98	44.65	10.51
111112A	2011-11-12 21:47:48	223.72	28.81	11.08
111113A	2011-11-13 05:10:13	225.39	2.19	0.287
111113B	2011-11-13 09:50:12	4.32	-7.52	11.13
111114A	2011-11-14 05:35:45	268.08	-20.01	11.87
111117A	2011-11-17 12:13:41	12.70	23.02	0.0283
111117B	2011-11-17 12:38:01	27.16	-16.11	12.12
111120A	2011-11-20 13:20:24	344.60	-37.34	11.61
111121A	2011-11-21 16:26:24	154.76	-46.67	0.0005
111123A	2011-11-23 18:13:21	154.85	-20.64	0.0005
111124A	2011-11-24 07:24:10	94.06	4.63	14.03
111126A	2011-11-26 18:57:42	276.06	51.46	0.05
111127A	2011-11-27 19:27:01	103.70	3.50	10.61
111129A	2011-11-29 16:18:14	307.43	-52.71	0.0005
111201A	2011-12-01 14:22:46	190.49	32.99	0.035
111203A	2011-12-03 01:17:04	53.22	33.47	10.89
111203B	2011-12-03 14:36:46	242.83	-22.15	16.88
111204A	2011-12-04 13:37:28	336.63	-31.38	0.0006
111205A	2011-12-05 13:10:50	134.49	-31.97	0.305
111207A	2011-12-07 14:16:59	92.92	-39.00	0.05
111207B	2011-12-07 12:17:17	164.88	-17.94	14.41

Continued on next page

Table A.2 – continued from previous page

Name	Time (UTC)	RA	Dec	Err
111208A	2011-12-08 08:28:11	290.21	40.67	0.0367
111209A	2011-12-09 07:12:08	14.34	-46.80	0.0004
111210A	2011-12-10 14:37:03	191.48	-7.17	0.0006
111211A	2011-12-11 22:17:33	153.09	11.18	0.05
111212A	2011-12-12 09:23:07	310.43	-68.61	0.0004
111215A	2011-12-15 14:04:08	349.56	32.49	0.0004
111215B	2011-12-15 20:28:06	222.40	16.44	0.23
111216A	2011-12-16 09:20:31	185.99	5.83	10.49
111220A	2011-12-20 11:40:27	267.60	-56.05	10.49
111221A	2011-12-21 17:43:31	10.16	-29.77	10.58
111222A	2011-12-22 14:51:55	179.19	69.04	0.589
111225A	2011-12-25 03:50:37	13.16	51.57	0.0006
111226A	2011-12-26 19:04:59	21.50	3.87	10.45
111228A	2011-12-28 15:44:43	150.07	18.30	0.0004
111228B	2011-12-28 10:52:51	330.65	14.47	11.0
111229A	2011-12-29 22:37:52	76.29	-84.71	0.0005
111230A	2011-12-30 16:23:09	150.19	33.43	10.77
111230B	2011-12-30 19:39:32	242.61	-22.12	10.59
120101A	2012-01-01 08:30:07	185.87	52.91	13.6
120102A	2012-01-02 02:15:55	276.22	24.71	0.0005
120102B	2012-01-02 09:59:01	341.15	-23.16	11.0
120105A	2012-01-05 14:00:36	203.69	40.07	10.77
120106A	2012-01-06 14:16:24	66.11	64.04	0.0004
120107A	2012-01-07 09:12:15	246.40	-69.93	10.41
120109A	2012-01-09 19:46:02	251.33	30.80	15.38

Continued on next page

Table A.2 – continued from previous page

Name	Time (UTC)	RA	Dec	Err
120111A	2012-01-11 01:13:28	95.34	5.00	11.71
120114A	2012-01-14 16:20:06	317.90	57.04	0.0383
120114B	2012-01-14 10:23:39	263.23	-75.64	15.17
120116A	2012-01-16 18:06:28	16.24	33.93	0.0005
120118A	2012-01-18 06:04:44	195.40	-61.64	0.045
120118B	2012-01-18 17:00:21	124.87	-7.19	0.0005
120118C	2012-01-18 21:32:46	166.57	47.87	12.63
120119A	2012-01-19 04:01:34	120.03	-9.08	0.0004
120119B	2012-01-19 05:29:49	139.65	-61.33	10.59
120119C	2012-01-19 08:29:30	65.96	-33.92	11.3
120120A	2012-01-20 10:21:26	134.72	35.47	11.86
120121A	2012-01-21 09:42:19	249.35	-23.96	0.0005
120121B	2012-01-21 02:25:54	235.67	-39.34	13.04
120121C	2012-01-21 06:00:45	208.90	-1.34	10.52
120122A	2012-01-22 07:12:06	96.58	16.53	10.74
120129A	2012-01-29 13:55:46	30.44	59.28	11.478
120129B	2012-01-29 07:29:14	26.52	-8.51	18.29
120130A	2012-01-30 16:47:11	150.04	-17.45	11.04
120130B	2012-01-30 21:44:55	64.96	9.48	11.79
120130C	2012-01-30 22:30:35	323.30	58.56	10.45
120202A	2012-02-02 21:40:17	203.51	22.77	0.0417
120203A	2012-02-03 19:29:24	339.30	-46.59	12.41
120204A	2012-02-04 01:17:08	292.58	-3.57	10.45
120205A	2012-02-05 06:51:05	243.42	25.90	26.0
120206A	2012-02-06 22:46:17	73.45	58.41	10.64

Continued on next page

Table A.2 – continued from previous page

Name	Time (UTC)	RA	Dec	Err
120210A	2012-02-10 15:35:43	54.65	-58.52	11.77
120211A	2012-02-11 11:58:28	87.75	-24.77	0.0005
120212A	2012-02-12 09:11:23	43.10	-18.02	0.0005
120212B	2012-02-12 08:27:47	303.40	-48.10	12.8
120213A	2012-02-13 00:27:19	301.01	65.41	0.0005
120213B	2012-02-13 14:32:44	183.49	5.76	11.22
120215A	2012-02-15 00:41:15	30.05	8.80	0.0006
120217A	2012-02-17 19:23:51	122.44	36.77	10.89
120217B	2012-02-17 21:41:58	298.73	32.70	10.51
120218A	2012-02-18 00:49:22	319.76	-25.46	0.0317
120218B	2012-02-18 06:37:03	101.85	-1.37	11.02
120219A	2012-02-19 14:30:08	129.79	51.03	0.0004
120219B	2012-02-19 13:31:24	274.85	-31.11	15.09
120220A	2012-02-20 05:02:22	206.13	-57.36	12.76
120222A	2012-02-22 00:29:36	299.55	26.49	10.76
120222B	2012-02-22 02:51:54	340.00	-36.41	11.86
120223A	2012-02-23 22:23:49	219.61	-7.46	10.75
120224A	2012-02-24 04:39:56	40.94	-17.76	0.0005
120224B	2012-02-24 06:46:29	118.42	41.34	11.37
120224C	2012-02-24 21:33:08	331.06	10.18	11.0
120226A	2012-02-26 20:54:17	300.05	48.81	0.5
120226B	2012-02-26 10:44:16	87.59	52.35	10.46
120227A	2012-02-27 09:22:46	84.76	8.50	12.17
120227B	2012-02-27 17:24:41	256.73	-88.86	10.47
120229A	2012-02-29 14:35:11	20.03	-35.80	0.0317

Continued on next page

Table A.2 – continued from previous page

Name	Time (UTC)	RA	Dec	Err
120302A	2012-03-02 01:55:34	122.43	29.64	0.0383
120302B	2012-03-02 17:19:59	24.09	9.71	17.34
120304A	2012-03-04 01:27:48	127.15	-61.12	10.45
120304B	2012-03-04 05:57:48	277.28	-46.22	10.45
120305A	2012-03-05 19:37:30	47.54	28.49	0.0006
120308A	2012-03-08 06:13:38	219.09	79.69	0.0005
120308B	2012-03-08 14:06:06	30.75	55.22	10.47
120311A	2012-03-11 05:33:38	273.09	14.30	0.0007
120311B	2012-03-11 15:08:10	258.56	-13.05	0.0004
120312A	2012-03-12 16:06:28	251.81	23.88	0.035
120314A	2012-03-14 09:52:35	17.89	-48.73	20.63
120316A	2012-03-16 00:11:02	57.02	-56.29	1.401
120319A	2012-03-19 23:35:05	69.85	-45.44	11.03
120320A	2012-03-20 11:56:15	212.52	8.70	0.0006
120323A	2012-03-23 12:10:20	340.41	29.72	0.354
120323B	2012-03-23 03:52:49	211.10	-45.23	11.07
120324A	2012-03-24 05:59:11	291.08	24.13	0.0005
120326A	2012-03-26 01:20:29	273.91	69.26	0.0005
120327A	2012-03-27 02:55:16	246.86	-29.41	0.0004
120327B	2012-03-27 10:01:49	170.41	23.76	16.65
120328A	2012-03-28 03:06:19	241.61	-39.34	0.0005
120328B	2012-03-28 06:26:20	229.04	25.30	3.231
120331A	2012-03-31 01:19:07	26.37	-54.84	12.27
120401A	2012-04-01 05:24:15	58.08	-17.64	0.0004
120402B	2012-04-02 16:04:00	223.70	-10.40	10.72

Continued on next page

Table A.2 – continued from previous page

Name	Time (UTC)	RA	Dec	Err
120403A	2012-04-03 01:05:23	42.46	40.49	0.0383
120403B	2012-04-03 20:33:56	55.28	-89.01	0.0006
120404A	2012-04-04 12:51:02	235.01	12.88	0.0004
120410A	2012-04-10 14:02:01	159.63	-17.00	13.5
120411A	2012-04-11 22:12:26	38.07	-7.24	13.4
120412A	2012-04-12 01:18:42	29.44	-24.67	17.02
120412B	2012-04-12 22:04:41	38.91	7.06	10.77
120415A	2012-04-15 01:49:57	213.54	16.73	11.28
120415B	2012-04-15 21:23:41	190.69	4.91	12.47
120415C	2012-04-15 22:59:19	150.46	61.27	11.52
120419A	2012-04-19 12:56:25	187.40	-63.02	0.0417
120420A	2012-04-20 05:58:07	47.89	-52.19	11.74
120420B	2012-04-20 20:35:14	109.26	10.76	10.46
120422A	2012-04-22 07:12:03	136.91	14.02	0.0005
120426A	2012-04-26 02:09:14	111.54	-65.63	0.904
120426B	2012-04-26 14:02:22	285.49	-13.68	11.08
120427A	2012-04-27 01:17:28	224.94	29.31	0.658
120427B	2012-04-27 03:40:38	114.70	50.21	28.61
120429A	2012-04-29 00:04:07	165.98	-8.76	18.58
120429B	2012-04-29 11:37:04	133.04	-32.23	11.69
120430A	2012-04-30 23:30:44	47.25	18.52	11.88
120504A	2012-05-04 11:13:40	329.94	46.83	11.16
120504B	2012-05-04 22:40:08	200.28	-24.20	12.39
120506A	2012-05-06 03:05:02	172.22	-33.72	13.97
120509A	2012-05-09 14:52:03	195.39	38.31	19.76

Continued on next page

Table A.2 – continued from previous page

Name	Time (UTC)	RA	Dec	Err
120510A	2012-05-10 08:47:44	44.05	72.89	0.0013
120510B	2012-05-10 21:36:27	186.93	-55.24	11.06
120511A	2012-05-11 15:18:48	226.93	-60.49	10.6
120512A	2012-05-12 02:41:40	325.56	13.64	0.0167
120513A	2012-05-13 12:44:01	140.79	74.99	14.99
120514A	2012-05-14 01:12:49	283.00	-4.26	0.0005
120519A	2012-05-19 17:18:14	178.37	22.41	1.902
120520A	2012-05-20 22:46:25	45.86	35.28	13.31
120521A	2012-05-21 05:59:42	148.72	-49.42	0.0005
120521B	2012-05-21 09:07:48	197.01	-52.76	0.0006
120521C	2012-05-21 23:22:07	214.29	42.15	0.0006
120522A	2012-05-22 03:11:07	166.00	-62.09	0.232
120522B	2012-05-22 08:39:17	56.07	54.85	10.59
120524A	2012-05-24 03:12:55	358.15	-15.61	14.74
120526A	2012-05-26 07:16:41	66.28	-32.23	10.45
120528A	2012-05-28 10:36:00	295.13	6.50	12.0
120528B	2012-05-28 18:11:48	77.59	-37.80	0.1
120528C	2012-05-28 21:21:58	12.93	-0.95	0.1
120530A	2012-05-30 02:53:41	175.96	78.83	10.9
120531A	2012-05-31 09:26:39	290.40	1.22	15.16
120602A	2012-06-02 05:00:00	87.92	-39.35	0.117
120603A	2012-06-03 10:32:09	198.79	4.33	1.928
120604A	2012-06-04 05:16:31	163.87	-7.40	13.98
120604B	2012-06-04 08:13:40	113.58	-2.79	15.81
120605A	2012-06-05 10:52:16	243.61	41.51	10.72

Continued on next page

Table A.2 – continued from previous page

Name	Time (UTC)	RA	Dec	Err
120608A	2012-06-08 11:43:52	229.98	-26.12	10.7
120608B	2012-06-08 18:38:33	313.26	12.64	11.57
120609A	2012-06-09 13:54:35	67.32	13.00	12.85
120611A	2012-06-11 02:36:00	324.68	-44.79	11.66
120612A	2012-06-12 02:05:19	126.72	-17.57	0.0004
120612B	2012-06-12 16:19:46	211.88	34.56	12.58
120612C	2012-06-12 16:29:45	39.67	-37.91	14.89
120614A	2012-06-14 05:49:10	312.73	65.16	0.197
120616A	2012-06-16 15:06:51	79.69	56.44	13.46
120617A	2012-06-17 15:02:47	22.31	33.80	0.753
120618A	2012-06-18 03:03:50	77.31	75.85	10.72
120618B	2012-06-18 22:03:35	213.57	-2.11	11.45
120619A	2012-06-19 21:13:17	190.74	-25.02	10.77
120622A	2012-06-22 03:21:46	205.43	-1.71	0.348
120624A	2012-06-24 07:24:25	4.77	7.17	1.328
120624B	2012-06-24 22:19:30	170.89	8.93	0.0167
120625A	2012-06-25 02:50:46	51.26	51.07	10.47
120626B	2012-06-26 13:38:14	175.77	68.50	0.51
120629A	2012-06-29 13:34:12	176.16	-0.60	13.68
120630A	2012-06-30 23:17:33	352.30	42.49	0.045
120701A	2012-07-01 07:50:41	80.34	-58.53	0.0217
120701B	2012-07-01 15:41:50	182.73	-45.70	18.08
120702A	2012-07-02 21:23:20	227.80	36.76	13.42
120703A	2012-07-03 17:25:22	339.36	-29.72	0.0004
120703B	2012-07-03 10:01:13	69.49	34.74	10.72

Continued on next page

Table A.2 – continued from previous page

Name	Time (UTC)	RA	Dec	Err
120703C	2012-07-03 11:56:58	210.51	46.26	11.61
120707A	2012-07-07 19:12:17	291.87	-32.77	6.32
120709A	2012-07-09 21:11:40	318.17	-49.97	0.678
120710A	2012-07-10 02:23:19	120.39	-31.14	11.44
120711A	2012-07-11 02:44:53	94.04	-71.09	0.12
120711B	2012-07-11 03:11:02	331.71	60.00	0.0533
120711C	2012-07-11 10:42:55	127.88	-31.83	15.6
120712A	2012-07-12 13:42:25	169.59	-20.03	0.0004
120713A	2012-07-13 05:25:30	161.68	40.66	19.68
120714A	2012-07-14 07:46:46	167.98	-30.63	0.0005
120714B	2012-07-14 21:18:46	355.41	-46.20	0.0433
120715A	2012-07-15 01:35:17	272.15	58.79	11.05
120716A	2012-07-16 17:05:05	313.09	9.56	0.524
120716B	2012-07-16 13:51:04	304.53	59.41	11.58
120719A	2012-07-19 03:30:02	204.29	-43.45	10.49
120722A	2012-07-22 12:53:26	230.50	13.25	0.0006
120724A	2012-07-24 06:39:02	245.18	3.51	0.0004
120727A	2012-07-27 08:29:40	163.26	25.09	18.48
120727B	2012-07-27 16:20:20	37.76	16.36	10.45
120728A	2012-07-28 22:25:11	137.09	-54.44	0.0005
120728B	2012-07-28 10:25:24	103.77	-45.89	1.417
120729A	2012-07-29 10:56:12	13.07	49.94	0.0005
120801A	2012-08-01 22:05:22	245.73	-47.37	10.67
120802A	2012-08-02 08:00:51	44.84	13.77	0.0008
120803A	2012-08-03 07:22:16	269.53	-6.73	0.0417

Continued on next page

Table A.2 – continued from previous page

Name	Time (UTC)	RA	Dec	Err
120803B	2012-08-03 11:06:06	314.24	53.30	0.0006
120804A	2012-08-04 00:54:14	233.95	-28.78	0.0005
120805A	2012-08-05 21:28:09	216.54	5.83	0.0008
120805B	2012-08-05 16:56:23	30.13	-21.51	14.5
120806A	2012-08-06 00:10:10	308.99	6.33	11.23
120807A	2012-08-07 07:09:37	241.26	-47.48	0.0005
120811A	2012-08-11 02:35:18	257.18	-22.74	0.0433
120811B	2012-08-11 00:20:31	43.66	-31.68	0.699
120811C	2012-08-11 15:34:52	199.68	62.30	0.0005
120814A	2012-08-14 04:49:14	26.19	22.45	11.04
120814B	2012-08-14 19:16:08	90.57	33.13	14.91
120815A	2012-08-15 02:13:58	273.96	-52.13	0.0004
120816A	2012-08-16 19:18:34	282.14	-6.94	0.0005
120816B	2012-08-16 23:58:18	337.57	-1.68	10.03
120817A	2012-08-17 06:49:42	250.69	-38.35	0.0005
120817B	2012-08-17 04:02:29	8.31	-26.43	0.0833
120817C	2012-08-17 01:22:11	259.97	-9.07	12.62
120819A	2012-08-19 13:10:14	235.91	-7.31	0.0005
120819B	2012-08-19 01:08:28	171.54	49.42	13.08
120820A	2012-08-20 14:02:23	186.64	-12.31	11.46
120821A	2012-08-21 13:23:45	255.27	-40.52	0.0333
120822A	2012-08-22 15:03:57	181.72	80.56	12.94
120824A	2012-08-24 14:16:02	70.92	17.63	10.82
120827A	2012-08-27 05:10:26	222.74	-71.89	10.53
120830A	2012-08-30 07:07:03	88.65	-28.98	0.379

Continued on next page

Table A.2 – continued from previous page

Name	Time (UTC)	RA	Dec	Err
120830B	2012-08-30 05:04:53	337.87	-80.04	10.96
120831A	2012-08-31 21:37:32	144.02	-16.21	13.46
120905A	2012-09-05 15:46:23	355.96	16.99	10.55
120907A	2012-09-07 00:24:24	74.75	-9.31	0.0004
120908A	2012-09-08 22:31:00	230.77	-25.50	1.0
120908B	2012-09-08 20:57:32	268.67	-35.79	10.51
120909A	2012-09-09 01:41:03	275.74	-59.45	0.0004
120911A	2012-09-11 07:08:33	357.98	63.10	0.0005
120911B	2012-09-11 06:25:14	172.15	-37.70	1.055
120913A	2012-09-13 20:18:21	146.40	26.96	0.02
120913B	2012-09-13 23:55:58	213.66	-14.51	0.0167
120914A	2012-09-14 03:26:43	267.94	1.82	11.7
120915A	2012-09-15 11:22:06	283.56	-1.11	12.29
120916A	2012-09-16 04:07:46	205.63	36.70	1.486
120916B	2012-09-16 02:02:17	82.04	-19.22	15.23
120918A	2012-09-18 11:16:10	181.04	-32.76	0.0183
120919A	2012-09-19 07:24:42	214.77	-45.56	0.259
120919B	2012-09-19 01:14:59	302.63	-37.49	0.796
120919C	2012-09-19 19:35:43	303.53	-66.16	15.8
120920A	2012-09-20 00:04:34	27.12	-26.12	13.02
120921A	2012-09-21 21:03:03	96.42	-64.77	10.88
120922A	2012-09-22 22:30:28	234.75	-20.18	0.0006
120923A	2012-09-23 05:16:06	303.80	6.22	0.0006
120926A	2012-09-26 08:02:58	318.39	58.38	10.51
120926B	2012-09-26 10:13:17	59.72	-37.20	11.06

Continued on next page

Table A.2 – continued from previous page

Name	Time (UTC)	RA	Dec	Err
120926C	2012-09-26 18:04:36	24.61	-45.58	23.72
120927A	2012-09-27 22:40:46	136.61	0.42	0.0004
121001A	2012-10-01 18:23:02	276.03	-5.67	0.0005
121004A	2012-10-04 05:03:19	137.46	-11.02	14.05
121005A	2012-10-05 00:42:53	195.17	-2.09	14.07
121005B	2012-10-05 08:09:13	149.73	25.40	11.71
121008A	2012-10-08 10:10:52	340.97	-3.10	13.75
121011A	2012-10-11 11:15:30	260.21	41.11	0.0006
121011B	2012-10-11 22:32:23	182.81	44.11	4.483
121012A	2012-10-12 17:22:16	33.40	14.60	12.43
121014A	2012-10-14 20:11:56	166.65	-29.11	0.0333
121014B	2012-10-14 15:19:01	320.01	-53.43	20.1
121017A	2012-10-17 19:23:28	288.83	-1.60	0.0006
121019A	2012-10-19 05:35:11	43.47	62.14	12.83
121023A	2012-10-23 07:44:18	313.86	-4.38	11.44
121024A	2012-10-24 02:56:12	70.47	-12.29	0.0004
121025A	2012-10-25 07:46:30	248.75	27.73	0.288
121027A	2012-10-27 07:32:29	63.60	-58.83	0.0006
121027B	2012-10-27 00:54:21	4.31	-47.54	10.72
121028A	2012-10-28 05:04:31	271.90	-2.29	0.0005
121028B	2012-10-28 06:43:14	52.56	-25.07	12.93
121029A	2012-10-29 08:24:18	226.80	-28.20	10.54
121031A	2012-10-31 22:50:30	170.77	-3.52	0.0006
121102A	2012-11-02 02:27:00	270.90	-16.96	0.0004
121102B	2012-11-02 01:32:49	258.47	14.09	15.99

Continued on next page

Table A.2 – continued from previous page

Name	Time (UTC)	RA	Dec	Err
121104A	2012-11-04 15:02:17	72.14	14.08	11.16
121108A	2012-11-08 17:47:39	83.19	54.47	0.0005
121109A	2012-11-09 08:06:57	6.84	-42.57	14.69
121112A	2012-11-12 19:20:46	78.98	-55.44	18.72
121113A	2012-11-13 13:02:44	313.17	59.82	10.6
121116A	2012-11-16 11:00:25	180.88	-74.79	12.53
121117A	2012-11-17 08:50:56	31.62	7.43	0.0183
121117B	2012-11-17 00:25:39	279.14	44.93	11.26
121118A	2012-11-18 13:48:54	299.38	65.65	3.433
121118B	2012-11-18 22:27:06	171.70	-3.06	2.209
121118C	2012-11-18 13:48:55	299.38	65.65	10.45
121119A	2012-11-19 13:53:15	311.65	-16.92	13.2
121122A	2012-11-22 21:14:52	35.26	45.14	11.129
121122B	2012-11-22 13:31:28	52.67	46.47	16.56
121122C	2012-11-22 20:52:51	355.45	6.34	10.73
121123A	2012-11-23 10:02:41	307.32	-11.86	0.0004
121123B	2012-11-23 10:35:57	30.52	-18.79	10.52
121124A	2012-11-24 14:32:09	87.93	49.55	17.96
121125A	2012-11-25 08:32:29	228.53	55.31	0.0004
121125B	2012-11-25 11:14:49	177.53	38.54	11.65
121127A	2012-11-27 21:56:00	176.44	-52.41	0.241
121128A	2012-11-28 05:05:37	300.60	54.30	0.0005
121201A	2012-12-01 12:25:42	13.47	-42.94	0.0004
121202A	2012-12-02 04:20:05	256.80	23.95	0.0004
121205A	2012-12-05 12:10:06	238.59	-49.71	15.67

Continued on next page

Table A.2 – continued from previous page

Name	Time (UTC)	RA	Dec	Err
121209A	2012-12-09 21:59:11	326.79	-8.23	0.0004
121210A	2012-12-10 01:56:03	202.54	17.77	13.27
121211A	2012-12-11 13:47:03	195.53	30.15	0.0004
121211B	2012-12-11 16:41:03	72.37	8.63	11.64
121212A	2012-12-12 06:56:12	177.79	78.04	0.0005
121216A	2012-12-16 10:03:18	13.88	-85.44	17.56
121217A	2012-12-17 07:17:47	153.71	-62.35	0.0005
121217B	2012-12-17 07:30:03	153.71	-62.35	10.4
121220A	2012-12-20 07:28:14	31.07	48.28	13.31
121221A	2012-12-21 21:59:31	214.26	33.55	11.22
121223A	2012-12-23 07:11:20	50.11	21.37	10.75
121225A	2012-12-25 09:50:24	264.86	-66.07	0.283
121225B	2012-12-25 10:00:54	308.91	-34.35	3.75
121226A	2012-12-26 19:09:43	168.62	-30.41	0.0333
121229A	2012-12-29 05:00:21	190.10	-50.59	0.0005
121229B	2012-12-29 12:47:35	315.59	-11.94	11.36
121230A	2012-12-30 21:00:07	173.35	-48.72	35.56
121231A	2012-12-31 10:41:24	335.47	-17.78	12.24
130102A	2013-01-02 18:10:53	311.42	49.82	0.0004
130102B	2013-01-02 04:41:42	309.58	-72.38	0.283
130104A	2013-01-04 17:18:08	174.09	25.92	10.68
130106A	2013-01-06 19:53:23	66.67	29.74	11.54
130106B	2013-01-06 23:52:27	28.76	63.38	10.57
130109A	2013-01-09 04:56:28	17.45	19.24	11.05
130112A	2013-01-12 06:52:08	236.03	52.19	11.51

Continued on next page

Table A.2 – continued from previous page

Name	Time (UTC)	RA	Dec	Err
130112B	2013-01-12 08:27:49	196.29	-31.94	11.89
130114A	2013-01-14 00:27:06	310.19	-15.32	15.04
130115A	2013-01-15 17:10:40	171.09	22.62	10.77
130116A	2013-01-16 09:58:16	38.24	15.75	31.61
130117A	2013-01-17 02:05:13	341.24	2.81	12.09
130118A	2013-01-18 11:33:31	278.30	40.98	12.37
130121A	2013-01-21 20:02:01	211.31	-49.49	10.46
130122A	2013-01-22 23:44:09	194.29	59.02	0.0005
130127A	2013-01-27 17:50:23	251.05	-17.07	13.41
130127B	2013-01-27 07:09:55	301.21	-57.21	14.43
130131A	2013-01-31 13:56:22	171.13	48.08	0.0005
130131B	2013-01-31 19:10:08	173.96	15.04	0.0005
130131C	2013-01-31 12:15:15	189.63	-14.48	10.45
130204A	2013-02-04 11:36:53	105.64	41.92	12.58
130206A	2013-02-06 19:36:30	140.39	-58.19	0.0317
130206B	2013-02-06 11:33:35	269.10	49.43	10.67
130208A	2013-02-08 16:24:25	181.60	50.93	11.4
130209A	2013-02-09 23:03:43	33.59	-27.58	10.45
130211A	2013-02-11 03:36:32	147.52	-42.33	0.035
130213A	2013-02-13 21:43:57	99.09	-8.10	14.86
130214A	2013-02-14 03:17:07	325.02	-1.83	16.47
130214B	2013-02-14 19:12:23	56.93	-0.29	10.52
130215A	2013-02-15 01:31:25	43.49	13.39	0.025
130215B	2013-02-15 15:34:18	3.11	59.38	10.61
130216A	2013-02-16 22:15:24	67.90	14.67	0.0167

Continued on next page

Table A.2 – continued from previous page

Name	Time (UTC)	RA	Dec	Err
130216B	2013-02-16 18:58:11	58.87	2.04	0.025
130217A	2013-02-17 16:31:20	96.72	6.80	13.24
130218A	2013-02-18 06:16:27	69.31	-69.13	10.65
130219A	2013-02-19 18:35:51	303.73	40.83	10.47
130219B	2013-02-19 04:44:09	169.29	-22.25	10.63
130219C	2013-02-19 15:01:15	211.60	12.22	19.66
130220A	2013-02-20 23:08:50	306.20	31.74	10.46
130224A	2013-02-24 08:53:04	205.90	59.72	10.72
130228A	2013-02-28 02:40:04	257.28	53.94	13.35
130228C	2013-02-28 05:05:58	240.75	-55.21	10.48
130304A	2013-03-04 09:49:54	98.93	53.57	10.47
130304B	2013-03-04 15:46:51	178.87	-60.29	12.27
130305A	2013-03-05 11:39:11	116.77	52.04	0.03
130305B	2013-03-05 12:37:49	73.32	-1.56	10.55
130306A	2013-03-06 23:47:25	279.48	-11.68	0.0267
130307A	2013-03-07 03:01:44	156.00	23.00	1.093
130307B	2013-03-07 05:42:21	319.52	10.77	11.3
130310A	2013-03-10 20:09:41	141.91	-17.43	0.653
130313A	2013-03-13 16:08:11	236.44	-0.35	0.0433
130314A	2013-03-14 03:31:18	206.21	46.77	10.5
130315A	2013-03-15 12:45:32	157.54	-51.79	0.0217
130318A	2013-03-18 10:56:33	200.74	8.12	14.39
130320A	2013-03-20 07:08:40	192.68	-14.47	4.533
130320B	2013-03-20 13:24:07	195.54	-71.26	1.458
130324A	2013-03-24 01:00:26	255.43	0.05	12.02

Continued on next page

Table A.2 – continued from previous page

Name	Time (UTC)	RA	Dec	Err
130325A	2013-03-25 04:51:54	122.78	-18.90	10.4
130325B	2013-03-25 00:07:48	30.44	62.06	19.2
130327A	2013-03-27 01:47:34	92.04	55.72	0.0005
130327B	2013-03-27 08:24:04	218.00	-69.51	0.17
130331A	2013-03-31 13:35:46	164.47	29.64	10.68
130403A	2013-04-03 20:46:49	199.90	-46.68	13.28
130404A	2013-04-04 10:15:41	30.75	1.54	12.67
130404B	2013-04-04 20:10:05	146.58	-42.16	10.46
130404C	2013-04-04 21:02:12	28.29	56.49	20.99
130406A	2013-04-06 06:55:05	157.78	-62.05	10.61
130406B	2013-04-06 08:00:38	109.66	-27.86	12.92
130406C	2013-04-06 08:29:38	138.21	42.83	18.12
130407A	2013-04-07 23:37:01	248.10	10.51	0.1
130407B	2013-04-07 19:12:44	53.53	44.17	13.95
130408A	2013-04-08 21:51:38	134.41	-32.36	0.0005
130408B	2013-04-08 15:40:24	118.77	66.34	11.12
130409A	2013-04-09 23:02:00	30.52	44.10	10.63
130416A	2013-04-16 16:34:08	99.28	24.70	17.71
130416B	2013-04-16 18:28:55	51.21	-18.25	11.48
130418A	2013-04-18 19:00:53	149.04	13.67	0.0005
130418B	2013-04-18 20:14:47	216.53	-17.54	13.41
130419A	2013-04-19 13:30:29	355.28	9.90	0.0433
130420A	2013-04-20 07:28:29	196.11	59.42	0.0005
130420B	2013-04-20 12:56:32	183.13	54.39	0.0006
130420C	2013-04-20 08:14:04	122.68	-11.43	10.47

Continued on next page

Table A.2 – continued from previous page

Name	Time (UTC)	RA	Dec	Err
130420D	2013-04-20 10:08:10	117.06	-69.03	11.15
130425A	2013-04-25 07:51:16	6.21	-70.18	7.511
130427A	2013-04-27 07:47:57	173.14	27.70	0.001
130427B	2013-04-27 13:20:41	314.90	-22.55	0.0005
130502A	2013-05-02 17:50:30	138.57	-0.12	0.0005
130502B	2013-05-02 07:51:11	66.64	71.08	0.093

REFERENCES

[1] W. Pauli, "Letter to the participants of the conference at Tubingen,", private communication 1930.

[2] C. Cowan, F. Reines, F. Harrison, H. Kruse, and A. McGuire, "Detection of the free neutrino: A Confirmation," *Science* **124**, 103 (1956).

[3] R. Gandhi, C. Quigg, M. Hall Reno, and I. Sarcevic, "Ultrahigh-energy neutrino interactions," *Astroparticle Physics* **5**, 81 (1996) hep-ph/9512364.

[4] S. R. Klein and A. Connolly, "Neutrino Absorption in the Earth, Neutrino Cross-Sections, and New Physics," *ArXiv e-prints* (2013) 1304.4891.

[5] J. A. Formaggio and G. P. Zeller, "From eV to EeV: Neutrino cross sections across energy scales," *Reviews of Modern Physics* **84**, 1307 (2012) 1305.7513.

[6] P. Lipari and T. Stanev, "Propagation of multi-TeV muons," *Phys. Rev. D* **44**, 3543 (1991).

[7] W.-M. Yao *et al.*, "Review of Particle Physics," *Journal of Physics G Nuclear Physics* **33**, 1 (2006) astro-ph/0601168.

[8] D. Chirkin and W. Rhode, "Propagating leptons through matter with Muon Monte Carlo (MMC)," *ArXiv High Energy Physics - Phenomenology e-prints* (2004) hep-ph/0407075.

[9] D. E. Groom, N. V. Mokhov, and S. I. Striganov, "Muon stopping power and range tables 10-MeV to 100-TeV," *Atom.Data Nucl.Data Tabl.* **78**, 183 (2001).

[10] Gregors, "Schematic of a particle shower,", `http://commons.wikimedia.org/wiki/File:Schematic_of_a_particle_shower.jpg` 2011, Licensed under CC BY-SA 3.0 via Wikimedia Commons.

[11] J. van Santen, "Neutrino Interactions in IceCube above 1 TeV,", `https://docushare.icecube.wisc.edu/dsweb/Get/Document-72536/thesis.pdf` 2014, PhD thesis, University of Wisconsin-Madison.

[12] A. Horvath, "Cherenkov,", `http://commons.wikimedia.org/wiki/File:Cherenkov.svg#/media/File:Cherenkov.svg` 2006, Licensed under CC BY-SA 2.5 via Wikimedia Commons and Modifications Added By James Casey.

[13] L. Rädel and C. Wiebusch, "Calculation of the Cherenkov light yield from electromagnetic cascades in ice with Geant4," *Astroparticle Physics* **44**, 102 (2013) 1210.5140.

[14] F. Capozzi, L. Fogli, G. E. Lisi, A. Marrone, D. Montanino, and A. Palazzo, "Status of three-neutrino oscillation parameters, circa 2013," *Phys. Rev. D* **89**, 093018 (2014).

[15] Particle Data Group K. Olive *et al.*, "Review of Particle Physics," *Chin.Phys.* **C38**, 090001 (2014).

[16] R. Davis, D. Harmer, and K. Hoffman, "Search for Neutrinos from the Sun," *Phys. Rev. Lett.* **20**, 1205 (1968).

[17] B. T. Cleveland, T. Daily, R. Davis, Jr., J. R. Distel, K. Lande, C. K. Lee, P. S. Wildenhain, and J. Ullman, "Measurement of the Solar Electron Neutrino Flux with the Homestake Chlorine Detector," ApJ **496**, 505 (1998).

[18] Q. R. Ahmad *et al.*, "Measurement of the Rate of ν_e + d –> p + p + e^- Interactions Produced by ^{8}B Solar Neutrinos at the Sudbury Neutrino Observatory," *Physical Review Letters* **87**, 071301 (2001) nucl-ex/0106015.

[19] H. Nunokawa, S. Parke, and J. W. F. Valle, "CP violation and neutrino oscillations," *Progress in Particle and Nuclear Physics* **60**, 338 (2008) 0710.0554.

[20] R. N. Cahn, D. A. Dwyer, S. J. Freedman, W. C. Haxton, R. W. Kadel, Y. G. Kolomensky, K. B. Luk, P. McDonald, G. D. Orebi Gann, and A. W. P. Poon, "White Paper: Measuring the Neutrino Mass Hierarchy," *ArXiv e-prints* (2013) 1307.5487.

[21] R. M. Bionta, G. Blewitt, C. B. Bratton, D. Casper, A. Ciocio, R. Claus, B. Cortez, M. Crouch, S. T. Dye, S. Errede, G. W. Foster, W. Gajewski, K. S. Ganezer, M. Goldhaber, T. J. Haines, T. W. Jones, D. Kielczewska, W. R. Kropp, J. G. Learned, J. M. LoSecco, J. Matthews, R. Miller, M. S. Mudan, H. S. Park, L. R. Price, F. Reines, J. Schultz, S. Seidel, E. Shumard, D. Sinclair, H. W. Sobel, J. L. Stone, L. R. Sulak, R. Svoboda, G. Thornton, J. C. van der Velde, and C. Wuest, "Observation of a neutrino burst in coincidence with supernova 1987A in the Large Magellanic Cloud," *Phys. Rev. Lett.* **58**, 1494 (1987).

[22] C. B. Bratton, D. Casper, A. Ciocio, R. Claus, M. Crouch, S. T. Dye, S. Errede, W. Gajewski, M. Goldhaber, T. J. Haines, T. W. Jones, D. Kielczewska, W. R. Kropp, J. G. Learned, J. M. LoSecco, J. Matthews, R. Miller, M. Mudan, L. R. Price, F. Reines, J. Schultz, S. Seidel, D. Sinclair, H. W. Sobel, J. L. Stone, L. Sulak, R. Svoboda, G. Thornton, and J. C. van der Velde, "Angular distribution of events from SN1987A," *Phys. Rev. D* **37**, 3361 (1988).

[23] K. Hirata, T. Kajita, M. Koshiba, M. Nakahata, Y. Oyama, N. Sato, A. Suzuki, M. Takita, Y. Totsuka, T. Kifune, T. Suda, K. Takahashi, T. Tanimori, K. Miyano, M. Yamada, E. W. Beier, L. R. Feldscher, S. B. Kim, A. K. Mann, F. M. Newcomer, R. Van, W. Zhang, and B. G. Cortez, "Observation of a neutrino burst from the supernova SN1987A," *Phys. Rev. Lett.* **58**, 1490 (1987).

[24] K. S. Hirata, T. Kajita, M. Koshiba, M. Nakahata, Y. Oyama, N. Sato, A. Suzuki, M. Takita, Y. Totsuka, T. Kifune, T. Suda, K. Takahashi, T. Tanimori, K. Miyano, M. Yamada, E. W. Beier, L. R. Feldscher, W. Frati, S. B. Kim, A. K. Mann, F. M. Newcomer, R. Van Berg, W. Zhang, and B. G. Cortez, "Observation in the Kamiokande-II detector of the neutrino burst from supernova SN1987A," *Phys. Rev. D* **38**, 448 (1988).

[25] E. N. Alexeyev, L. N. Alexeyeva, I. V. Krivosheina, and V. I. Volchenko, "Detection of the neutrino signal from SN 1987A in the LMC using the INR Baksan underground scintillation telescope," *Physics Letters B* **205**, 209 (1988).

[26] IceCube Collaboration, "Evidence for High-Energy Extraterrestrial Neutrinos at the IceCube Detector," *Science* **342** (2013) 1311.5238.

[27] M. G. Aartsen, M. Ackermann, J. Adams, J. A. Aguilar, M. Ahlers, M. Ahrens, D. Altmann, T. Anderson, C. Arguelles, T. C. Arlen, and et al., "Observation of High-Energy Astrophysical Neutrinos in Three Years of IceCube Data," *Physical Review Letters* **113**, 101101 (2014) 1405.5303.

[28] V. F. Hess, "ber Beobachtungen der durchdringenden Strahlung bei sieben Freiballonfahrten," *Physikalische Zeitschrift* **13**, 1084 (1912).

[29] L. Anchordoqui, T. Paul, S. Reucroft, and J. Swain, "Ultrahigh Energy Cosmic Rays," *International Journal of Modern Physics A* **18**, 2229 (2003) hep-ph/0206072, (The figure is from Murat Boratav).

[30] T. Piran, "Gamma-ray bursts and the fireball model," Phys. Rep. **314**, 575 (1999) astro-ph/9810256.

[31] M. Ackermann *et al.*, "Multiwavelength Observations of GRB 110731A: GeV Emission from Onset to Afterglow," ApJ **763**, 71 (2013) 1212.0973.

[32] C. Kouveliotou, R. A. M. J. Wijers, and S. Woosley, editors, *Gamma-ray Bursts* (Cambridge University Press, 2012).

[33] P. Mészáros, "Gamma-ray bursts," *Reports on Progress in Physics* **69**, 2259 (2006) astro-ph/0605208.

[34] M. S. Briggs, "Gamma Ray Astrophysics at the NSSTC,", `http://gammaray.msfc.nasa.gov/batse/grb/skymap/`, Accessed: 2015-03-13.

[35] W. S. Paciesas, C. A. Meegan, G. N. Pendleton, M. S. Briggs, C. Kouveliotou, T. M. Koshut, J. P. Lestrade, M. L. McCollough, J. J. Brainerd, J. Hakkila, W. Henze, R. D. Preece, V. Connaughton, R. M. Kippen, R. S. Mallozzi, G. J. Fishman, G. A. Richardson, and M. Sahi, "The Fourth BATSE Gamma-Ray Burst Catalog (Revised)," ApJS **122**, 465 (1999) astro-ph/9903205.

[36] D. Q. Lamb, C. Graziani, and I. A. Smith, "Evidence for two distinct morphological classes of gamma-ray bursts from their short time scale variability," ApJ **413**, L11 (1993) astro-ph/9306011.

[37] J. P. Dezalay, J. P. Lestrade, C. Barat, R. Talon, R. Sunyaev, O. Terekhov, and A. Kuznetsov, "The Hardness-Duration Diagram of Gamma-Ray Bursts," ApJ **471**, L27 (1996).

[38] "Overview of GRB Spectral Analysis,", `http://fermi.gsfc.nasa.gov/ssc/data/analysis/documentation/Cicerone/Cicerone_GRBs/Overview_GRB_Spec_Anal.html`, Accessed: 2015-03-13.

[39] T. Piran, "The physics of gamma-ray bursts," *Reviews of Modern Physics* **76**, 1143 (2004) astro-ph/0405503.

[40] D. N. Burrows, P. Romano, A. Falcone, S. Kobayashi, B. Zhang, A. Moretti, P. T. O'Brien, M. R. Goad, S. Campana, K. L. Page, L. Angelini, S. Barthelmy, A. P. Beardmore, M. Capalbi, G. Chincarini, J. Cummings, G. Cusumano, D. Fox, P. Giommi, J. E. Hill, J. A. Kennea, H. Krimm, V. Mangano, F. Marshall, P. Mészáros, D. C. Morris, J. A. Nousek, J. P. Osborne, C. Pagani, M. Perri, G. Tagliaferri, A. A. Wells, S. Woosley, and N. Gehrels, "Bright X-ray Flares in Gamma-Ray Burst Afterglows," *Science* **309**, 1833 (2005) astro-ph/0506130.

[41] M. J. Rees and P. Meszaros, "Relativistic fireballs - Energy conversion and time-scales," MNRAS **258**, 41P (1992).

[42] G. A. MacLachlan, A. Shenoy, E. Sonbas, K. S. Dhuga, B. E. Cobb, T. N. Ukwatta, D. C. Morris, A. Eskandarian, L. C. Maximon, and W. C. Parke, "Minimum variability time-scales of long and short GRBs," MNRAS **432**, 857 (2013) 1201.4431.

[43] T. K. Gaisser, F. Halzen, and T. Stanev, "Particle astrophysics with high energy neutrinos," Phys. Rep. **258**, 173 (1995) hep-ph/9410384.

[44] "UKSSDC — Pre-Swift GRBs,", `http://www.swift.ac.uk/about/grb.php`, Accessed: 2015-03-13.

[45] P. Blasi, "Lecture 2: Particle Acceleration,", `http://fermi.gsfc.nasa.gov/science/mtgs/summerschool/2012/week1/CR2_Blasi.pdf` 2012, Presented at the 2012 Fermi Summer School.

[46] T. J. Galama, R. A. M. J. Wijers, M. Bremer, P. J. Groot, R. G. Strom, A. G. de Bruyn, C. Kouveliotou, C. R. Robinson, and J. van Paradijs, "The 1.4 GHz Light Curve of GRB 970508," ApJ **500**, L101 (1998) astro-ph/9804190.

[47] D. A. Frail, S. R. Kulkarni, L. Nicastro, M. Feroci, and G. B. Taylor, "The radio afterglow from the γ-ray burst of 8 May 1997," Nature **389**, 261 (1997).

[48] S. Razzaque, P. Mészáros, and E. Waxman, "High Energy Neutrinos from Gamma-Ray Bursts with Precursor Supernovae," *Physical Review Letters* **90**, 241103 (2003) astro-ph/0212536.

[49] J. Granot and D. Guetta, "Neutrinos from Pulsar Wind Bubbles as Precursors to Gamma-Ray Bursts: ~ 10 TeV," *Phys. Rev. Lett.* **90**, 191102 (2003) astro-ph/0211433.

[50] P. Mészáros and M. J. Rees, "Optical and Long-Wavelength Afterglow from Gamma-Ray Bursts," ApJ **476**, 232 (1997) astro-ph/9606043.

[51] K. Murase and S. Nagataki, "High energy neutrino emission and neutrino background from gamma-ray bursts in the internal shock model," *Phys. Rev. D* **73**, 063002 (2006).

[52] E. Waxman and J. N. Bahcall, "Neutrino Afterglow from Gamma-Ray Bursts: ˜10^{18} EV," ApJ **541**, 707 (2000) hep-ph/9909286.

[53] S. Kobayashi, B. Zhang, P. Mészáros, and D. Burrows, "Inverse Compton X-Ray Flare from Gamma-Ray Burst Reverse Shock," ApJ **655**, 391 (2007) astro-ph/0506157.

[54] P. T. O'Brien, R. Willingale, J. Osborne, M. R. Goad, K. L. Page, S. Vaughan, E. Rol, A. Beardmore, O. Godet, C. P. Hurkett, A. Wells, B. Zhang, S. Kobayashi, D. N. Burrows, J. A. Nousek, J. A. Kennea, A. Falcone, D. Grupe, N. Gehrels, S. Barthelmy, J. Cannizzo, J. Cummings, J. E. Hill, H. Krimm, G. Chincarini, G. Tagliaferri, S. Campana, A. Moretti, P. Giommi, M. Perri, V. Mangano, and V. LaParola, "The Early X-Ray Emission from GRBs," ApJ **647**, 1213 (2006) astro-ph/0601125.

[55] K. Murase and S. Nagataki, "High Energy Neutrino Flashes from Far-Ultraviolet and X-Ray Flares in Gamma-Ray Bursts," *Physical Review Letters* **97**, 051101 (2006) astro-ph/0604437.

[56] "GCN: The Gamma-ray Coordinates Network (TAN: Transient Astronomy Network),", `http://gcn.gsfc.nasa.gov/`, Accessed: 2015-03-13.

[57] Fermi-GBM Collaborations S. Zhu *et al.*, "Fermi-LAT Observations of the Gamma-ray Burst GRB 130427A," (2013) 1311.5623.

[58] S. D. Barthelmy, L. M. Barbier, J. R. Cummings, E. E. Fenimore, N. Gehrels, D. Hullinger, H. A. Krimm, C. B. Markwardt, D. M. Palmer, A. Parsons, G. Sato, M. Suzuki, T. Takahashi, M. Tashiro, and J. Tueller, "The Burst Alert Telescope (BAT) on the SWIFT Midex Mission," Space Sci. Rev. **120**, 143 (2005) astro-ph/0507410.

[59] "Swift's Burst Alert Telescope (BAT),", `http://swift.gsfc.nasa.gov/about_swift/bat_desc.html`, Accessed: 2015-03-13.

[60] "Swift's X-Ray Telescope (XRT),", `http://swift.gsfc.nasa.gov/about_swift/xrt_desc.html`, Accessed: 2015-03-13.

[61] "Swift's Ultraviolet/Optical Telescope (UVOT),", `http://swift.gsfc.nasa.gov/about_swift/uvot_desc.html`, Accessed: 2015-03-13.

[62] "Swift-XRT light curves of GRB 130427A,", `http://www.swift.ac.uk/xrt_curves/554620`, Accessed: 2015-03-13.

[63] C. Winkler, T. J.-L. Courvoisier, G. Di Cocco, N. Gehrels, A. Giménez, S. Grebenev, W. Hermsen, J. M. Mas-Hesse, F. Lebrun, N. Lund, G. G. C. Palumbo, J. Paul, J.-P. Roques, H. Schnopper, V. Schönfelder, R. Sunyaev, B. Teegarden, P. Ubertini, G. Vedrenne, and A. J. Dean, "The INTEGRAL mission," A&A **411**, L1 (2003).

[64] G. Vedrenne, J.-P. Roques, V. Schönfelder, P. Mandrou, G. G. Lichti, A. von Kienlin, B. Cordier, S. Schanne, J. Knödlseder, G. Skinner, P. Jean, F. Sanchez, P. Caraveo, B. Teegarden, P. von Ballmoos, L. Bouchet, P. Paul, J. Matteson, S. Boggs, C. Wunderer, P. Leleux, G. Weidenspointner, P. Durouchoux, R. Diehl, A. Strong, M. Cassé, M. A. Clair, and Y. André, "SPI: The spectrometer aboard INTEGRAL," A&A **411**, L63 (2003).

[65] A. von Kienlin, N. Arend, G. G. Lichti, A. W. Strong, and P. Connell, "Gamma-ray burst detection with INTEGRAL/SPI," in *X-Ray and Gamma-Ray Telescopes and Instruments for Astronomy.*, edited by J. E. Truemper and H. D. Tananbaum volume 4851 of *Society of Photo-Optical Instrumentation Engineers (SPIE) Conference Series* pp. 1336–1346 2003 astro-ph/0302139.

[66] "The Global Geospace satellite Wind,", https://heasarc.gsfc.nasa.gov/docs/heasarc/missions/wind.html, Accessed: 2015-03-13.

[67] T. Mihara, M. Nakajima, M. Sugizaki, M. Serino, M. Matsuoka, M. Kohama, K. Kawasaki, H. Tomida, S. Ueno, N. Kawai, J. Kataoka, M. Morii, A. Yoshida, K. Yamaoka, S. Nakahira, H. Negoro, N. Isobe, M. Yamauchi, and I. Sakurai, "Gas Slit Camera (GSC) onboard MAXI on ISS," PASJ **63**, 623 (2011) 1103.4224.

[68] M. Serino, T. Sakamoto, N. Kawai, A. Yoshida, M. Ohno, Y. Ogawa, Y. Nishimura, K. Fukushima, M. Higa, K. Ishikawa, M. Ishikawa, T. Kawamuro, M. Kimura, M. Matsuoka, T. Mihara, M. Morii, Y. E. Nakagawa, S. Nakahira, M. Nakajima, Y. Nakano, H. Negoro, T. Onodera, M. Sasaki, M. Shidatsu, J. Sugimoto, M. Sugizaki, F. Suwa, K. Suzuki, Y. Tachibana, T. Takagi, T. Toizumi, H. Tomida, Y. Tsuboi, H. Tsunemi, Y. Ueda, S. Ueno, R. Usui, H. Yamada, T. Yamamoto, K. Yamaoka, M. Yamauchi, K. Yoshidome, and T. Yoshii, "MAXI observations of GRBs," *ArXiv e-prints* (2014) 1406.3912.

[69] S. Mereghetti, G. Barbiellini, G. Budini, P. Caraveo, E. Costa, V. Cocco, G. Di Cocco, M. Feroci, C. Labanti, F. Longo, E. Morelli, A. Morselli, A. Pellizzoni, F. Perotti, P. Picozza, M. Prest, P. Soffitta, L. Soli, M. Tavani, E. Vallazza, and S. Vercellone, "The AGILE gamma-ray astronomy mission," in *American Institute of Physics Conference Series*, edited by B. L. Dingus, M. H. Salamon, and D. B. Kieda volume 515 of *American Institute of Physics Conference Series* pp. 467–473 2000 astro-ph/9911256.

[70] C. Pittori, "The Gamma-Ray Imaging Detector AGILE: Scientific Goals and Instrument Performance," *Chinese Journal of Astronomy and Astrophysics Supplement* **3**, 517 (2003).

[71] "AGILE,", http://www.asi.it/en/activity/high_energy/agile, Accessed: 2015-03-13.

[72] K. Mitsuda *et al.*, "The X-Ray Observatory Suzaku," PASJ **59**, 1 (2007).

[73] D. Lennarz, unpublished, 2014.

[74] M. Ackermann *et al.*, "Detection of a Spectral Break in the Extra Hard Component of GRB 090926A," ApJ **729**, 114 (2011) 1101.2082.

[75] R. Abbasi, Y. Abdou, T. Abu-Zayyad, M. Ackermann, J. Adams, J. A. Aguilar, M. Ahlers, D. Altmann, K. Andeen, J. Auffenberg, and et al., "An absence of neutrinos associated with cosmic-ray acceleration in γ-ray bursts," Nature **484**, 351 (2012) 1204.4219.

[76] R. Abbasi, Y. Abdou, T. Abu-Zayyad, J. Adams, J. A. Aguilar, M. Ahlers, K. Andeen, J. Auffenberg, X. Bai, M. Baker, and et al., "Limits on Neutrino Emission from Gamma-Ray Bursts with the 40 String IceCube Detector," *Physical Review Letters* **106**, 141101 (2011) 1101.1448.

[77] R. Abbasi, Y. Abdou, T. Abu-Zayyad, J. Adams, J. A. Aguilar, M. Ahlers, K. Andeen, J. Auffenberg, X. Bai, M. Baker, and et al., "Search for Muon Neutrinos from Gamma-ray Bursts with the IceCube Neutrino Telescope," ApJ **710**, 346 (2010) 0907.2227.

[78] D. Guetta, D. Hooper, J. Alvarez-Mun˜Iz, F. Halzen, and E. Reuveni, "Neutrinos from individual gamma-ray bursts in the BATSE catalog," *Astroparticle Physics* **20**, 429 (2004) astro-ph/0302524.

[79] M. Ahlers, M. C. Gonzalez-Garcia, and F. Halzen, "GRBs on probation: Testing the UHE CR paradigm with IceCube," *Astroparticle Physics* **35**, 87 (2011) 1103.3421.

[80] IceCube Collaboration, M. G. Aartsen, M. Ackermann, J. Adams, J. A. Aguilar, M. Ahlers, M. Ahrens, D. Altmann, T. Anderson, C. Arguelles, and et al., "Search for Prompt Neutrino Emission from Gamma-Ray Bursts with IceCube," *ArXiv e-prints* (2014) 1412.6510.

[81] S. Hümmer, P. Baerwald, and W. Winter, "Neutrino Emission from Gamma-Ray Burst Fireballs, Revised," *Physical Review Letters* **108**, 231101 (2012) 1112.1076.

[82] M. J. Rees and P. Mészáros, "Dissipative Photosphere Models of Gamma-Ray Bursts and X-Ray Flashes," ApJ **628**, 847 (2005) astro-ph/0412702.

[83] B. Zhang and P. Kumar, "Model-Dependent High-Energy Neutrino Flux from Gamma-Ray Bursts," *Physical Review Letters* **110**, 121101 (2013) 1210.0647.

[84] J. G. Learned and K. Mannheim, "HIGH-ENERGY NEUTRINO ASTROPHYSICS," *Annual Review of Nuclear and Particle Science* **50**, 679 (2000) http://dx.doi.org/10.1146/annurev.nucl.50.1.679.

[85] R. Abbasi, Y. Abdou, T. Abu-Zayyad, M. Ackermann, J. Adams, J. A. Aguilar, M. Ahlers, D. Altmann, K. Andeen, J. Auffenberg, and et al., "Search for ultrahigh-energy tau neutrinos with IceCube," Phys. Rev. D **86**, 022005 (2012) 1202.4564.

[86] M. Ackermann *et al.*, "Optical properties of deep glacial ice at the South Pole," *Journal of Geophysical Research: Atmospheres* **111**, n/a (2006).

[87] The IceCube Collaboration, "The IceCube Data Acquisition System: Signal Capture, Digitization, and Timestamping," *ArXiv e-prints* (2008) 0810.4930.

[88] J. Ahrens *et al.*, "Muon track reconstruction and data selection techniques in AMANDA," *Nuclear Instruments and Methods in Physics Research A* **524**, 169 (2004) astro-ph/0407044.

[89] N. Whitehorn, "A Search for High-Energy Neutrino Emission from Gamma-Ray Bursts,", `https://docushare.icecube.wisc.edu/dsweb/Get/Document-60879/thesis.pdf` 2012, PhD thesis, University of Wisconsin-Madison.

[90] K. M. Górski, E. Hivon, A. J. Banday, B. D. Wandelt, F. K. Hansen, M. Reinecke, and M. Bartelmann, "HEALPix: A Framework for High-Resolution Discretization and Fast Analysis of Data Distributed on the Sphere," ApJ **622**, 759 (2005) astro-ph/0409513.

[91] IceCube Collaboration, M. G. Aartsen, M. Ackermann, J. Adams, J. A. Aguilar, M. Ahlers, M. Ahrens, D. Altmann, T. Anderson, C. Arguelles, and et al., "Flavor Ratio of Astrophysical Neutrinos above 35 TeV in IceCube," *ArXiv e-prints* (2015) 1502.03376.

[92] J. Braun, J. Dumm, F. De Palma, C. Finley, A. Karle, and T. Montaruli, "Methods for point source analysis in high energy neutrino telescopes," *Astroparticle Physics* **29**, 299 (2008) 0801.1604.

[93] S. D. Barthelmy, L. M. Barbier, J. R. Cummings, E. E. Fenimore, N. Gehrels, D. Hullinger, H. A. Krimm, C. B. Markwardt, D. M. Palmer, A. Parsons, G. Sato, M. Suzuki, T. Takahashi, M. Tashiro, and J. Tueller, "The Burst Alert Telescope (BAT) on the SWIFT Midex Mission," Space Sci. Rev. **120**, 143 (2005) astro-ph/0507410.

[94] W. S. Paciesas, C. A. Meegan, A. von Kienlin, P. N. Bhat, E. Bissaldi, M. S. Briggs, J. M. Burgess, V. Chaplin, V. Connaughton, R. Diehl, G. J. Fishman, G. Fitzpatrick, S. Foley, M. Gibby, M. Giles, A. Goldstein, J. Greiner, D. Gruber, S. Guiriec, A. J. van der Horst, R. M. Kippen, C. Kouveliotou, G. Lichti, L. Lin, S. McBreen, R. D. Preece, A. Rau, D. Tierney, and C. Wilson-Hodge, "The Fermi GBM Gamma-Ray Burst Catalog: The First Two Years," ApJS **199**, 18 (2012) 1201.3099.

[95] N. Baddour, "Operational and convolution properties of three-dimensional Fourier transforms in spherical polar coordinates," 2010.

[96] A. von Kienlin, C. A. Meegan, W. S. Paciesas, P. N. Bhat, E. Bissaldi, M. S. Briggs, J. M. Burgess, D. Byrne, V. Chaplin, W. Cleveland, V. Connaughton, A. C. Collazzi, G. Fitzpatrick, S. Foley, M. Gibby, M. Giles, A. Goldstein, J. Greiner, D. Gruber, S. Guiriec, A. J. van der Horst, C. Kouveliotou, E. Layden, S. McBreen, S. McGlynn, V. Pelassa, R. D. Preece, A. Rau, D. Tierney, C. A. Wilson-Hodge, S. Xiong, G. Younes, and H.-F. Yu, "The Second Fermi GBM Gamma-Ray Burst Catalog: The First Four Years," ApJS **211**, 13 (2014) 1401.5080.

[97] G. J. Feldman and R. D. Cousins, "Unified approach to the classical statistical analysis of small signals," Phys. Rev. D **57**, 3873 (1998) physics/9711021.

[98] A. D. Falcone, D. Morris, J. Racusin, G. Chincarini, A. Moretti, P. Romano, D. N. Burrows, C. Pagani, M. Stroh, D. Grupe, S. Campana, S. Covino, G. Tagliaferri, R. Willingale, and N. Gehrels, "The First Survey of X-Ray Flares from Gamma-Ray Bursts Observed by Swift: Spectral Properties and Energetics," ApJ **671**, 1921 (2007) 0706.1564.